Atmos. Chem. Phys., 24, 1–21, 2024
https://doi.org/10.5194/acp-24-1-2024

Atmospheric Chemistry and Physics
Open Access
EGU

Seasonal variations in photooxidant formation and light absorption in aqueous extracts of ambient particles

Lan Ma[1,a], Reed Worland[1,b], Laura Heinlein[1], Chrystal Guzman[1,c], Wenqing Jiang[2], Christopher Niedek[2], Keith J. Bein[3], Qi Zhang[2], and Cort Anastasio[1]

[1]Department of Land, Air and Water Resources, University of California, Davis, One Shields Avenue, Davis, CA 95616-8627, USA
[2]Department of Environmental Toxicology, University of California, Davis, One Shields Avenue, Davis, CA 95616-8627, USA
[3]Center for Health and the Environment, University of California, Davis, One Shields Avenue, Davis, CA 95616-8627, USA
[a]now at: SGS-CSTC Standards Technical Services Co. Ltd., Hangzhou Branch, Hangzhou, Zhejiang Province, 310052, China
[b]now at: Department of Chemistry, University of Washington, 1410 Northeast Campus Parkway, Seattle, WA 98195, USA
[c]now at: Department of Pharmacology, University of Washington, 1410 Northeast Campus Parkway, Seattle, WA 98195, USA

Correspondence: Cort Anastasio (canastasio@ucdavis.edu)

Received: 29 April 2023 – Discussion started: 11 May 2023
Revised: 11 October 2023 – Accepted: 20 October 2023 – Published: 2 January 2024

Abstract. Fog/cloud drops and aerosol liquid water are important sites for the transformations of atmospheric species, largely through reactions with photoformed oxidants such as the hydroxyl radical ($^{\bullet}$OH), singlet molecular oxygen ($^1O_2^*$), and oxidizing triplet excited states of organic matter ($^3C^*$). Despite their importance, few studies have measured these oxidants or their seasonal variations. To address this gap, we collected ambient $PM_{2.5}$ from Davis, California, over the course of a year and measured photooxidant concentrations and light absorption in dilute aqueous extracts. Mass absorption coefficients (MACs) normalized by dissolved organic carbon range from 0.4–3.8 m^2 per gram C at 300 nm. Concentrations of $^{\bullet}$OH, $^1O_2^*$, and $^3C^*$ in the extracts range from (0.2–4.7) $\times 10^{-15}$ M, (0.7–45) $\times 10^{-13}$ M, and (0.03–7.9) $\times 10^{-13}$ M, respectively, with biomass burning brown carbon playing a major role in light absorption and the formation of $^1O_2^*$ and $^3C^*$. Extrapolating photooxidant kinetics from our dilute particle extracts to concentrated aerosol liquid water (ALW) conditions gives an estimated $^{\bullet}$OH concentration of 7×10^{-15} M and ranges for $^1O_2^*$ and $^3C^*$ of (0.6–7) $\times 10^{-12}$ M and (0.2–1) $\times 10^{-12}$ M, respectively. Compared to the results in Kaur et al. (2019), our ALW predictions show roughly 10 times higher $^{\bullet}$OH, up to 5 times higher ^3C, and $^1O_2^*$ concentrations that are lower by factors of 20–100. These concentrations suggest that $^3C^*$ and $^1O_2^*$ in ALW dominate the processing of organic compounds that react quickly with these oxidants (e.g., phenols and furans, respectively), while $^{\bullet}$OH is more important for less reactive organics.

Published by Copernicus Publications on behalf of the European Geosciences Union.

1 Introduction

Atmospheric waters, including fog/cloud drops and liquid water on aerosol particles, are important media for photochemical transformations of chemical species (Herrmann et al., 2010, 2015). These include formation of aqueous secondary organic aerosol (aqSOA), formation and photobleaching of brown carbon (BrC), oxidation of reduced sulfur, and aerosol aging (Ervens, 2018, 2011; Gilardoni et al., 2016; Laskin et al., 2015; McNeill, 2015; Seinfeld and Pandis, 2016; Wang et al., 2016; Zhao et al., 2015). Many of these processes are driven by photochemically generated oxidants, including the hydroxyl radical ($^{\bullet}$OH), triplet excited states of organic matter (^{3}C*), and singlet molecular oxygen ($^1O_2^*$) (Ervens et al., 2014; Herrmann, 2003; McNeill and Canonica, 2016; Ossola et al., 2021).

The hydroxyl radical ($^{\bullet}$OH), the best studied aqueous oxidant in the atmosphere, is highly reactive with most reduced species but has a relatively low abundance compared to ^{3}C* and $^1O_2^*$. Concentrations of $^{\bullet}$OH in fog and cloud waters, as well as aqueous extracts of ambient particles and lab-generated secondary organic aerosol, are typically 10^{-17} to 10^{-15} M (Anastasio and McGregor, 2001; Arakaki et al., 2013; Dorfman and Adams, 1973; Kaur and Anastasio, 2017; Kaur et al., 2019; Manfrin et al., 2019; Tilgner and Herrmann, 2018). Sources of $^{\bullet}$OH in the aqueous phase include mass transfer from the gas phase; Fenton or Fenton-like reactions of reduced metals with hydrogen peroxide; and photolysis of nitrate, nitrite, iron complexes, hydrogen peroxide, and organic hydroperoxides (Badali et al., 2015; Herrmann et al., 2010; Tilgner and Herrmann, 2018; Tong et al., 2016). Additionally, organic compounds in atmospheric waters can affect $^{\bullet}$OH production. For example, the interaction of humic-like substances (HULIS) or secondary organic aerosol (SOA) with Fe(II) can enhance or suppress $^{\bullet}$OH formation (Baba et al., 2015; Gonzalez et al., 2017; Hems and Abbatt, 2018; Tong et al., 2016; Zuo and Hoigné, 1992). This suggests that seasonal variations in particle composition (e.g., SOA and Fe) can affect $^{\bullet}$OH kinetics, as reported recently for $^{\bullet}$OH photoproduction in extracts of particulate matter (PM) from Colorado: winter $^{\bullet}$OH originated from nitrate photolysis, while summer $^{\bullet}$OH was more linked to soluble iron (Leresche et al., 2021). But little is known about how $^{\bullet}$OH concentrations in particles vary with season or among particle types. Although the seasonality of gas-phase $^{\bullet}$OH has been characterized (Martin et al., 2003; Pfannerstill et al., 2021; Rohrer and Berresheim, 2006), mass transport of $^{\bullet}$OH(g) is a minor source of $^{\bullet}$OH to particle water (Kaur et al., 2019; Leresche et al., 2021; Ma et al., 2023a) and thus is not sufficient to predict the seasonality of particle $^{\bullet}$OH.

Triplet excited states (^{3}CDOM*) are formed when organic chromophores (i.e., brown carbon, BrC) absorb sunlight and are promoted to a higher energy state (McNeill and Canonica, 2016). Oxidizing triplets (^{3}C*), i.e., the subset of triplets that have high reduction potential, are effective oxidants, reacting with phenols and biogenic volatile compounds to form SOA and BrC and oxidizing bisulfite to sulfate (González Palacios et al., 2016; Monge et al., 2012; Rossignol et al., 2014; Smith et al., 2014; X. Wang et al., 2020; Yu et al., 2014). For compounds (like phenols) that react rapidly with triplets, ^{3}C* can be as important an oxidant as $^{\bullet}$OH in cloud and fog drops, where oxidizing triplet concentrations are 10^{-15}–10^{-13} M (Kaur and Anastasio, 2018; Kaur et al., 2019; Ma et al., 2021; Smith et al., 2015). Moreover, triplet concentrations are estimated to be enhanced by 1 or 2 orders of magnitude in aerosol liquid water (Kaur et al., 2019; Ma et al., 2023a). The ability of dissolved organic matter (DOM) to form triplets depends on its composition. In surface waters, quantum yields of ^{3}CDOM* are positively correlated with the E2/E3 parameter and more highly saturated molecular formulas, i.e., with lower average molecular weights and lower aromaticity (Berg et al., 2019; Maizel and Remucal, 2017; McCabe and Arnold, 2017, 2018; Mckay et al., 2017). However, little is known about how ^{3}C* formation in atmospheric waters depends on BrC characteristics or season.

The final oxidant we consider, singlet molecular oxygen ($^1O_2^*$), is formed when triplet excited states transfer energy to dissolved molecular oxygen. $^1O_2^*$ reacts rapidly with certain electron-rich compound classes such as furans, polycyclic aromatic hydrocarbons, some amino acids, and substituted alkenes (Gollnick and Griesbeck, 1985; McGregor and Anastasio, 2001; Richards-Henderson et al., 2015; Wilkinson et al., 1995; Zeinali et al., 2019). $^1O_2^*$ concentrations in fog and cloud waters and aqueous particle extracts are the highest of the three oxidants, in the range of 10^{-14}–10^{-12} M (Bogler et al., 2022; Kaur and Anastasio, 2017; Kaur et al., 2019; Leresche et al., 2021; Manfrin et al., 2019). Dissolved black carbon can also produce $^1O_2^*$, resulting in concentrations on the order of 10^{-12} M (Li et al., 2019). Though $^1O_2^*$ is not as reactive as ^{3}C* and $^{\bullet}$OH, its concentration increases by orders of magnitude when moving from dilute cloud/fog conditions towards the more concentrated conditions of aerosol liquid water (Kaur et al., 2019; Ma et al., 2023a). Since $^1O_2^*$ is born from ^{3}CDOM*, these two oxidants are tightly linked. For example, in surface waters the quantum yield of $^1O_2^*$ ($\Phi_{^1O_2^*}$) is also higher in samples with lower average molecular weight DOM, as seen for ^{3}C* (Berg et al., 2019; Maizel and Remucal, 2017; Ossola et al., 2021; H. Wang et al., 2020). Some studies on the seasonal trend of $\Phi_{^1O_2^*}$ in surface waters hypothesized that summer samples where photodegradation is more rapid have higher $\Phi_{^1O_2^*}$ based on DOM photodegradation increasing $^1O_2^*$ quantum yields (McCabe and Arnold, 2016; Ossola et al., 2021; Sharpless et al., 2014). However, there are differences in singlet oxygen generation and concentrations between surface and atmospheric waters. For example, while ozonation and photodegradation of DOM enhances $\Phi_{^1O_2^*}$ in surface waters, photodegradation of aqueous particle extracts has no significant effect on $\Phi_{^1O_2^*}$

(Leresche et al., 2019, 2021; Sharpless et al., 2014). In addition, $\Phi_{^1O_2^*}$ in water extracts of PM_{10} collected in Switzerland shows a seasonal trend with low values in summer (Bogler et al., 2022); these authors also found that anthropogenic SOA is much more efficient in sensitizing $^1O_2^*$ than biomass burning organic aerosol (OA). Therefore, while some information is available, only a few studies have examined the seasonality of $^1O_2^*$ concentrations in particles or how this oxidant varies between particle types.

Although $^{\bullet}OH$, $^3C^*$, and $^1O_2^*$ are important in the transformation of atmospheric species, there are relatively few measurements of these photooxidants in atmospheric condensed phases, especially in extracts of ambient particles. In addition, very little is known about seasonal variations in these oxidant concentrations and kinetics. To address this gap, we collected $PM_{2.5}$ from November 2019 to October 2020 in Davis, CA; extracted the particles in water; and measured light absorption and photooxidant formation. This period included four main types of samples: winter samples influenced by residential wood combustion and high humidity, summer samples impacted by nearby wildfires (i.e., fresh biomass burning (BB) particles), summer samples impacted by more distant wildfires (i.e., aged BB particles), and spring/summer samples with little to no biomass burning. We measured photooxidant concentrations ($^{\bullet}OH$, $^1O_2^*$, $^3C^*$) in water extracts of the particles and investigated how photooxidant formation depends on particle type, optical properties, and biomass burning influence. Finally, building on the work of Kaur et al. (2019), we extrapolated our dilute extract results to predict photooxidant concentrations in aerosol liquid water (ALW) and assessed the importance of photooxidants in processing particulate organic compounds. This work is the last in a trio of connected papers examining oxidant generation in Davis particles. We use the kinetic measurements of Ma et al. (2023a) to extrapolate photooxidant concentrations from dilute solution to ALW conditions. In addition, results from our current work provided the samples and oxidant information for Jiang et al. (2023), who used aerosol mass spectrometry (AMS) and positive matrix factorization to identify five organic aerosol factors in the particles along with their AMS tracers and oxidant production potential.

2 Experimental methods

2.1 Chemicals

Furfuryl alcohol (FFA; 98 %), benzoic acid (BA; ≥ 99.5 %), *p*-hydroxybenzoic acid (*p*-HBA; 99 %), (phenylthio)acetic acid (PTA; 96 %), syringol (SYR; 99 %), 3,4-dimethoxybenzaldehyde (DMB; 99 %), and deuterium oxide (D_2O; 99.9 % D-atom) were received from Millipore Sigma. All chemical solutions and particulate matter extracts were prepared using air-saturated ultrapure water (Milli-Q water) from a Milli-Q Advantage A10 system (Millipore; ≥ 18.2 MΩ cm) that was pretreated with a Barnstead activated carbon cartridge.

2.2 Particle collection and extraction

More detailed descriptions of sampling and extraction procedures are provided in Ma et al. (2023a) and are only briefly discussed here. Fine particle ($PM_{2.5}$) sampling was conducted from November 2019 to October 2020 on the roof of Ghausi Hall on the University of California, Davis campus. Winter in Davis is humid and sometimes foggy, and the air quality is often impacted by residential wood combustion, while Davis in summer is hot and dry. During the summer of 2020, several severe wildfires occurred in northern California and Oregon, including the largest wildfires in the recorded history of California: the August complex (size: 4179 km^2), LNU Lightning Complex (1605 km^2), and SCU Lightning Complex (1470 km^2) (https://www.fire.ca.gov/incidents/2020; last access: 15 July 2022). These fires caused extremely heavy air pollution in Davis with daily $PM_{2.5}$ concentrations sometimes exceeding 80 $\mu g\,m^{-3}$ (https://www.arb.ca.gov/aqmis2/aqmis2.php, last access: 20 June 2022). Particles were collected with a high-volume sampler containing a PM_{10} inlet (Graseby Andersen) to remove PM larger than 10 µm, followed by two offset, slotted impactor plates (Tisch Environmental, Inc., 230 series) to remove particles larger than 2.5 µm. The resulting $PM_{2.5}$ was collected onto pre-cleaned Teflon-coated borosilicate glass microfiber filters (Pall Corporation, Emfab™ filters, 20.3 cm × 25.4 cm) and stored at −20 °C immediately after collection. The sampling duration was either 24 h or up to a week (Table S1 in the Supplement). The sampling campaign was paused from March to June 2020 because of COVID-related restrictions on campus activities.

To prepare particulate matter extracts (PMEs), filters were cut into 2 cm × 2 cm squares and then extracted with 1.0 mL Milli-Q water by shaking for 4 h in the dark. The extracts from the same filter were combined, filtered (0.22 µm PTFE; Pall), and adjusted to pH 4.2 by sulfuric acid to mimic the acidity of winter particle water in the Central Valley of California (Parworth et al., 2017). The acidity of extracts was measured by a pH microelectrode (MI-414 series, protected tip, Microelectrodes, Inc.). PMEs were flash-frozen in liquid nitrogen immediately after preparation and were later thawed on the day of the experiment. Particle mass extracted was determined by weighing filter squares before and after extraction with a microbalance (M2P, Sartorius); the extracted mass is an upper bound because we cannot account for insoluble material that is extracted from the square but removed by subsequent filtration. UV–Vis spectra of PMEs were measured with a Shimadzu UV-2501PC spectrophotometer in a 1 cm rectangular cuvette. Dissolved organic carbon (DOC) and major ions were measured by a total organic carbon analyzer (TOC-VCPH, Shimadzu) and ion chromatographs (881 Compact IC Pro, Metrohm) equipped with conductivity de-

tectors, respectively. PME sample information is provided in Table S1, while DOC and ion concentrations are in Table S2.

2.3 Sample illumination and chemical analysis

Illumination experiments were conducted using light from a 1000 W xenon arc lamp that was passed through optical filters to simulate tropospheric sunlight; details and the resulting light output are in Kaur et al. (2017). We spiked 1.0 mL of extract at pH 4.2 with a photooxidant probe and illuminated in a silicone-plugged GE 021 quartz tube (5 mm inner diameter, 1.0 mL volume) at 20 °C. Dark control samples were wrapped in aluminum foil and kept in the same photoreactor chamber. During illumination, aliquots were removed from the illuminated and dark tubes periodically to measure probe concentrations with high-performance liquid chromatography (HPLC; Shimadzu LC-20AB pump, Thermo Scientific Accucore XL C18 column (50 mm × 3 mm, 4 µm bead), and Shimadzu-M20A UV–Vis detector). In most cases, probe decay followed pseudo-first-order kinetics, as illustrated in Fig. S1 in the Supplement. The photon flux in an identical quartz tube was determined on each experiment day by measuring the photolysis rate constant of a 10 µM 2-nitrobenzaldehyde (2NB) solution (Galbavy et al., 2010).

2.4 Photooxidant measurements

Photooxidant methods are detailed in past papers (Anastasio and McGregor, 2001; Kaur and Anastasio, 2017; Ma et al., 2023a) and are only briefly described here. The uncertainty in an individual oxidant concentration is 1 standard error, determined by propagating the errors in the individual parameters required to calculate the concentration. Uncertainties in average values are 1 standard deviation, calculated from the spread of the individual values.

2.4.1 Hydroxyl radical ($^{\bullet}$OH)

$^{\bullet}$OH concentration was quantified using 10 µM benzoic acid (BA) as a probe and simultaneously monitoring the rates of probe decay and product (*p*-hydroxybenzoic acid, *p*-HBA) formation. For dilute samples (DOC < 15 mg C L^{-1}), 2 µM BA was used in order to not perturb the natural $^{\bullet}$OH sink in PME. Aliquots were taken during illumination to measure BA and *p*-HBA concentrations. From the BA probe loss, a linear regression of $\ln([BA]_t/[BA]_0)$ versus illumination time (t) was fitted, where $[BA]_0$ is the concentration at time zero. The negative value of the regression slope is the BA pseudo-first-order decay rate constant (k'_{BA}). The $^{\bullet}$OH concentration was then determined using

$$[^{\bullet}OH]_{exp} = \left[\frac{k'_{BA}}{k_{BA+^{\bullet}OH}}\right], \quad (1)$$

where $k_{BA+^{\bullet}OH}$ is the second-order rate constant of BA reacting with $^{\bullet}$OH at pH 4.2 (5.1×10^9 M^{-1} s^{-1}) (Ashton et al., 1995; Wander et al., 1968). Next, $[^{\bullet}OH]_{exp}$ was normalized to sunlight conditions at midday on the winter solstice at Davis (solar zenith = 62°, $j_{2NB,win} = 0.0070\,s^{-1}$) (Galbavy et al., 2010) and corrected for internal light screening due to absorption by chromophores in PME:

$$[^{\bullet}OH]_{win} = \left[\frac{[^{\bullet}OH]_{exp}}{S_\lambda \times j_{2NB,exp}}\right] \times j_{2NB,win},$$

where S_λ is the internal light screening factor in an individual sample (Table S1), and $j_{2NB,exp}$ is the photolysis rate constant of 2NB measured on the experiment day.

We also determined the $^{\bullet}$OH concentration in each sample from *p*-HBA formation. The initial formation rate of *p*-HBA was determined from the regression between *p*-HBA concentration and illumination time, using either a linear regression or a three-parameter exponential fit:

$$[p\text{-HBA}]_t = [p\text{-HBA}]_0 + a(1 - e^{-bt}), \quad (2)$$

where $[p\text{-HBA}]_t$ and $[p\text{-HBA}]_0$ are the measured concentrations at illumination times t and zero, respectively, and a and b are regression fit parameters. With this fitting, the initial formation rate of *p*-HBA, R_p, is calculated with

$$R_p = a \times b, \quad (3)$$

and then the $^{\bullet}$OH concentration was calculated using

$$[^{\bullet}OH]_{exp} = \frac{R_p}{[BA]_0 \times k_{BA+^{\bullet}OH} \times Y_{p\text{-HBA}}}, \quad (4)$$

where $Y_{p\text{-HBA}}$ (0.18) is the yield of *p*-HBA from the reaction of BA with $^{\bullet}$OH (Anastasio and McGregor, 2001). $^{\bullet}$OH concentrations were normalized by j_{2NB} and the light screening factor using Eq. (2). In some samples, BA decay and *p*-HBA formation were faster at the beginning of illumination and then slowed (e.g., Fig. S2), indicating an initially higher $^{\bullet}$OH concentration compared to later times, as seen previously (Paulson et al., 2019). For each sample we generally used all data points for the regressions of BA and *p*-HBA and then determined the reported $[^{\bullet}OH]$ as the average of the BA and *p*-HBA results (Table S3).

2.4.2 Singlet molecular oxygen ($^1O_2^*$)

To determine $^1O_2^*$ concentrations, FFA was used as a probe, and deuterium oxide (D_2O) was used as a diagnostic tool (Anastasio and McGregor, 2001) because $^1O_2^*$ decays more rapidly in H_2O than D_2O. Therefore, the difference in FFA decay rates in H_2O and D_2O is attributed to $^1O_2^*$ (instead of other oxidants). For each sample, 1.0 mL of PME was divided into two 0.5 mL aliquots, one diluted with 0.5 mL H_2O and the other 0.5 mL D_2O. A total of 10 µM FFA was spiked into both solutions, and pseudo-first-order rate constants of FFA loss during illumination were determined (k_{exp,H_2O} and k_{exp,D_2O}). The difference between the FFA first-order rate

constants was used to calculate the steady-state $^1O_2^*$ concentration (Anastasio and McGregor, 2001). This experimental $^1O_2^*$ concentration was normalized by photon flux and light screening factors of PME using an analog of Eq. (2) to determine $^1O_2^*$ winter solstice values (Table S4). For roughly 90 % of our experiments, decay of FFA and our triplet probes (see below) followed first-order kinetics (e.g., Fig. S1).

2.4.3 Oxidizing triplet excited states of organic matter ($^3C^*$)

Oxidizing triplets were measured with two probes, syringol (SYR) and (phenylthio)acetic acid (PTA). SYR reacts rapidly with all oxidizing triplets, but its decay by $^3C^*$ can be inhibited by high concentrations of dissolved organic matter (DOM) (Ma et al., 2023a, b; Maizel and Remucal, 2017; McCabe and Arnold, 2017). In contrast, PTA is more resistant to this inhibition, but it can only capture strongly oxidizing triplets (Ma et al., 2023b). To determine $^3C^*$ concentrations, two 1.0 mL aliquots of PME were spiked with 10 µM of either SYR or PTA and then illuminated to determine the pseudo-first-order rate constant for loss of each probe ($k'_{P,exp}$). We then removed the contributions of direct photodegradation, $^\bullet OH$, and $^1O_2^*$ to triplet probe decay (Ma et al., 2023a). Since $^3C^*$ is a complex mixture of triplets with a wide range of reactivities, there is no exact value for the second-order rate constant of $^3C^*$ in PME reacting with probes. Our past work indicated that $^3C^*$ in Davis winter PM has a similar average reactivity to the triplet state of DMB (Kaur and Anastasio, 2018; Kaur et al., 2019), which is a component of BB BrC (Fleming et al., 2020; Schauer et al., 2001). However, it is possible that this model compound is more reactive than natural oxidizing triplets, which would lead to an underestimate of $^3C^*$ (Ma et al., 2023b). We quantified the inhibition effect of DOM on the decay of SYR and PTA by measuring inhibition factors of each probe ($IF_{P,corr}$) in each sample and used them to correct $^3C^*$ concentrations (Canonica and Laubscher, 2008; Ma et al., 2023b; McCabe and Arnold, 2017; Wenk et al., 2011). Details about determining inhibition factors and correcting $^3C^*$ concentrations are provided in Sect. S1 in the Supplement. $^3C^*$ concentrations in PME during each experiment were calculated with

$$[^3C^*]_{P,exp} = \frac{k'_{P,^3C^*}}{k_{P+^3DMB^*} \times IF_{P,corr}}, \quad (5)$$

where $k_{P+^3DMB^*}$ is the second-order rate constant of probes with $^3DMB^*$ (Table S5). These values were converted to $^3C^*$ concentrations expected at midday of the winter solstice in Davis (after correction for internal light screening) using an equation analogous to Eq. (2); these are the concentrations reported in the main text. Details of $^3C^*$ measurements by SYR and PTA are in Tables S7 and S8, respectively.

2.4.4 Extrapolating extract results to aerosol liquid water conditions

Photooxidant concentrations in PM extracts represent dilute conditions similar to cloud/fog waters, while our goal is to estimate photooxidant concentrations in aerosol liquid water, which is orders of magnitude more concentrated. To predict photooxidant concentrations in ALW, we quantified photooxidant kinetics (i.e., oxidant formation rates and loss rate constants) for each sample type as a function of particle mass concentration and then extrapolated to ALW conditions (Kaur et al., 2019; Ma et al., 2023a). Details about the extrapolations are provided in Sect. S4.

3 Results and discussion

3.1 General extract characteristics

To investigate the seasonal variation in photooxidant formation, we studied 18 $PM_{2.5}$ samples across a year of sampling. Samples were from all seasons, but there was only one spring sample because of COVID restrictions from March through June of 2020 (Fig. 1 and Table S1). Most particle samples were collected for 24 h, while four of the winter samples were collected for 7 d to obtain more particle mass. Winters were marked by residential wood burning and high relative humidities, while the summer samples represented both periods influenced by fresh and aged biomass burning (from wildfires) and clean conditions. From August to October 2020, Davis periodically experienced severe air pollution caused by wildfires in California and Oregon. Section S2 provides satellite images with fire points detected by satellite and 24 h back trajectories estimated on the day of sampling for wildfire periods (Rolph et al., 2017; Stein et al., 2015). Based on the satellite images and back trajectories, smoke plumes were transported from their sources to Davis in as short as 1–2 h, which we classify as fresh wildfire samples, or as long as 12–24 h or more, which represent aged wildfire particles.

Figure 1 shows the average $PM_{2.5}$ concentration during each extract sampling period. We categorized the 18 samples into four groups based on sampling date and positive matrix factorization (PMF) results obtained using UV–Vis absorption spectra and aerosol-mass-spectrometer chemical characterization (Jiang et al., 2023). The first group is termed winter and spring samples (Win-Spr), which were collected from November 2019 to March 2020 and have an average $PM_{2.5}$ concentration of 9.9 ($\pm$ 1.5) µg m^{-3} (Table S1). Three samples collected in July, August, and October without wildfire influence are classified as summer and fall samples (Sum-Fall), with an average $PM_{2.5}$ of 7.4 ($\pm$ 0.4) µg m^{-3}. The seven wildfire-influenced samples collected from August to October are classified as fresh biomass burning (FBB) or aged biomass burning (ABB), with average $PM_{2.5}$ values of 55 ($\pm$ 10) and 24 ($\pm$ 8) µg m^{-3}, respectively. The PMF results

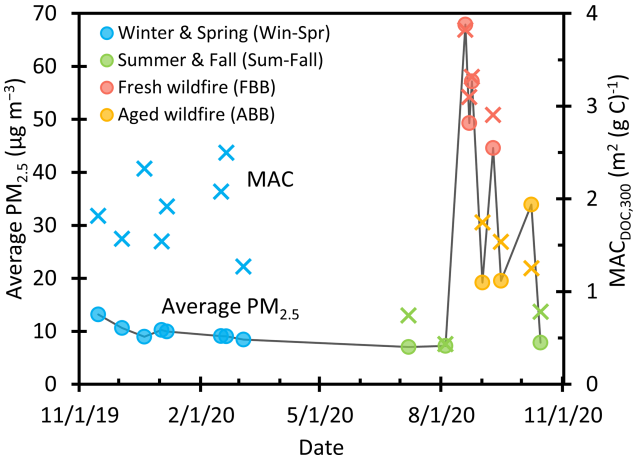

Figure 1. Average $PM_{2.5}$ concentrations (circles) during each sampling period and DOC-normalized mass absorption coefficients at 300 nm (×) in particle extracts for winter and spring samples (blue), summer and fall samples (green), fresh biomass burning (red), and aged biomass burning (yellow). The sampling date format is mm/dd/yy; e.g., the first sample was collected on 15 November 2019. $PM_{2.5}$ concentrations were measured roughly 2 km west of our sampling site by the California Air Resources Board and were retrieved from the AQMIS online database (California Air Resources Board AQMIS Database; https://www.arb.ca.gov/aqmis2/aqmis2.php, last access: 12 July 2022.)

indicate that FBB samples are dominated by biomass burning organic aerosol factors characterized by elevated levels of levoglucosan (m/z 60) signature ions in the AMS mass spectra (Alfarra et al., 2007). ABB samples were also collected during the wildfire-influenced period, but they are dominated by an oxidized organic aerosol factor with high O/C ratio and little levoglucosan (Jiang et al., 2023).

Our PM extracts are much more dilute than aerosol liquid water in the ambient atmosphere, a result of physical limitations on the amount of water we need to extract and study particle photochemistry. Particle mass / liquid water mass ratios of our extracts were in the range (0.7–4.1) $\times 10^{-4}$ μg PM / μg H_2O for 1 d samples (Fig. S10 in the Supplement) and correlated well with the ambient $PM_{2.5}$ concentrations (Table S1). The 7 d winter samples had higher particle mass / water mass ratios, up to 9.1×10^{-4} μg PM/μg H_2O. Based on the PM mass concentrations, our particle extracts are similar to dilute atmospheric waters such as cloud and fog drops (10^{-5}–10^{-3} μg PM/μg H_2O), instead of concentrated particle liquid water (roughly 1 μg PM/μg H_2O) (Nguyen et al., 2016; Seinfeld and Pandis, 2016).

Dissolved-organic-carbon concentrations in the extracts range from 5 to 192 mg C L^{-1} (Table S1). The ratio of organic carbon (OC) mass to total extracted PM mass is high in the wildfire samples, with average values of 31 (± 6) % and 26 (± 6) % for FBB and ABB, respectively. These fractions are lower than values for BB particles in other studies (43 %–59 %) (Schauer et al., 2001; Vicente et al., 2013), probably because we used water as the extraction solvent, thereby missing water-insoluble organics. The OC/PM fractions for Win-Spr and Sum-Fall samples are similar to each other, with values of 16 (± 5) % and 11 (± 3) %, respectively. Win-Spr PMEs have high concentrations of nitrate (NO_3^-), 84–3300 μM (Table S2), which contributed up to 33 % of PM mass. PMEs in the other three groups have nitrate concentrations from 25 to 300 μM, which are less than 10 % of PM mass. Win-Spr samples also have the highest ammonium concentrations, 168–4900 μM, followed by wildfire-influenced samples (46–803 μM), and Sum-Fall samples (< 100 μM). Potassium, a marker of biomass burning (Silva et al., 1999), has its highest concentrations in winter and wildfire samples with a range of 62–220 μM. The Sum-Fall samples have the highest fraction of sodium with an average of 11 %, suggesting the influence of sea salt (Parworth et al., 2017). We employed three field blanks in this study at the beginning, middle, and end of the sampling campaign. In field blanks, ions and DOC concentrations are less than 10 % of their concentrations in most PME samples, though FB1 was contaminated by the filling solution of a pH electrode, resulting in extremely high chloride concentrations (Table S2).

3.2 Light absorption in particle extracts

DOC-normalized mass absorption coefficients (MACs) at 300 nm ($MAC_{DOC,300}$) are shown in Fig. 1. For wildfire samples, MAC is correlated with the $PM_{2.5}$ concentration, which probably reflects the dominant influence of BB emissions on both PM levels and light absorbance since FBB has the highest MAC among sample types, with an average of 3.3 (± 0.4) per gram C. This is expected because fresh biomass burning organic aerosol (BBOA) contains abundant amounts of highly light-absorbing products, including substituted aromatics with high unsaturation and nitroaromatics (Budisulistiorini et al., 2017; Claeys et al., 2012; Fleming et al., 2020; Hettiyadura et al., 2021; Lin et al., 2016, 2017). The average MAC for FBB at 365 nm is 1.2 (± 0.4) m^2 per gram C, similar to past values determined in water extracts of biomass burning particles (0.9–1.4 m^2 per gram C) (Du et al., 2014; Fan et al., 2018; Park and Yu, 2016). At 300 nm, the average MAC of ABB is 1.5 (± 0.3) m^2 per gram C, half the value of FBB, likely because of photobleaching of brown carbon during aging (Hems and Abbatt, 2018; Hems et al., 2021; Laskin et al., 2015; Wong et al., 2017; Zhao et al., 2015). Win-Spr has an average $MAC_{DOC,300}$ (1.9 (± 0.4) m^2 per gram C) that is 3 times higher than that of Sum-Fall (0.65 (± 0.19) m^2 per gram C), though they have similar $PM_{2.5}$ concentrations. This indicates that winter wood combustion can significantly enhance light absorption by particles. Our winter MAC value is similar to the average value (2.2 (± 0.7) m^2 per gram C) de-

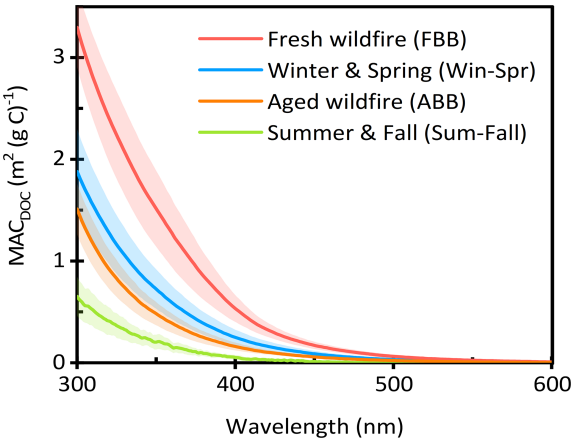

Figure 2. Average DOC-normalized mass absorption coefficients for fresh wildfire samples (red), winter and spring samples (blue), aged wildfire samples (orange), and summer and fall samples (green). Each shaded area represents ± 1 standard deviation.

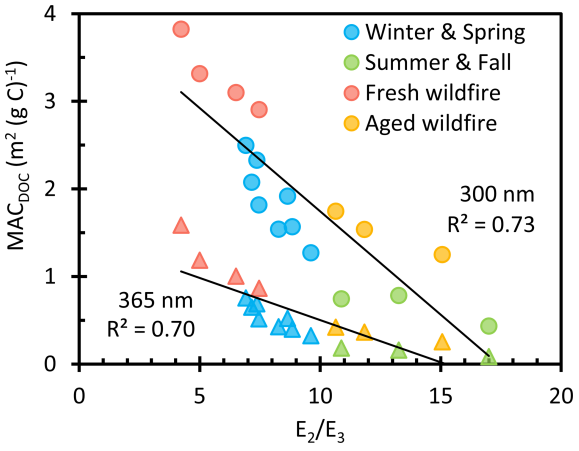

Figure 3. Mass absorption coefficients of dissolved organic carbon at 300 nm (circles) and 365 nm (triangles) as a function of E_2/E_3 for each sample type. Solid lines represent linear regressions.

termined in previous water extracts of Davis winter particles (Kaur et al., 2019).

We also calculated the average MAC_{DOC} for each sample type in the wavelength range of 300–600 nm, as shown in Fig. 2. Fresh wildfire samples have the highest MAC values across the wavelength range and the lowest absorption Ångström exponent (AAE; 300–450 nm), which is 7.3 (± 0.2). ABB shows slightly lower MAC values than Win-Spr. This might be explained by faster rates of aging and photobleaching during summer as well as higher amounts of less absorbing SOA. AAE values of ABB and Win-Spr are similar, 7.7 (± 0.3) and 7.9 (± 0.3), respectively, and are comparable to previously reported values of water-soluble organic carbon from biomass burning (Du et al., 2014; Hecobian et al., 2010; Lin et al., 2017). Sum-Fall has the lowest MAC but the highest AAE (9.1 (± 0.5)). There are several similarities between our average sample-type MAC values in Fig. 2 and the MAC values for the five OA types determined from positive matrix factorization (PMF) on the PM extracts (Jiang et al., 2023). Most notably, our fresh and aged wildfire spectra in Fig. 2 are very similar to the fresh and aged BBOA spectra determined by PMF, while our Sum-Fall average is comparable to the three oxidized OA factors of Jiang et al. (2023).

An optical property frequently used to characterize surface water DOM is E_2/E_3, which is the ratio of absorbance at 250 nm to that at 365 nm. In surface waters, this ratio is an indicator of the molecular weight of dissolved organic matter, with low E_2/E_3 representing high-molecular-weight DOM (Ossola et al., 2021). E_2/E_3 in our PMEs ranges from 4.2 to 17 and is related to MAC values: as shown in Fig. 3, MAC decreases with increasing E_2/E_3; i.e., absorbance decreases as DOM molecular weight decreases. FBB has the lowest average E_2/E_3 (5.8 (± 1.5)) of our sample types, including ABB (12.5 (± 2.3)), which suggests that organic molecules in fresh BB are fragmented during aging. This is consistent with the observation that high-molecular-weight compounds are less abundant in aged BBOA (Farley et al., 2022), as well as studies showing that ozone exposure leads to an increase in E_2/E_3 and a decrease in molecular weight of surface water DOM (Buckley et al., 2023; Leresche et al., 2019). Therefore, E_2/E_3 may be an easy and effective indicator to differentiate fresh and aged samples. E_2/E_3 ratios for the Win-Spr samples are intermediate between the summer fresh and aged BB samples, again suggesting that these biomass-burning-influenced winter samples are less aged than ABB.

Since the light absorption of methanol extracts of particles is usually greater than that of water extracts (Liu et al., 2013; Zhang et al., 2013), we also examined the absorbance of a FBB filter extracted with different solvents (water, methanol, and hexane). As shown in Fig. S11, the absorbance of the methanol (MeOH) extract is more than twice as high as the water extract and 5 times higher than the hexane extract, indicating that this FBB contains a high fraction of organic-soluble brown carbon. We also did a sequential extraction with this FBB sample and with a Win-Spr sample, with first, second, and third extraction solvents of water, methanol, and hexane, respectively. The UV–Vis spectra and PM mass extracted for each solvent extraction are shown in Fig. S12. For the Win-Spr and FBB samples, the PM mass recovered by the second extraction (in methanol) is only 20 % and 56 % of the mass by the first extraction (in water), respectively, but the MeOH extract absorbance at 365 nm is similar to or even greater than the water extract. This is consistent with a previous study of sequential extraction with US western wildfire samples (Zeng et al., 2022), which found that water-insoluble brown carbon (e.g., polycyclic aromatic hydrocarbons) is highly light-absorbing, despite accounting for little of the PM mass. The high light absorption in methanol extracts suggests

that the water-insoluble chromophores have high potential to produce photooxidants, although this requires further study since methanol can react with some chromophores, altering light absorption by BrC (Chen et al., 2022). Regardless, since the oxidant probes we use were developed for aqueous and not organic solutions, we did not study photooxidant generation in methanol or hexane extracts.

3.3 Photooxidant concentrations

3.3.1 Normalization by sample duration

While most of our PM samples were collected for 1 d, we also collected four samples for 7 d, which resulted in extracts that were more concentrated and that had higher oxidant concentrations. To properly compare these longer samples with the rest, we normalized photooxidant concentrations in the 7 d samples to what would be expected for a 24 h sample. For $^1O_2^*$ and $^3C^*$, the production rate is proportional to the brown carbon mass (Faust and Allen, 1992; Kaur et al., 2019), and so we normalized their concentrations by dividing by the duration of sampling (i.e., number of sampling days). The case for the hydroxyl radical is more complicated, since past work has found that the $^\bullet$OH concentration can be independent of extract concentration (Arakaki et al., 2013; Kaur et al., 2019), but unnormalized $^\bullet$OH concentrations in our 7 d samples are clearly higher than in the adjacent 24 h samples (Fig. S13). If we normalize $^\bullet$OH using the same method as for $^1O_2^*$ and $^3C^*$ (i.e., by the duration of sampling), the resulting $^\bullet$OH concentrations are lower than the adjacent 24 h samples (Fig. S13). To obtain more reasonable estimates for [$^\bullet$OH] in the 7 d samples, we fitted the plot of $^\bullet$OH concentration versus particle mass / water mass ratio for Win-Spr samples with a linear regression (Fig. S14) and then used the regression to estimate $^\bullet$OH concentrations in the 7 d samples using the time-normalized particle mass / water mass ratio values (i.e., the measured particle mass / water ratio divided by 7).

3.3.2 Hydroxyl radical ($^\bullet$OH)

As shown in Fig. 4a, normalized $^\bullet$OH concentrations have a range of (0.2–3.2) $\times 10^{-15}$ M. The values are similar to those in illuminated particle extracts from Davis and Colorado (Kaur et al., 2019; Leresche et al., 2021) but much higher than those in illuminated extracts of lab SOA and PM_{10} from Switzerland (2.2–4.9) $\times 10^{-17}$ M) that had low DOC (5 mg C L^{-1}) (Manfrin et al., 2019). Among our four sample types, fresh biomass burning samples have the highest average [$^\bullet$OH], 2.5 ($\pm$ 0.3) $\times 10^{-15}$ M, while aged BB particles have a similar average concentration that is statistically indistinguishable, 1.7 ($\pm$ 1.4) $\times 10^{-15}$ M. This is parallel to a previous finding that BBOA, compared to other types of organic aerosols, has the highest oxidative potential as measured by the dithiothreitol (DTT) assay, and this potential decreases with simulated atmospheric aging (Verma et al., 2015; Wong et al., 2019). Win-Spr has a similar average [$^\bullet$OH], 1.5 ($\pm$ 0.3) $\times 10^{-15}$ M, while Sum-Fall is the lowest at 0.4 ($\pm$ 0.3) $\times 10^{-15}$ M. Our winter values are roughly 3 to 4 times higher than average values in previous Davis winter particle extracts and fog waters (0.51 ($\pm$ 0.24) $\times 10^{-15}$ M and 0.42 ($\pm$ 0.07) $\times 10^{-15}$ M, respectively) (Kaur and Anastasio, 2017; Kaur et al., 2019). While nitrate and nitrite can be important sources of $^\bullet$OH in atmospheric waters (Anastasio and McGregor, 2001; Kaur and Anastasio, 2017; Kaur et al., 2019; Leresche et al., 2021), these species account for less than 10 % of $^\bullet$OH in most of our current samples (Table S3). In our kinetic experiments, in 6 of our 18 samples (5 winter samples and 1 wildfire sample) BA decayed faster at the beginning of irradiation but was slower at later times, with a rate difference of up to a factor of 3.4 (Fig. S2). This indicates that [$^\bullet$OH] in some samples is higher during the initial stage of irradiation, possibly because a portion of the compounds that produce $^\bullet$OH are labile and undergo rapid

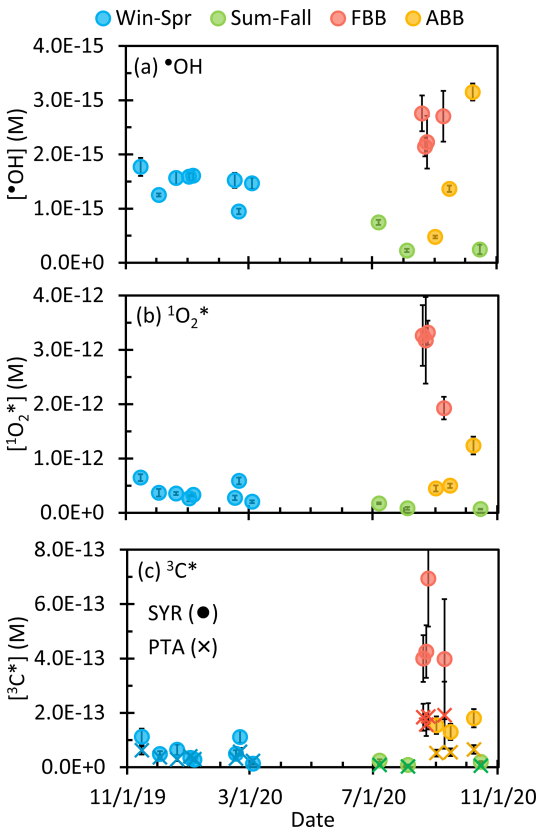

Figure 4. Steady-state concentrations of **(a)** the hydroxyl radical, **(b)** singlet molecular oxygen, and **(c)** oxidizing triplet excited states of organics determined by syringol (circles) and (phenylthio)acetic acid (crosses) in particle extracts. Concentrations are all normalized by sampling duration and to midday winter solstice sunlight in Davis to highlight seasonal differences in particle reactivity; the equivalent plots with concentrations calculated for the midday sunlight of each sample collection period are shown in Fig. S15. Sample dates are mm/dd/yy.

decomposition. A similar effect was seen in biomass burning aerosols from Fresno, CA, where a burst of $^{\bullet}$OH was observed within the first few minutes of irradiation and was hypothesized to be due to the decomposition of peroxides through photo-Fenton reactions (Paulson et al., 2019).

Figure 5a shows $^{\bullet}$OH concentration as a function of dissolved organic carbon for the four sample types. For comparison, we also include data from Kaur et al. (2019), who measured photooxidant concentrations in Davis winter particle extracts. Though samples in Kaur et al. (2019) have similar values of DOC to our 24 h Win-Spr samples, their [$^{\bullet}$OH] is 5 times lower and independent of DOC. While $^{\bullet}$OH appears to increase with DOC for our samples (Fig. 5a), the data are noisy, and the linear correlation is weak ($R^2 = 0.40$). A previous study on Minnesota surface waters observed a logarithmic relationship between [$^{\bullet}$OH] and absorbance coefficient at 440 nm (Chen et al., 2020), which in turn was correlated to DOC. They speculated that this is because the dominant $^{\bullet}$OH sink changes from bicarbonate/carbonate to DOC with increasing DOC levels, but bicarbonate and carbonate are negligible sinks in our extracts since they are acidic (pH 4.2). [$^{\bullet}$OH] in FBB is independent of DOC, but the three ABB samples show $^{\bullet}$OH increasing with DOC. We also found that [$^{\bullet}$OH] increases with DOC in a dilution series of summer wildfire PM and hypothesized that $^{\bullet}$OH production is a bimolecular reaction (primarily Fe(II) + HOOH) that increases with the square of PM mass concentration (Ma et al., 2023a). This might also explain our current ABB results.

3.3.3 Singlet molecular oxygen ($^1O_2^*$)

Winter-solstice-sunlight-normalized $^1O_2^*$ has a concentration range of (0.7–32) $\times 10^{-13}$ M (Fig. 4b) and correlates well with ambient $PM_{2.5}$ concentration (Fig. S16). These concentrations are similar to the wide range of previously reported values in particle extracts, (0.6–22) $\times 10^{-13}$ M (Bogler et al., 2022; Kaur et al., 2019; Leresche et al., 2021), but are roughly 100 times higher than concentrations in illuminated extracts of biogenic and anthropogenic SOA, (0.8–45) $\times 10^{-15}$ M (Manfrin et al., 2019). Our higher $^1O_2^*$ concentrations are only partially explained by our 1–40 times higher DOC concentrations; the remaining difference is likely due to greater light absorption by our samples. Our values are also similar to [$^1O_2^*$] in solutions of dissolved soot illuminated with simulated sunlight, (0.6–65) $\times 10^{-13}$ M (Li et al., 2019), even though their samples absorbed very little light. Among our samples, fresh BB has the highest average [$^1O_2^*$], followed by ABB, with values of 29 ($\pm$ 7) $\times 10^{-13}$ M and 7.3 ($\pm$ 0.4) $\times 10^{-13}$ M, respectively. Leresche et al. (2021) found that [$^1O_2^*$] decreased by a factor of 2 in particle extracts after sunlight irradiation, which is consistent with our observation that aged particle extracts have lower [$^1O_2^*$]. Win-Spr and Sum-Fall samples have average [$^1O_2^*$] values of 3.8 ($\pm$ 1.6) $\times 10^{-13}$ M and 1.1 ($\pm$ 0.6) $\times 10^{-13}$ M, respectively. The higher Win-Spr concentrations are probably because of the influence of biomass burning.

As shown in Fig. 5b, $^1O_2^*$ concentrations linearly increase with DOC ($R^2 = 0.93$), consistent with our understanding that organic matter is the primary source of $^1O_2^*$ (Bogler et al., 2022; Kaur and Anastasio, 2017; Kaur et al., 2019; Ossola et al., 2021). Moreover, all four types of samples share the same slope, suggesting that the relationship between [$^1O_2^*$] and DOC is independent of particle type or chemical composition, which is somewhat surprising given the large differences in DOC-normalized light absorption for the different sample types (Fig. 2). When plotting [$^1O_2^*$] as a function of absorbance at 300 and 365 nm (Figs. S17b and S18b, respectively), we do observe differences among sample types. In these plots, Win-Spr samples present a steeper slope (as do samples from Kaur et al., 2019) compared to wildfire samples, consistent with our previous work (Ma et al., 2023a). The $^1O_2^*$ concentrations in previous Davis winter particle extracts (Kaur et al., 2019) also follow the linear regression of this work. While this suggests that DOC is a robust descriptor for $^1O_2^*$ concentrations, most of our particle samples were influenced by biomass burning. Other particle types, such as anthropogenic SOA, biogenic SOA, and emissions from fossil fuel combustion, appear to have different relationships between $^1O_2^*$ and DOC, as suggested by results from Manfrin et al. (2019), Ma et al. (2023a), and Bogler et al. (2022).

3.3.4 Oxidizing triplet excited states of brown carbon ($^3C^*$)

We used two probes – syringol (SYR) and (phenylthio)acetic acid (PTA) – to quantify oxidizing triplet excited states. SYR reacts rapidly with both strongly and weakly oxidizing triplets, while PTA is only reactive with strongly oxidizing triplets (Ma et al., 2023b). However, syringol has a disadvantage that its decay by $^3C^*$ can be inhibited by dissolved organic matter, while PTA is largely resistant to this inhibition (Ma et al., 2023b; Maizel and Remucal, 2017; McCabe and Arnold, 2017; Wenk et al., 2011). As shown in Fig. 4c, winter-solstice-normalized (and inhibition-corrected) $^3C^*$ concentrations have a range of (0.13–6.9) $\times 10^{-13}$ M as determined by SYR and (0.03–1.9) $\times 10^{-13}$ M by PTA. The $^3C^*$ concentration follows $PM_{2.5}$ concentration well, with low values during non-wildfire periods and very high values during wildfire-influenced periods (Fig. S16). For nearly all samples, $[^3C^*]_{SYR}$ is higher than $[^3C^*]_{PTA}$. As seen for $^1O_2^*$, FBB has the highest average [$^3C^*$], 4.8 ($\pm$ 1.4) $\times 10^{-13}$ M from SYR and 1.8 ($\pm$ 1.6) $\times 10^{-13}$ M from PTA, due to the high organic amounts in these samples. Relative to the FBB average, the FBB, ABB, Win-Spr, and Sum-Fall samples have triplet concentration ratios of 1 : 0.32 : 0.12 : 0.04 as determined by SYR and 1 : 0.32 : 0.21 : 0.03 as determined by PTA. These ratios are similar to the ratio of average DOC concentrations, which is 1 : 0.45 : 0.15 : 0.08, indicating that

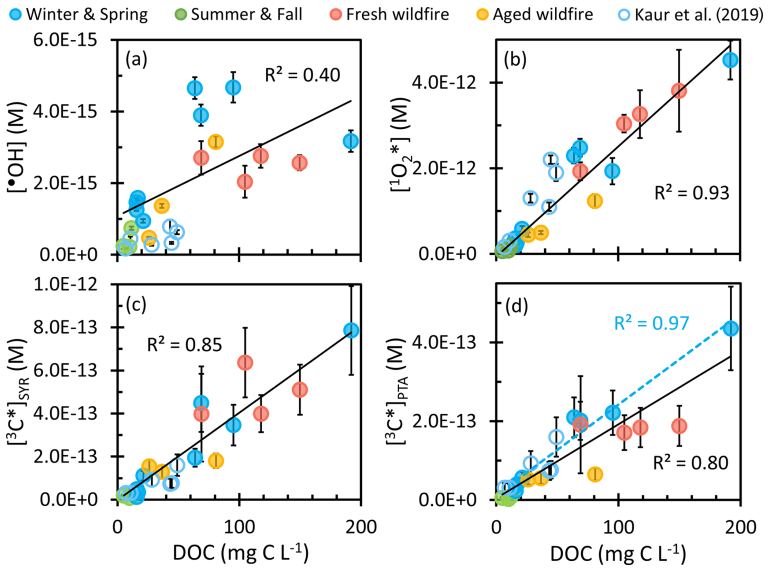

Figure 5. Steady-state concentrations of **(a)** the hydroxyl radical, **(b)** singlet molecular oxygen, and oxidizing triplet excited states of organic matter determined by **(c)** syringol and **(d)** (phenylthio)acetic acid as a function of dissolved organic matter for each sample type (solid circles). Previous measurements made in Davis winter particle extracts are in open circles (Kaur et al., 2019). Solid black lines are linear regressions between oxidant concentrations in this work and DOC. The dashed blue line in **(d)** is the linear regression of the Win-Spr samples. Error bars represent standard error propagated from linear regression and error in rate constants. Oxidant concentration values are not normalized by the sampling duration.

DOC is the main driver of $^3C^*$ concentration differences among sample types. This relationship is complicated at high DOC, where dissolved organics can be the dominant triplet sink (up to roughly 60 % of the total sink), larger than the contribution from dissolved oxygen.

Figure 5c shows the correlation between $[^3C^*]_{SYR}$ and DOC for our samples, along with data from Kaur et al. (2019). $[^3C^*]_{SYR}$ linearly increases with DOC ($R^2 = 0.83$) independent of sample type, likely because SYR reacts rapidly with a wide range of oxidizing triplets (Kaur and Anastasio, 2018). However, Figs. S17c and S18c show some differences between sample types in the relationship between $[^3C^*]_{SYR}$ and absorbance at 300 or 365 nm, with Win-Spr samples having a steeper slope. However, the trend of FBB samples is hard to discern, in part because there are only four samples. As shown in Fig. 5d, $[^3C^*]_{PTA}$ also linearly increases with DOC, though the correlation is not as good as those for $[^1O_2^*]$ or $[^3C^*]_{SYR}$. Win-Spr samples present a slightly higher slope than wildfire samples (FBB and ABB); oddly, $[^3C^*]_{PTA}$ is nearly independent of DOC within either biomass burning group. The steeper slope of $[^3C^*]_{PTA}$ with DOC for the Win-Spr samples suggests that these samples contain a higher fraction of highly oxidizing $^3C^*$ than the wildfire samples. This difference in slopes is particularly noticeable in Figs. S17d and S18d, where $[^3C^*]_{PTA}$ is plotted against absorbance at 300 or 365 nm.

Since PTA only captures $^3C^*$ that has high reduction potential, while SYR reacts rapidly with both strongly and weakly oxidizing triplets, the ratio $[^3C^*]_{PTA} / [^3C^*]_{SYR}$ provides an estimate of the fraction of oxidizing $^3C^*$ consisting of strong oxidants. As shown in Fig. 6, the ratio $[^3C^*]_{PTA} / [^3C^*]_{SYR}$ ranges from 0.27 ($\pm$ 0.10) to 1.7 ($\pm$ 0.7) with an average value of 0.58 ($\pm$ 0.38), indicating that roughly 60 % of oxidizing triplets are strong oxidants. The Win-Spr samples have an average ratio of 0.86 ($\pm$ 0.43), significantly higher than the rest of the samples (0.37 $\pm$ 0.07), indicating that they produce a higher fraction of strongly oxidizing $^3C^*$. Precursors for more oxidizing triplets include quinones, aromatic ketones, and aromatic aldehydes, while weakly oxidizing triplet precursors include polycyclic aromatic compounds (McNeill and Canonica, 2016).

We can also gain some insight into extract compositions from the inhibition factors (IFs) (Sect. S1) for SYR and PTA in each sample. An IF of 1 represents no inhibition of probe decay by the sample, while an IF of 0 indicates that the triplet-mediated decay of the probe is completely reversed by DOM in the sample (Canonica and Laubscher, 2008; Ma et al., 2023b). Among our samples, the IF for SYR ($IF_{SYR,corr}$) ranges from 1.2 to 0.21, with an average value of 0.64 ($\pm$ 0.29) (Table S6 and Fig. S19). This indicates that SYR decay by $^3C^*$ in PME can be heavily inhibited, suggesting that our PMEs contain abundant antioxidants such as phenolic moieties (Wenk and Canonica, 2012; Wenk et al., 2011). As shown in Fig. S19b, $IF_{SYR,corr}$ generally decreases with increasing DOC, consistent with previous surface water studies (Canonica and Laubscher, 2008; McCabe and Arnold, 2017). We fit $IF^{-1}_{SYR,corr}$ versus DOC using a linear regression with all samples (Ma et al.,

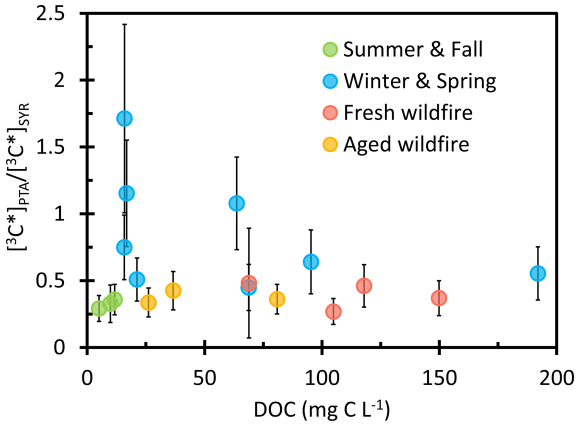

Figure 6. The ratio of oxidizing triplet excited state concentrations determined by PTA to those determined by SYR as a function of DOC for each sample type.

2023b; Wenk et al., 2011), as shown in Fig. S19b. The fitted slope is 0.015 L per milligram C; the inverse of this slope, 67 ($\pm$ 13) mg C L^{-1}, represents the DOC concentration that causes $IF_{SYR,corr}$ to equal 0.5. All the sample groups essentially fit on the same line. The IF for PTA ($IF_{PTA,corr}$) ranges from 1.5 to 0.6, with an average value of 1.1 ($\pm$ 0.2), demonstrating its better resistance to inhibition (Fig. S19c). We also measured the inhibition factor of furfuryl alcohol (IF_{FFA}) as the indicator of the ability of DOM in PME to quench ^{3}C* (Fig. S19a). IF_{FFA} decreases with increasing DOC, ranging from 1.4 (i.e., no quenching of triplets by PME DOM) to 0.5 (i.e., DOM reduces the triplet concentration to 50 % of its non-quenched value). From the linear fit between IF_{FFA}^{-1} and DOC, we obtain a second-order rate constant of DOM-quenching ^{3}DMB* (Ma et al., 2023b; Wenk et al., 2011, 2013) of 2.7 ($\pm$ 0.7) $\times$ 10^7 L (mol C^{-1}) s^{-1}. This value is somewhat lower than rate constants of DOM-quenching oxidizing ^{3}C* in two previous Davis particle extracts (5.7–12) $\times$ 10^7 L (mol C)$^{-1}$ s^{-1}) (Ma et al., 2023a) but in the range of values for DOM-quenching ^{3}C* in surface waters (1.3–7.9) $\times$ 10^7 L (mol C)$^{-1}$ s^{-1}; Wenk et al., 2013).

3.3.5 Normalization by photon flux

Photooxidant concentrations in Figs. 4 and 5 are all normalized to the same actinic flux condition (i.e., solar noon on the winter solstice in Davis, CA, $j_{2NB} = 0.007$ s^{-1}) to highlight seasonal differences in particle reactivity. However, photon fluxes vary throughout the year, which will affect the rate of photooxidant formation and accompanying concentration. To account for this effect, we calculated midday j_{2NB} values as a function of date during our sampling campaign, as shown in Fig. S20 and described in Sect. S3. The estimated j_{2NB} value at midday of the summer solstice is 0.013 s^{-1}, which is nearly twice the value during winter. Next, we estimated midday j_{2NB} values for each sampling day and normalized photooxidant concentrations to the corresponding sunlight condition. Figure S15 shows the equivalent plot of Fig. 4 after photon flux normalization, which increased oxidant concentrations by factors ranging from 1.0 to 1.9. The average normalization factors for FBB and Sum-Fall samples are 1.7, while ABB and Win-Spr have average factors of 1.5 and 1.2, respectively. These j_{2NB} values do not account for optical confinement of sunlight within particles; recent work suggests that this will enhance in-particle actinic fluxes by approximately a factor of 2 (Corral Arroyo et al., 2022), which would cause a proportional increase in oxidant concentrations. At this point we do not have enough information to understand how seasonal variations in temperature might affect oxidant concentrations, so we have not attempted to factor this into our analysis.

3.4 Apparent quantum yields for photooxidants

3.4.1 Hydroxyl radical

To investigate how sample type affects the efficiency of photooxidant formation, we determined apparent quantum yields of photooxidant formation (Φ_{Ox}), i.e., the fraction of absorbed photons that result in formation of a particular photooxidant:

$$\Phi_{Ox} = \frac{P_{Ox}}{R_{abs}}, \quad (6)$$

where P_{Ox} is the oxidant production rate, and R_{abs} is the rate of sunlight absorption by the sample between 300 and 450 nm (Kaur et al., 2019). The apparent quantum yield integrates photochemistry for all the chromophores in a natural sample and quantifies the overall efficiency of oxidant production. We calculate the production rate of $^{\bullet}$OH, P_{OH}, by assuming that it is equal to the $^{\bullet}$OH consumption rate since the hydroxyl radical (and the other photooxidants) is in a steady state. Thus, P_{OH} is equal to the product of [$^{\bullet}$OH] and the first-order rate constant of $^{\bullet}$OH loss by natural sinks (k'_{OH}). To estimate k'_{OH}, we assume that organic matter is the dominant sink for $^{\bullet}$OH (Kaur et al., 2019) and that k'_{OH} is the product of DOC concentration and the second-order rate constant of DOC with $^{\bullet}$OH (k_{DOC+OH}). For k_{DOC+OH}, we used the average value measured in Davis winter and summer wildfire particle extracts (Ma et al., 2023a), which is 2.7 ($\pm$ 0.4) $\times$ 10^8 L (mol C)$^{-1}$ s^{-1}. This value is slightly lower than that determined by Arakaki et al. (2013) for a broad range of atmospheric waters (3.8 ($\pm$ 1.9) $\times$ 10^8 L (mol C)$^{-1}$ s^{-1}) and the one from Leresche et al. (2021) for Colorado PM extracts (4.9 ($\pm$ 2.3) $\times$ 10^8 L (mol C)$^{-1}$ s^{-1}), but none of these are statistically different. In our samples, the resulting calculated k'_{OH} is in the range of (0.11–4.3) $\times$ 10^6 s^{-1} (Table S3), yielding P_{OH} in the range of (0.04–14) $\times$ 10^{-9} M s^{-1}, similar to past measured and modeled values for fog/cloud waters and particle extracts (Arakaki et al., 2013; Leresche et al., 2021; Tilgner and Herrmann, 2018).

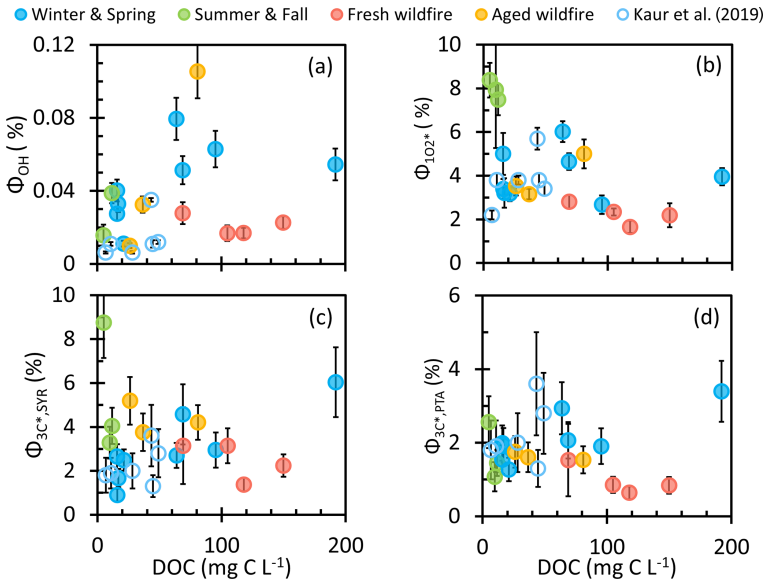

Figure 7. Apparent quantum yields of **(a)** the hydroxyl radical, **(b)** singlet molecular oxygen, and oxidizing triplets determined by **(c)** syringol and **(d)** (phenylthio)acetic acid as a function of dissolved organic matter for each sample type (solid circles). Previous measurements made in Davis winter particle extracts are in open circles (Kaur et al., 2019).

Our calculated apparent quantum yields of $^{\bullet}$OH are shown in Fig. 7a, along with past Davis winter PME samples from Kaur et al. (2019). Φ_{OH} ranges from 0.01 % to 0.10 % in our samples, which are generally higher than values from Kaur et al. (2019) and from PM_{10} and lab SOA water extracts (Manfrin et al., 2019). As expected, Φ_{OH} appears independent of DOC. Average $^{\bullet}$OH quantum yields for Win-Spr, Sum-Fall, FBB, and ABB are 0.044 (± 0.022) %, 0.028 (± 0.010) %, 0.021 (± 0.005) %, and 0.049 (± 0.050) %, respectively. These averages are not statistically different ($p > 0.05$).

3.4.2 Singlet molecular oxygen

To calculate the apparent quantum yields of $^1O_2^*$ ($\Phi_{^1O_2^*}$), we assume that H_2O is the dominant sink for $^1O_2^*$ in our PM extracts. This is a reasonable assumption since the first-order rate constants for $^1O_2^*$ loss via DOC are (0.04–2) × 10^3 s^{-1} in our samples (based on an estimated $^1O_2^*$ + DOC rate constant of 1 × 10^5 L (mol C)$^{-1}$ s^{-1}; Ma et al., 2023a), while the rate constant for $^1O_2^*$ loss by water is 2.2 × 10^5 s^{-1} (Bilski et al., 1997). Therefore, we calculated the production rate of $^1O_2^*$ ($P_{^1O_2^*}$) by multiplying the rate of $^1O_2^*$ loss by water (k'_{H_2O}) by [$^1O_2^*$]. As shown in Fig. 7b, $\Phi_{^1O_2^*}$ ranges from 1.7 % to 8.4 %, comparable to values from Kaur et al. (2019), which are shown as open circles in the figure, as well as from SOA and ambient particle extracts in other studies (0.1 %–4.5 %) (Bogler et al., 2022; Leresche et al., 2021; Manfrin et al., 2019). But our $\Phi_{^1O_2^*}$ values are significantly lower than those in dissolved soot extracts (33 %) (Li et al., 2019) under 377 nm irradiation; we do not expect significant black carbon in our extracts since they were filtered. Sum-Fall has the highest average $\Phi_{^1O_2^*}$, 7.9 (± 0.4) %, which is significantly different from the others, while Win-Spr and ABB have similar average values, 4.0 (± 1.1) and 3.9 (± 1.0), respectively, and FBB shows the lowest average $\Phi_{^1O_2^*}$ of 2.2 (± 0.5) %. The higher quantum yield for aged biomass burning PM compared to fresh BB PM is broadly consistent with the enhancement in $\Phi_{^1O_2^*}$ resulting from ozonation of surface water DOM (Leresche et al., 2019). The difference among sample types is more pronounced when $\Phi_{^1O_2^*}$ is plotted as a function of MAC. As shown in Figs. S21b and S22b, $\Phi_{^1O_2^*}$ decreases with absorbance at 300 or 365 nm, indicating that less light-absorbing brown carbon (e.g., Sum-Fall) more efficiently produces $^1O_2^*$ compared to high-MAC samples (e.g., FBB). In surface waters, $\Phi_{^1O_2^*}$ is positively correlated with E_2/E_3; i.e., the $^1O_2^*$ quantum yield increases for DOM with lower-average-molecular-weight molecules (Berg et al., 2019; Ossola et al., 2021). We find a similar linear relationship in our samples, with an R^2 of 0.54 (Fig. S23). The fresh BB extract has low E_2/E_3 (and low $\Phi_{^1O_2^*}$), suggesting that it contains more high-molecular-weight compounds that absorb significant amounts of light but inefficiently produce $^1O_2^*$. It has been suggested that DOM with a high lignin content (as expected for BB PM) can have a high degree of charge transfer interactions, which results in low $\Phi_{^1O_2^*}$ (Ossola et al., 2021). Despite the relatively inefficient production of singlet oxygen by the fresh BB extracts, these samples have some of the highest $^1O_2^*$ concentrations (Fig. 4), a result of their very strong light absorption (Fig. 2). During the review of this work, we were alerted to a more recent rate constant of $^1O_2^*$ loss by water of 2.76 × 10^5 s^{-1} (Ap-

piani et al., 2017), which is 26 % higher than the value we employed ($2.2 \times 10^5\ s^{-1}$; Bilski et al., 1997). We decided to continue to use our original value so that our results here are consistent with our recent work in PM extracts (Jiang et al., 2023; Kaur et al., 2019; Ma et al., 2023a). Applying the new rate constant would increase our $^1O_2^*$ production rates and quantum yields by 26 % and decrease our $^1O_2^*$ steady-state concentrations by 3 %.

3.4.3 Oxidizing triplet excited states

To calculate the production rate of $^3C^*$, we first need to estimate the $^3C^*$ sink, which is dominated by dissolved oxygen at low DOC but by organic matter as DOC increases. We estimated average second-order rate constants for DOC reacting with and physically quenching $^3C^*$ ($k_{rxn+Q,^3C^*}$) in our samples by fitting [$^3C^*$] as a function of DOC with a hyperbolic regression (Fig. S24). Values of $k_{rxn+Q,^3C^*}$, calculated from one of the regression fitting parameters (Kaur et al., 2019), are 7.2 ($\pm$ 2.2) $\times 10^7$ L (mol C)$^{-1}$ s^{-1} for $^3C^*$ determined by SYR and 7.4 ($\pm$ 2.5) $\times 10^7$ L (mol C)$^{-1}$ s^{-1} for $^3C^*$ by PTA. Since the production rate of $^3C^*$ (P_{3C^*}) is equal to its loss rate, we calculate the former with

$$P_{3C^*} = \left(k_{rxn+Q,^3C^*}[DOC] + k_{3C^*+O_2}[O_2]\right) \times [^3C^*], \quad (7)$$

where $k_{3C^*+O_2}$ is the second-order rate constant of dissolved oxygen reacting with $^3C^*$ ($2.8 \times 10^9\ M^{-1}\ s^{-1}$) (Kaur et al., 2019), and [O_2] is the dissolved oxygen concentration, 280 µM at 20 °C for an air-saturated solution (U.S. Geological Survey, 2020). The apparent quantum yield of $^3C^*$ is then calculated using P_{3C^*} divided by the rate of light absorption (Eq. 7).

Figure 7c and d show quantum yields of $^3C^*$ determined by SYR ($\Phi_{3C^*,SYR}$) and PTA ($\Phi_{3C^*,PTA}$). $\Phi_{3C^*,SYR}$ has a range of 0.9 %–8.8 % and an average value of 3.5 ($\pm$ 1.8) %. Our values are similar to Φ_{3C^*} in past Davis winter PM extracts (as shown by the open circles in the figures), as well as fog waters and surface waters, which are in the range 0.3 %–14 % (Kaur and Anastasio, 2018; McCabe and Arnold, 2018). We do not observe significant differences in $\Phi_{3C^*,SYR}$ among sample types (Fig. S25), consistent with the similarities among sample types in the relationship of [$^3C^*$]$_{SYR}$ versus DOC (Fig. 4). $\Phi_{3C^*,PTA}$ has a range of 0.6 %–3.4 %, with an average value of 1.7 ($\pm$ 0.7) %, half of the average $\Phi_{3C^*,SYR}$. Win-Spr has the highest average $\Phi_{3C^*,PTA}$, 2.1 ($\pm$ 0.7) %, while FBB has the lowest, 0.96 ($\pm$ 0.39) %, but they are not statistically different. Though $^3C^*$ is the precursor of $^1O_2^*$, Φ_{3C^*} does not correlate well with MAC, unlike $\Phi_{^1O_2^*}$ (Figs. S21 and S22), probably because we are measuring only the oxidizing portion of the triplet pool. In surface waters, Φ_{3C^*} often increases with E_2/E_3, similar to $\Phi_{^1O_2^*}$ (Berg et al., 2019; Maizel and Remucal, 2017; McCabe and Arnold, 2017), but we do not see this triplet behavior in our samples (Fig. S26) even though we do for $^1O_2^*$ (Fig. S23).

We next use our quantum yields to estimate the fraction of the total triplet pool that can oxidize SYR or PTA. Since almost all triplets can transfer energy to dissolved oxygen to make $^1O_2^*$, we estimate the quantum yield of total $^3C^*$ as $\Phi_{^1O_2^*}/f_\Delta$, where f_Δ is the fraction of $^3C^*$ interactions with dissolved oxygen that form $^1O_2^*$. Therefore, the fraction of triplets that are oxidizing can be calculated as $\Phi_{3C^*}/(\Phi_{^1O_2^*}/f_\Delta)$, with values shown in Fig. S27. We use an estimated f_Δ of 0.53 (Kaur and Anastasio, 2018; McNeill and Canonica, 2016), which is somewhat higher than the value of 0.34 for Suwannee River fulvic acid at 346 nm measured by Schmitt et al. (2017). For $^3C^*$ determined by SYR, the fraction of triplets that are oxidizing ranges from 0.14 to 0.81, with an average of 0.47 ($\pm$ 0.20) and no statistical difference among the four sample types. This average value is similar to those determined in fog waters (0.55 $\pm$ 0.44) as well as in previous Davis winter particle extracts (0.31 $\pm$ 0.11) (Kaur and Anastasio, 2018; Kaur et al., 2019), indicating that roughly half of the triplets in Davis PM and fog samples are oxidizing. For strongly oxidizing triplets determined by PTA, the fraction ranges from 0.07 to 0.45, with an average of 0.24 ($\pm$ 0.09); this is half the SYR value, suggesting that approximately half of oxidizing $^3C^*$ possesses a high reduction potential, consistent with the results of Fig. 6. For $^3C^*$ determined by PTA, Sum-Fall has a statistically lower average value, 0.11 ($\pm$ 0.05), compared to Win-Spr (0.29 $\pm$ 0.09), FBB (0.22 $\pm$ 0.04), and ABB (0.23 $\pm$ 0.06). This is reasonable because Sum-Fall samples were not significantly influenced by biomass burning, leading to a lower aromatic content and more weakly oxidizing triplets (McNeill and Canonica, 2016).

3.4.4 Quantum yields in aerosol liquid water

We calculated the quantum yields above for the relatively dilute conditions of our particle extracts, but these results are not necessarily applicable to the more concentrated conditions of aerosol liquid water. This is because the formation rate of each oxidant (P_{Ox}) is not necessarily proportional to the concentration factor of the sample, while the light absorption should be proportional; based on Eq. (7), if these factors do not vary in the same way as samples get more concentrated, the quantum yield will vary with concentration. As described by Ma et al. (2023a), as we move from dilute extracts to concentrated particle water P_{3C^*} appears to increase linearly with concentration factor, $P_{^1O_2^*}$ does not, and P_{OH} only does sometimes. This suggests that triplet quantum yields in ALW will be similar to those determined in PME but that yields for singlet oxygen and the hydroxyl radical can be lower in ALW compared to in PME. In each case, care needs to be taken when applying the extract quantum yields from above to more concentrated conditions.

3.5 Extrapolation of photooxidant concentrations to aerosol liquid water (ALW) conditions

Particle mass / water mass ratios in our PM extracts range from 10^{-5} to 10^{-3} μg PM/μg H_2O (Table S1), which are typical for dilute hydrometeors like cloud and fog drops (Hess et al., 1998; Nguyen et al., 2016; Parworth et al., 2017). While the results in dilute extracts are interesting and applicable to cloud and fog chemistry, our goal is to understand photooxidant concentrations for each sample type in aerosol liquid water, which is orders of magnitude more concentrated (typically near 1 μg PM/μg H_2O). Due to the very limited water content of particles, we cannot study this condition directly using our current probe techniques. Instead, our approach has been to quantify photooxidant kinetics (i.e., formation rates and loss rate constants) in a single PM sample as a function of particle dilution and then extrapolate to ALW conditions (Kaur et al., 2019; Ma et al., 2023a). The photooxidant concentration is estimated with

$$[\mathrm{Ox}] = \frac{P_{\mathrm{Ox}}}{k'_{\mathrm{Ox}}}, \quad (8)$$

where P_{Ox} is the oxidant production rate, and k'_{Ox} is the loss rate constant. We do this with our current samples by applying parameters obtained from our recent dilution study of a winter (WIN) and a summer (SUM) $PM_{2.5}$ sample (Ma et al., 2023a). Details about the extrapolations and accompanying parameters are provided in Sect. S4 and Table S10. Moreover, we take the influence of actinic flux on sample types into consideration by using the average midday $j_{2\mathrm{NB}}$ value for each sample type to normalize photooxidant concentrations to that sunlight condition.

We calculate [•OH] in ALW using the average P_{OH} and k'_{OH} values that were determined from the Davis winter and summer particle extracts in our previous study (Ma et al., 2023a). We do not consider the effect of sample type because we do not observe significant differences in the relationship of [•OH] versus DOC among our four sample types (Fig. 5a). As shown in Fig. S28, the predicted •OH concentration is relatively constant across drop to particle conditions, with a range of (6–9) × 10^{-15} M. The predicted [•OH] under dilute conditions is higher than our measured values because we include •OH from the gas phase in our calculation (Kaur et al., 2019). As shown in Fig. 8, [•OH] at 1 μg PM/μg H_2O has a range of (8.8–13) × 10^{-15} M, of which the difference among sample types is driven by the seasonal variation in actinic flux. Our •OH concentrations are around 10 times higher than the previous ALW value predicted by Kaur et al. (2019).

We next consider singlet oxygen. As shown in Fig. S30, $[^1O_2^*]$ for each sample type increases with particle mass / water mass ratio under dilute conditions, peaks near 0.01–0.1 μg PM/μg H_2O, and then decreases under more concentrated conditions. At 1 μg PM/μg H_2O, Win-Spr has the highest $[^1O_2^*]$ (8 × 10^{-12} M), followed by Sum-Fall (3 × 10^{-12} M), FBB (2 × 10^{-12} M), and ABB (1 × 10^{-12} M)

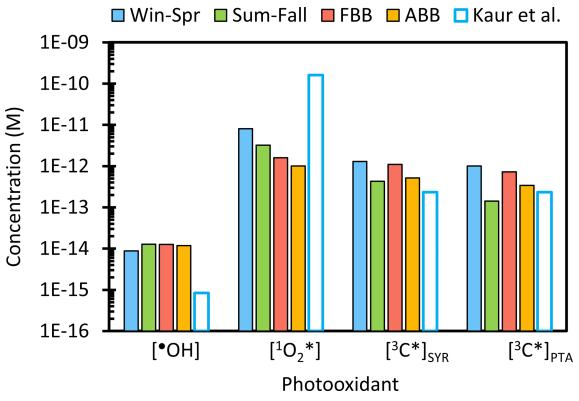

Figure 8. Predicted photooxidant concentrations for each sample type under aerosol liquid water conditions (1 μg PM/μg H_2O), normalized to the average midday actinic flux for each sample type. Previous extrapolations made from Davis winter particle extracts are in open bars, where photooxidant concentrations are normalized to Davis winter solstice sunlight, and $^3C^*$ is the lower-bound estimate (Kaur et al., 2019). Photooxidant concentrations all normalized to Davis winter solstice sunlight are in Fig. S32.

(Fig. 8). Win-Spr is characterized by its high $^1O_2^*$ quantum yield, second-highest light absorption, and low rate of DOC quenching for both $^3C^*$ and $^1O_2^*$. In contrast, FBB and ABB have more brown carbon (and therefore greater sources of $^1O_2^*$) but high DOC, which leads to greater sinks for triplets and singlet oxygen. Moreover, DOC in FBB and ABB quenches $^3C^*$ more efficiently than that in Win-Spr (i.e., the BB samples have higher values of $k_{\mathrm{rxn+Q},^3C^*}$). Therefore, their $[^1O_2^*]$ in ALW is similar to, or even lower than, $[^1O_2^*]$ measured in FBB and ABB extracts, while the ALW singlet oxygen concentrations for Win-Spr and Sum-Fall are nearly 20 times higher than their corresponding averages in extracts. Our estimated $[^1O_2^*]$ in ALW is 20–200 times lower than the value derived by Kaur et al. (2019), 1.6 × 10^{-10} M, for Davis winter particle water. This is primarily because we account for DOC suppressing $^3C^*$ concentrations and therefore lowering the rate of $^1O_2^*$ production at high DOC values; this was not done in the previous work.

Our final ALW predictions are for oxidizing triplets. $[^3C^*]$ for all sample types increases with particle mass concentration under dilute conditions but then reaches a plateau as solutions become more concentrated, and DOC becomes the dominant sink for triplets (Fig. S31). As shown in Fig. 8, $[^3C^*]_{\mathrm{SYR}}$ and $[^3C^*]_{\mathrm{PTA}}$ at 1 μg PM/μg H_2O have a range of (0.4–13) × 10^{-12} M and (0.1–10) × 10^{-12} M, respectively, with Win-Spr and Sum-Fall having the maximum and minimum values, respectively. Sum-Fall samples might contain a lower fraction of carbonyl or ketone compounds compared to other sample types, leading to lower production of oxidizing $^3C^*$ (McNeill and Canonica, 2016). Compared to our average measured $^3C^*$ concentration in the PM extracts, $[^3C^*]$ in ALW for Win-Spr and Sum-Fall samples increases by a fac-

tor of approximately 20, while ALW concentrations for FBB and ABB are only around 2 times higher than their extract values. Our predicted $[^3C^*]_{SYR}$ is 2–5 times higher than the lower-bound (best-fit) estimate of Kaur et al. (2019) (Fig. 8).

3.6 Impact of photooxidants on organic fates in an aerosol

To understand how photooxidants affect the fate of organic compounds in ALW, we revisit the Kaur et al. (2019) estimates for the lifetimes and fates of five model organic compounds: (1) syringol, (2) methyl jasmonate, (3) tyrosine, (4) 1,2,4-butanetriol, and (5) 3-hydroxy-2,5-bis(hydroxymethyl)furan. To estimate the fate of each compound, we assume equilibrium gas–aqueous partitioning in an aerosol with an ALW of $20\,\mu g\,m^{-3}$ and consider reactions with two gas-phase oxidants ($^\bullet$OH, O_3) and four aqueous-phase oxidants ($^\bullet$OH, O_3, $^3C^*$, $^1O_2^*$). In our calculations, we employ rate constants and Henry's law constants (K_H) from Kaur et al. (2019) and use our predicted ALW photooxidant concentrations in Win-Spr ($[^\bullet OH] = 7 \times 10^{-15}$ M, $[^1O_2^*] = 7 \times 10^{-12}$ M, $[^3C^*]_{SYR} = 1 \times 10^{-12}$ M, normalized to Davis winter solstice sunlight). More details about the calculations are in Kaur et al. (2019). We assume that Henry's law constants apply to our hypothetical concentrated particle water condition, but this might not be the case since ALW is far from a dilute solution; however, accounting for potential salting-out effects and organic-activity coefficients is beyond our simple scope here. As shown in Fig. 9, syringol (1) and methyl jasmonate (2), which have low K_H values, partition negligibly to the aqueous phase, and so gas-phase reactions dominate their fates, with overall lifetimes of 2–3 h; these results are the same for both the aqueous oxidant concentrations of Kaur et al. (2019) and those determined in this work (i.e., Fig. 8). For tyrosine (3), 1,2,4-butanetriol (4), and 3-hydroxy-2,5-bis(hydroxymethyl)furan (5), which have high K_H values, 30 %–100 % of the species are present in the aqueous phase of the aerosol. With photooxidant concentrations predicted by Kaur et al. (2019), organic lifetimes range from 0.04 to 20 h, and $^1O_2^*$ is the major sink. However, in this work we predict higher $^\bullet$OH and $^3C^*$ concentrations but significantly lower $^1O_2^*$ in ALW (Fig. 8). The lower $^1O_2^*$ leads to lifetimes of tyrosine (3) and the furan (5) increasing by factors of 6 and 17, respectively. $^3C^*$ becomes the dominant oxidant for the phenolic amino acid, tyrosine (3), but singlet oxygen is still the dominant sink for the substituted furan, compound (5). With the new oxidant concentrations, the lifetime of the aliphatic alcohol, 1,2,4-butanetriol (4), decreases by a factor of almost 3 due to the enhanced $^\bullet$OH concentration, and singlet oxygen is much less important. Overall, results with the new oxidant concentrations show some significant shifts in the lifetimes of the three highly soluble organics as well as in the contributions of individual oxidants. But our new results still indicate that $^3C^*$ and $^1O_2^*$ dominate the particle processing for highly soluble organic compounds with which they react quickly, while $^\bullet$OH dominates for aqueous organics that react slowly with the other two oxidants. Based on our Win-Spr oxidant concentrations (Fig. 8), for an organic compound that has an $^\bullet$OH rate constant of $1 \times 10^{10}\,M^{-1}\,s^{-1}$, singlet oxygen will be the dominant oxidant if its rate constant with the organic is larger than roughly $1 \times 10^{7}\,M^{-1}\,s^{-1}$, while oxidizing triplets will dominate if their rate constant is larger than approximately $1 \times 10^{8}\,M^{-1}\,s^{-1}$.

4 Conclusions, implications, and uncertainties

In this work, we measured concentrations of three photooxidants – the hydroxyl radical, singlet molecular oxygen, and oxidizing triplet excited states of brown carbon – in particle extracts. Our extracts have particle mass/liquid water mass ratios in the range of $(0.7–9.1) \times 10^{-4}\,\mu g\,PM/\mu g\,H_2O$, which are close to fog/cloud water conditions but much more dilute than aerosol liquid water. We categorized samples into four types based on sampling dates and chemical characterization: winter and spring (Win-Spr), summer and fall (Sum-Fall) without wildfire influence, fresh biomass burning (FBB), and aged biomass burning (ABB). FBB contains the highest amounts of BrC, leading to the highest average mass absorption coefficients normalized by dissolved organic carbon, e.g., 3.3 ($\pm$ 0.4) m^2 per gram C at 300 nm. Win-Spr and ABB have similar MACs at this wavelength (1.9 ($\pm$ 0.4) m^2 per gram C) and 1.5 ($\pm$ 0.3) m^2 per gram C, respectively), while Sum-Fall has the lowest MAC_{DOC} (0.65 ($\pm$ 0.19) m^2 per gram C).

Photooxidant concentrations in the particle extracts are in the range of $(0.2–4.7) \times 10^{-15}$ M for $^\bullet$OH, $(0.07–4.5) \times 10^{-12}$ M for $^1O_2^*$, and $(0.03–7.9) \times 10^{-13}$ M for $^3C^*$, respectively. All oxidant concentrations generally increase with the concentration of dissolved organic carbon (DOC), which ranged from 5 to 192 $mg\,C\,L^{-1}$. $^1O_2^*$ concentrations exhibit good linearity with DOC, with all sample types falling roughly on the same line. Fresh BB extracts have the highest $[^1O_2^*]$ but the lowest average quantum yield ($\Phi_{^1O_2^*}$), while Sum-Fall samples are the opposite. $\Phi_{^1O_2^*}$ is negatively correlated with MAC_{DOC}, indicating that less light-absorbing samples form $^1O_2^*$ more efficiently. Triplet concentrations determined by both probes linearly increase with DOC, and this relationship for $[^3C^*]_{SYR}$ is independent of sample type. We find that approximately half of the total triplets are oxidizing based on SYR loss, while roughly half of the oxidizing triplets are strongly oxidizing based on PTA loss. FBB has the lowest average $\Phi_{^3C^*}$, while atmospheric aging appears to enhance $\Phi_{^3C^*}$, as well as $\Phi_{^1O_2^*}$, based on the higher quantum yields for ABB samples.

Based on our results in dilute PM extracts (as well as past work), light absorption by brown carbon produces significant amounts of photooxidants in particles. To estimate the corresponding photooxidant concentrations, we extrapolate measured photooxidant kinetics in our particle extracts to an aerosol liquid water condition ($1\,\mu g\,PM/\mu g\,H_2O$). Estimated molar concentrations of $^1O_2^*$ in ALW are on the order of 10^{-12}–10^{-11}, while values are 10^{-13}–10^{-12} for $^3C^*$ and 10^{-14} for $^\bullet OH$ with a ratio of $^1O_2^*$: $^3C^*$: $^\bullet OH$ of (900–90) : (150–10) : 1. For comparison, the corresponding ratio in our particle extracts is (40–5) : (10–1) : 1. For Win-Spr and Sum-Fall samples, singlet oxygen and oxidizing triplet concentrations increase significantly in ALW compared to in dilute extracts, while the changes in FBB and ABB are minor, likely due to the high DOC in the extracts, which causes strong quenching of $^1O_2^*$ and $^3C^*$. Compared to the predicted photooxidant concentrations in Davis winter particle water by Kaur et al. (2019), our Win-Spr predictions for [$^\bullet OH$] and [$^3C^*$] are nearly 10 and 5 times higher, respectively, but our ALW value for [$^1O_2^*$] is 20 times lower. Based on our estimated ALW concentrations, lifetimes of organic compounds with high Henry's law constants in ALW can be significantly shortened compared to foggy conditions (Kaur et al., 2019), due to enhanced $^3C^*$ and $^1O_2^*$ concentrations in particle water.

While oxidant concentrations are required to calculate the lifetimes of individual organic species in ALW, the formation rate of a photooxidant provides insight into the overall significance of that oxidant as a sink for organics. Since organic compounds appear to be the major sink for all three photooxidants in ALW, the formation rate of an oxidant is approximately equal to the rate of DOM processing by that oxidant, although organics can also physically quench a triplet without transforming the organic (Grebel et al., 2011; Ma et al., 2021; Smith et al., 2014). Based on our extrapolations, the ratio of formation rates in ALW for $^1O_2^*$, $^3C^*$, and $^\bullet OH$ (including mass transfer from the gas phase) is 1 : 100 : 4, taking Win-Spr as an example. Since the triplet formation rate is much higher than those of $^\bullet OH$ or $^1O_2^*$, our results indicate that $^3C^*$ might be more important for the overall oxidation of organic compounds compared to the other two oxidants. However, the picture for any specific organic compound depends on its rate constants with each oxidant. For example, $^\bullet OH$ will be relatively more important for organics that are less reactive with $^3C^*$ and $^1O_2^*$.

There are important uncertainties in the ALW oxidant concentrations reported in our work. Foremost, predicting photooxidant concentrations from dilute extracts under ALW conditions is highly uncertain as it requires extrapolating over a concentration difference of approximately a factor of 1000. While our current extracts have more DOC than those in our past work (Kaur et al., 2019), allowing us to get closer to ALW chemistry, we are still orders of magnitude too dilute. Despite this improvement, additional approaches – such as chamber and flow tube studies – are needed to measure photooxidants and their chemical impacts under conditions more similar to ambient aerosols. The oxidizing triplet concentrations are less certain than those of the other two oxidants, both because we use an individual triplet ($^3DMB^*$) to model the wide range of natural triplet reactivities and also because of uncertainties in correcting the inhibition of syringol oxidation by particle components. Another uncertainty with our current (and past) results is that we are missing the water-insoluble chromophores from particles. Consistent with past results from other groups, we find significant amounts of highly light-absorbing organic-insoluble brown carbon in our particle samples, suggesting that by using aqueous extracts we are underestimating the concentrations and significance of photooxidants in ambient particles. This issue should be addressed in future photochemistry studies.

Data availability. All data are available upon request.

Supplement. The supplement related to this article is available online at: https://doi.org/10.5194/acp-24-1-2024-supplement.

Author contributions. CA and LM developed the research goals and designed the experiments. KJB lent and set up the sampler, while LM and CG collected samples. LM, RW, and LH performed the photochemistry experiments, while WJ and CN analyzed OC and ions, respectively. LM analyzed the data and prepared the manuscript with contributions from all co-authors. CA reviewed, wrote portions of, and edited the manuscript. CA and QZ provided supervision and oversight during the experiments and writing.

Competing interests. The contact author has declared that none of the authors has any competing interests.

Disclaimer. Publisher's note: Copernicus Publications remains neutral with regard to jurisdictional claims made in the text, published maps, institutional affiliations, or any other geographical representation in this paper. While Copernicus Publications makes every effort to include appropriate place names, the final responsibility lies with the authors.

Acknowledgements. We gratefully acknowledge the following agencies for their publicly available data: the California Air Resources Board for $PM_{2.5}$ data; the Earth Observing System Data and Information System (EOSDIS) for wildfire and smoke images, part of NASA's Land, Atmosphere Near real-time Capability for EOS (LANCE) system (https://earthdata.nasa.gov/lance, last access: 15 July 2022); and the NOAA Air Resources Laboratory (ARL), which provided the HYSPLIT model and READY website (https://www.ready.noaa.gov, last access: 15 July 2022).

Financial support. This research has been supported by the National Science Foundation (grant nos. AGS-1649212 and AGS-2220307); the California Agricultural Experiment Station (projects CA-D-LAW-6403-RR and CA-D-ETX-2102-H); and the University of California, Davis (Donald G. Crosby Graduate Fellowships in Environmental Chemistry and Jastro-Shields Research Awards).

Review statement. This paper was edited by Ryan Sullivan and reviewed by three anonymous referees.

References

Alfarra, M. R., Prevot, A. S. H., Szidat, S., Sandradewi, J., Weimer, S., Lanz, V. A., Schreiber, D., Mohr, M., and Baltensperger, U.: Identification of the Mass Spectral Signature of Organic Aerosols from Wood Burning Emissions, Environ. Sci. Technol., 41, 5770–5777, https://doi.org/10.1021/es062289b, 2007.

Anastasio, C. and McGregor, K. G.: Chemistry of fog waters in California's Central Valley: 1. In situ photoformation of hydroxyl radical and singlet molecular oxygen, Atmos. Environ., 35, 1079–1089, https://doi.org/10.1016/S1352-2310(00)00281-8, 2001.

Appiani, E., Ossola, R., Latch, D. E., Erickson, P. R., and McNeill, K.: Aqueous singlet oxygen reaction kinetics of furfuryl alcohol: effect of temperature, pH, and salt content, Environ. Sci.-Proc. Imp., 19, 507–516, https://doi.org/10.1039/C6EM00646A, 2017.

Arakaki, T., Anastasio, C., Kuroki, Y., Nakajima, H., Okada, K., Kotani, Y., Handa, D., Azechi, S., Kimura, T., Tsuhako, A., and Miyagi, Y.: A general scavenging rate constant for reaction of hydroxyl radical with organic carbon in atmospheric waters, Environ. Sci. Technol., 47, 8196–8203, https://doi.org/10.1021/es401927b, 2013.

Ashton, L., Buxton, G. V., and Stuart, C. R.: Temperature dependence of the rate of reaction of OH with some aromatic compounds in aqueous solution. Evidence for the formation of a π-complex intermediate?, J. Chem. Soc. Faraday T., 91, 1631–1633, https://doi.org/10.1039/FT9959101631, 1995.

Baba, Y., Yatagai, T., Harada, T., and Kawase, Y.: Hydroxyl radical generation in the photo-Fenton process: Effects of carboxylic acids on iron redox cycling, Chem. Eng. J., 277, 229–241, https://doi.org/10.1016/j.cej.2015.04.103, 2015.

Badali, K. M., Zhou, S., Aljawhary, D., Antiñolo, M., Chen, W. J., Lok, A., Mungall, E., Wong, J. P. S., Zhao, R., and Abbatt, J. P. D.: Formation of hydroxyl radicals from photolysis of secondary organic aerosol material, Atmos. Chem. Phys., 15, 7831–7840, https://doi.org/10.5194/acp-15-7831-2015, 2015.

Berg, S. M., Whiting, Q. T., Herrli, J. A., Winkels, R., Wammer, K. H., and Remucal, C. K.: The role of dissolved organic matter composition in determining photochemical reactivity at the molecular level, Environ. Sci. Technol., 53, 11725–11734, https://doi.org/10.1021/acs.est.9b03007, 2019.

Bilski, P., Holt, R. N., and Chignell, C. F.: Properties of singlet molecular oxygen in binary solvent mixtures of different polarity and proticity, J. Photoch. Photobio. A, 109, 243–249, https://doi.org/10.1016/S1010-6030(97)00147-0, 1997.

Bogler, S., Daellenbach, K. R., Bell, D. M., Prévôt, A. S. H., El Haddad, I., and Borduas-Dedekind, N.: Singlet oxygen seasonality in aqueous PM_{10} is driven by biomass burning and anthropogenic secondary organic aerosol, Environ. Sci. Technol., 56, 15389–15397, https://doi.org/10.1021/acs.est.2c04554, 2022.

Buckley, S., Leresche, F., Hanson, B., and Rosario-Ortiz, F. L.: Decoupling optical response and photochemical formation of singlet oxygen in size isolated fractions of ozonated dissolved organic matter, Environ. Sci. Technol., 57, 5603–5610, https://doi.org/10.1021/acs.est.2c08155, 2023.

Budisulistiorini, S. H., Riva, M., Williams, M., Chen, J., Itoh, M., Surratt, J. D., and Kuwata, M.: Light-Absorbing Brown Carbon Aerosol Constituents from Combustion of Indonesian Peat and Biomass, Environ. Sci. Technol., 51, 4415–4423, https://doi.org/10.1021/acs.est.7b00397, 2017.

California Air Resources Board AQMIS Database: Institute: California Environmental Protection Agency, https://www.arb.ca.gov/aqmis2/aqmis2.php, last access: 12 July 2022.

Canonica, S. and Laubscher, H.-U.: Inhibitory effect of dissolved organic matter on triplet-induced oxidation of aquatic contaminants, Photoch. Photobio. Sci., 7, 547, https://doi.org/10.1039/b719982a, 2008.

Chen, K., Raeofy, N., Lum, M., Mayorga, R., Woods, M., Bahreini, R., Zhang, H., and Lin, Y.-H.: Solvent effects on chemical composition and optical properties of extracted secondary brown carbon constituents, Aerosol Sci. Tech., 56, 917–930, https://doi.org/10.1080/02786826.2022.2100734, 2022.

Chen, Y., Hozalski, R. M., Olmanson, L. G., Page, B. P., Finlay, J. C., Brezonik, P. L., and Arnold, W. A.: Prediction of photochemically produced reactive intermediates in surface waters via satellite remote sensing, Environ. Sci. Technol., 54, 6671–6681, https://doi.org/10.1021/acs.est.0c00344, 2020.

Claeys, M., Vermeylen, R., Yasmeen, F., Gómez-González, Y., Chi, X., Maenhaut, W., Mészáros, T., and Salma, I.: Chemical characterisation of humic-like substances from urban, rural and tropical biomass burning environments using liquid chromatography with UV/vis photodiode array detection and electrospray ionisation mass spectrometry, Environ. Chem., 9, 273, https://doi.org/10.1071/EN11163, 2012.

Corral Arroyo, P., David, G., Alpert, P. A., Parmentier, E. A., Ammann, M., and Signorell, R.: Amplification of light within aerosol particles accelerates in-particle photochemistry, Science, 376, 293–296, https://doi.org/10.1126/science.abm7915, 2022.

Dorfman, L. M. and Adams, G. E.: Reactivity of the hydroxyl radical in aqueous solutions, National Bureau of Standards, Gaithersburg, MD, https://doi.org/https://doi.org/10.6028/NBS.NSRDS.46, 1973.

Du, Z., He, K., Cheng, Y., Duan, F., Ma, Y., Liu, J., Zhang, X., Zheng, M., and Weber, R.: A yearlong study of water-soluble organic carbon in Beijing II: Light absorption properties, Atmos. Environ., 89, 235–241, https://doi.org/10.1016/j.atmosenv.2014.02.022, 2014.

Ervens, B.: Progress and problems in modeling chemical processing in cloud droplets and wet aerosol particles, in: Multiphase environmental chemistry in the atmosphere, vol. 1299, edited by: Hunt, S. W., Laskin, A., and Nizkorodov, S. A., American Chemical Society, Washington, DC, pp. 327–345, 2018.

Ervens, B., Turpin, B. J., and Weber, R. J.: Secondary organic aerosol formation in cloud droplets and aqueous particles (aqSOA): a review of laboratory, field and model studies, Atmos.

Chem. Phys., 11, 11069–11102, https://doi.org/10.5194/acp-11-11069-2011, 2011.

Ervens, B., Sorooshian, A., Lim, Y. B., and Turpin, B. J.: Key parameters controlling OH-initiated formation of secondary organic aerosol in the aqueous phase (aqSOA), J. Geophys. Res.-Atmos., 119, 3997–4016, https://doi.org/10.1002/2013JD021021, 2014.

Fan, X., Li, M., Cao, T., Cheng, C., Li, F., Xie, Y., Wei, S., Song, J., and Peng, P.: Optical properties and oxidative potential of water- and alkaline-soluble brown carbon in smoke particles emitted from laboratory simulated biomass burning, Atmos. Environ., 194, 48–57, https://doi.org/10.1016/j.atmosenv.2018.09.025, 2018.

Farley, R., Bernays, N., Jaffe, D. A., Ketcherside, D., Hu, L., Zhou, S., Collier, S., and Zhang, Q.: Persistent Influence of Wildfire Emissions in the Western United States and Characteristics of Aged Biomass Burning Organic Aerosols under Clean Air Conditions, Environ. Sci. Technol., 56, 3645–3657, https://doi.org/10.1021/acs.est.1c07301, 2022.

Faust, B. C. and Allen, J. M.: Aqueous-phase photochemical sources of peroxyl radicals and singlet molecular oxygen in clouds and fog, J. Geophys. Res., 97, 12913, https://doi.org/10.1029/92JD00843, 1992.

Fleming, L. T., Lin, P., Roberts, J. M., Selimovic, V., Yokelson, R., Laskin, J., Laskin, A., and Nizkorodov, S. A.: Molecular composition and photochemical lifetimes of brown carbon chromophores in biomass burning organic aerosol, Atmos. Chem. Phys., 20, 1105–1129, https://doi.org/10.5194/acp-20-1105-2020, 2020.

Galbavy, E. S., Ram, K., and Anastasio, C.: 2-Nitrobenzaldehyde as a chemical actinometer for solution and ice photochemistry, J. Photoch. Photobio. A, 209, 186–192, https://doi.org/10.1016/j.jphotochem.2009.11.013, 2010.

Gilardoni, S., Massoli, P., Paglione, M., Giulianelli, L., Carbone, C., Rinaldi, M., Decesari, S., Sandrini, S., Costabile, F., Gobbi, G. P., Pietrogrande, M. C., Visentin, M., Scotto, F., Fuzzi, S., and Facchini, M. C.: Direct observation of aqueous secondary organic aerosol from biomass-burning emissions, P. Natl. Acad. Sci. USA, 113, 10013–10018, https://doi.org/10.1073/pnas.1602212113, 2016.

Gollnick, K. and Griesbeck, A.: ChemInform Abstract: Singlet Oxygen Photooxygenation of Furans. Isolation and Reactions of [4 + 2]-Cycloaddition Products (Unsaturated sec.-Ozonides), Chemischer Informationsdienst, 16, https://doi.org/10.1002/chin.198540196, 1985.

Gonzalez, D. H., Cala, C. K., Peng, Q., and Paulson, S. E.: HULIS Enhancement of Hydroxyl Radical Formation from Fe(II): Kinetics of Fulvic Acid-Fe(II) Complexes in the Presence of Lung Antioxidants, Environ. Sci. Technol., 51, 7676–7685, https://doi.org/10.1021/acs.est.7b01299, 2017.

González Palacios, L., Corral Arroyo, P., Aregahegn, K. Z., Steimer, S. S., Bartels-Rausch, T., Nozière, B., George, C., Ammann, M., and Volkamer, R.: Heterogeneous photochemistry of imidazole-2-carboxaldehyde: HO_2 radical formation and aerosol growth, Atmos. Chem. Phys., 16, 11823–11836, https://doi.org/10.5194/acp-16-11823-2016, 2016.

Grebel, J. E., Pignatello, J. J., and Mitch, W. A.: Sorbic acid as a quantitative probe for the formation, scavenging and steady-state concentrations of the triplet-excited state of organic compounds, Water Res., 45, 6535–6544, https://doi.org/10.1016/j.watres.2011.09.048, 2011.

Hecobian, A., Zhang, X., Zheng, M., Frank, N., Edgerton, E. S., and Weber, R. J.: Water-Soluble Organic Aerosol material and the light-absorption characteristics of aqueous extracts measured over the Southeastern United States, Atmos. Chem. Phys., 10, 5965–5977, https://doi.org/10.5194/acp-10-5965-2010, 2010.

Hems, R. F. and Abbatt, J. P. D.: Aqueous Phase Photo-oxidation of Brown Carbon Nitrophenols: Reaction Kinetics, Mechanism, and Evolution of Light Absorption, ACS Earth Space Chem., 2, 225–234, https://doi.org/10.1021/acsearthspacechem.7b00123, 2018.

Hems, R. F., Schnitzler, E. G., Liu-Kang, C., Cappa, C. D., and Abbatt, J. P. D.: Aging of atmospheric brown carbon aerosol, ACS Earth Space Chem., 5, 722–748, https://doi.org/10.1021/acsearthspacechem.0c00346, 2021.

Herrmann, H.: Kinetics of aqueous phase reactions relevant for atmospheric chemistry, Chem. Rev., 103, 4691–4716, https://doi.org/10.1021/cr020658q, 2003.

Herrmann, H., Hoffmann, D., Schaefer, T., Bräuer, P., and Tilgner, A.: Tropospheric aqueous-phase free-radical chemistry: radical sources, spectra, reaction kinetics and prediction tools, Chem. Phys. Chem., 11, 3796–3822, https://doi.org/10.1002/cphc.201000533, 2010.

Herrmann, H., Schaefer, T., Tilgner, A., Styler, S. A., Weller, C., Teich, M., and Otto, T.: Tropospheric aqueous-phase chemistry: kinetics, mechanisms, and its coupling to a changing gas phase, Chem. Rev., 115, 4259–4334, https://doi.org/10.1021/cr500447k, 2015.

Hess, M., Koepke, P., and Schult, I.: Optical properties of aerosols and clouds: the software package OPAC, B. Am. Meteorol. Soc., 79, 831–844, https://doi.org/10.1175/1520-0477(1998)079<0831:OPOAAC>2.0.CO;2, 1998.

Hettiyadura, A. P. S., Garcia, V., Li, C., West, C. P., Tomlin, J., He, Q., Rudich, Y., and Laskin, A.: Chemical composition and molecular-specific optical properties of atmospheric brown carbon associated with biomass burning, Environ. Sci. Technol., 55, 2511–2521, https://doi.org/10.1021/acs.est.0c05883, 2021.

Jiang, W., Ma, L., Niedek, C., Anastasio, C., and Zhang, Q.: Chemical and Light-Absorption Properties of Water-Soluble Organic Aerosols in Northern California and Photooxidant Production by Brown Carbon Components, ACS Earth Space Chem., 7, 1107–1119, https://doi.org/10.1021/acsearthspacechem.3c00022, 2023.

Kaur, R. and Anastasio, C.: Light absorption and the photoformation of hydroxyl radical and singlet oxygen in fog waters, Atmos. Environ., 164, 387–397, https://doi.org/10.1016/j.atmosenv.2017.06.006, 2017.

Kaur, R. and Anastasio, C.: First measurements of organic triplet excited states in atmospheric waters, Environ. Sci. Technol., 52, 5218–5226, https://doi.org/10.1021/acs.est.7b06699, 2018.

Kaur, R., Labins, J. R., Helbock, S. S., Jiang, W., Bein, K. J., Zhang, Q., and Anastasio, C.: Photooxidants from brown carbon and other chromophores in illuminated particle extracts, Atmos. Chem. Phys., 19, 6579–6594, https://doi.org/10.5194/acp-19-6579-2019, 2019.

Laskin, A., Laskin, J., and Nizkorodov, S. A.: Chemistry of atmospheric brown carbon, Chem. Rev., 115, 4335–4382, https://doi.org/10.1021/cr5006167, 2015.

Leresche, F., McKay, G., Kurtz, T., von Gunten, U., Canonica, S., and Rosario-Ortiz, F. L.: Effects of ozone on the photochemical and photophysical properties of dissolved organic matter, Environ. Sci. Technol., 53, 5622–5632, https://doi.org/10.1021/acs.est.8b06410, 2019.

Leresche, F., Salazar, J. R., Pfotenhauer, D. J., Hannigan, M. P., Majestic, B. J., and Rosario-Ortiz, F. L.: Photochemical aging of atmospheric particulate matter in the aqueous phase, Environ. Sci. Technol., 55, 13152–13163, https://doi.org/10.1021/acs.est.1c00978, 2021.

Li, M., Bao, F., Zhang, Y., Sheng, H., Chen, C., and Zhao, J.: Photochemical aging of soot in the aqueous phase: release of dissolved black carbon and the formation of 1O2, Environ. Sci. Technol., 53, 12311–12319, https://doi.org/10.1021/acs.est.9b02773, 2019.

Lin, P., Aiona, P. K., Li, Y., Shiraiwa, M., Laskin, J., Nizkorodov, S. A., and Laskin, A.: Molecular characterization of brown carbon in biomass burning aerosol particles, Environ. Sci. Technol., 50, 11815–11824, https://doi.org/10.1021/acs.est.6b03024, 2016.

Lin, P., Bluvshtein, N., Rudich, Y., Nizkorodov, S. A., Laskin, J., and Laskin, A.: Molecular Chemistry of Atmospheric Brown Carbon Inferred from a Nationwide Biomass Burning Event, Environ. Sci. Technol., 51, 11561–11570, https://doi.org/10.1021/acs.est.7b02276, 2017.

Liu, J., Bergin, M., Guo, H., King, L., Kotra, N., Edgerton, E., and Weber, R. J.: Size-resolved measurements of brown carbon in water and methanol extracts and estimates of their contribution to ambient fine-particle light absorption, Atmos. Chem. Phys., 13, 12389–12404, https://doi.org/10.5194/acp-13-12389-2013, 2013.

Ma, L., Guzman, C., Niedek, C., Tran, T., Zhang, Q., and Anastasio, C.: Kinetics and mass yields of aqueous secondary organic aerosol from highly substituted phenols reacting with a triplet excited state, Environ. Sci. Technol., 55, 5772–5781, https://doi.org/10.1021/acs.est.1c00575, 2021.

Ma, L., Worland, R., Jiang, W., Niedek, C., Guzman, C., Bein, K. J., Zhang, Q., and Anastasio, C.: Predicting photooxidant concentrations in aerosol liquid water based on laboratory extracts of ambient particles, Atmos. Chem. Phys., 23, 8805–8821, https://doi.org/10.5194/acp-23-8805-2023, 2023a.

Ma, L., Worland, R., Tran, T., and Anastasio, C.: Evaluation of probes to measure oxidizing organic triplet excited states in aerosol liquid water, Environ. Sci. Technol., 57, 6052–6062, https://doi.org/10.1021/acs.est.2c09672, 2023b.

Maizel, A. C. and Remucal, C. K.: The effect of probe choice and solution conditions on the apparent photoreactivity of dissolved organic matter, Environ. Sci. Process. Impacts, 19, 1040–1050, https://doi.org/10.1039/c7em00235a, 2017.

Manfrin, A., Nizkorodov, S. A., Malecha, K. T., Getzinger, G. J., McNeill, K., and Borduas-Dedekind, N.: Reactive oxygen species production from secondary organic aerosols: the importance of singlet oxygen, Environ. Sci. Technol., 53, 8553–8562, https://doi.org/10.1021/acs.est.9b01609, 2019.

Martin, R. V., Jacob, D. J., Yantosca, R. M., Chin, M., and Ginoux, P.: Global and regional decreases in tropospheric oxidants from photochemical effects of aerosols, J. Geophys. Res., 108, 4097, https://doi.org/10.1029/2002JD002622, 2003.

McCabe, A. J. and Arnold, W. A.: Seasonal and spatial variabilities in the water chemistry of prairie pothole wetlands influence the photoproduction of reactive intermediates, Chemosphere, 155, 640–647, https://doi.org/10.1016/j.chemosphere.2016.04.078, 2016.

McCabe, A. J. and Arnold, W. A.: Reactivity of triplet excited states of dissolved natural organic matter in stormflow from mixed-use watersheds, Environ. Sci. Technol., 51, 9718–9728, https://doi.org/10.1021/acs.est.7b01914, 2017.

McCabe, A. J. and Arnold, W. A.: Multiple linear regression models to predict the formation efficiency of triplet excited states of dissolved organic matter in temperate wetlands, Limnol. Oceanogr., 63, 1992–2014, https://doi.org/10.1002/lno.10820, 2018.

McGregor, K. G. and Anastasio, C.: Chemistry of fog waters in California's Central Valley: 2. Photochemical transformations of amino acids and alkyl amines, Atmos. Environ., 35, 1091–1104, https://doi.org/10.1016/S1352-2310(00)00282-X, 2001.

Mckay, G., Huang, W., Romera-Castillo, C., Crouch, J. E., Rosario-Ortiz, F. L., and Jaffé, R.: Predicting Reactive Intermediate Quantum Yields from Dissolved Organic Matter Photolysis Using Optical Properties and Antioxidant Capacity, Environ. Sci. Technol., 51, 5404–5413, https://doi.org/10.1021/acs.est.6b06372, 2017.

McNeill, K. and Canonica, S.: Triplet state dissolved organic matter in aquatic photochemistry: reaction mechanisms, substrate scope, and photophysical properties, Environ. Sci. Process. Impacts, 18, 1381–1399, https://doi.org/10.1039/c6em00408c, 2016.

McNeill, V. F.: Aqueous organic chemistry in the atmosphere: sources and chemical processing of organic aerosols, Environ. Sci. Technol., 49, 1237–1244, https://doi.org/10.1021/es5043707, 2015.

Monge, M. E., Rosenørn, T., Favez, O., Müller, M., Adler, G., Abo Riziq, A., Rudich, Y., Herrmann, H., George, C., and D'Anna, B.: Alternative pathway for atmospheric particles growth., P. Natl. Acad. Sci. USA, 109, 6840–6844, https://doi.org/10.1073/pnas.1120593109, 2012.

Nguyen, T. K. V., Zhang, Q., Jimenez, J. L., Pike, M., and Carlton, A. G.: Liquid water: ubiquitous contributor to aerosol mass, Environ. Sci. Tech. Let., 3, 257–263, https://doi.org/10.1021/acs.estlett.6b00167, 2016.

Ossola, R., Jönsson, O. M., Moor, K., and McNeill, K.: Singlet oxygen quantum yields in environmental waters, Chem. Rev., 121, 4100–4146, https://doi.org/10.1021/acs.chemrev.0c00781, 2021.

Park, S. S. and Yu, J.: Chemical and light absorption properties of humic-like substances from biomass burning emissions under controlled combustion experiments, Atmos. Environ., 136, 114–122, https://doi.org/10.1016/j.atmosenv.2016.04.022, 2016.

Parworth, C. L., Young, D. E., Kim, H., Zhang, X., Cappa, C. D., Collier, S., and Zhang, Q.: Wintertime water-soluble aerosol composition and particle water content in Fresno, California, J. Geophys. Res.-Atmos., 122, 3155–3170, https://doi.org/10.1002/2016JD026173, 2017.

Paulson, S. E., Gallimore, P. J., Kuang, X. M., Chen, J. R., Kalberer, M., and Gonzalez, D. H.: A light-driven burst of hydroxyl radicals dominates oxidation chemistry in newly activated cloud droplets, Sci. Adv., 5, eaav7689, https://doi.org/10.1126/sciadv.aav7689, 2019.

Pfannerstill, E. Y., Reijrink, N. G., Edtbauer, A., Ringsdorf, A., Zannoni, N., Araújo, A., Ditas, F., Holanda, B. A., Sá, M. O., Tsokankunku, A., Walter, D., Wolff, S., Lavrič, J. V., Pöhlker,

C., Sörgel, M., and Williams, J.: Total OH reactivity over the Amazon rainforest: variability with temperature, wind, rain, altitude, time of day, season, and an overall budget closure, Atmos. Chem. Phys., 21, 6231–6256, https://doi.org/10.5194/acp-21-6231-2021, 2021.

Richards-Henderson, N. K., Pham, A. T., Kirk, B. B., and Anastasio, C.: Secondary organic aerosol from aqueous reactions of green leaf volatiles with organic triplet excited states and singlet molecular oxygen, Environ. Sci. Technol., 49, 268–276, https://doi.org/10.1021/es503656m, 2015.

Rohrer, F. and Berresheim, H.: Strong correlation between levels of tropospheric hydroxyl radicals and solar ultraviolet radiation, Nature, 442, 184–187, https://doi.org/10.1038/nature04924, 2006.

Rolph, G., Stein, A., and Stunder, B.: Real-time Environmental Applications and Display sYstem: READY, Environ. Model. Softw., 95, 210–228, https://doi.org/10.1016/j.envsoft.2017.06.025, 2017.

Rossignol, S., Aregahegn, K. Z., Tinel, L., Fine, L., Nozière, B., and George, C.: Glyoxal induced atmospheric photosensitized chemistry leading to organic aerosol growth, Environ. Sci. Technol., 48, 3218–3227, https://doi.org/10.1021/es405581g, 2014.

Schauer, J. J., Kleeman, M. J., Cass, G. R., and Simoneit, B. R.: Measurement of emissions from air pollution sources. 3. C1-C29 organic compounds from fireplace combustion of wood, Environ. Sci. Technol., 35, 1716–1728, https://doi.org/10.1021/es001331e, 2001.

Schmitt, M., Erickson, P. R., and McNeill, K.: Triplet-State Dissolved Organic Matter Quantum Yields and Lifetimes from Direct Observation of Aromatic Amine Oxidation, Environ. Sci. Technol., 51, 13151–13160, https://doi.org/10.1021/acs.est.7b03402, 2017.

Seinfeld, J. H. and Pandis, S. N.: Atmospheric Chemistry And Physics: From Air Pollution To Climate Change, 3rd edn., Wiley, Hoboken, New Jersey, ISBN 978-1-118-94740-1, 2016.

Sharpless, C. M., Aeschbacher, M., Page, S. E., Wenk, J., Sander, M., and McNeill, K.: Photooxidation-induced changes in optical, electrochemical, and photochemical properties of humic substances, Environ. Sci. Technol., 48, 2688–2696, https://doi.org/10.1021/es403925g, 2014.

Silva, P. J., Liu, D.-Y., Noble, C. A., and Prather, K. A.: Size and chemical characterization of individual particles resulting from biomass burning of local Southern California species, Environ. Sci. Technol., 33, 3068–3076, https://doi.org/10.1021/es980544p, 1999.

Smith, J. D., Sio, V., Yu, L., Zhang, Q., and Anastasio, C.: Secondary organic aerosol production from aqueous reactions of atmospheric phenols with an organic triplet excited state, Environ. Sci. Technol., 48, 1049–1057, https://doi.org/10.1021/es4045715, 2014.

Smith, J. D., Kinney, H., and Anastasio, C.: Aqueous benzene-diols react with an organic triplet excited state and hydroxyl radical to form secondary organic aerosol, Phys. Chem. Chem. Phys., 17, 10227–10237, https://doi.org/10.1039/c4cp06095d, 2015.

Stein, A. F., Draxler, R. R., Rolph, G. D., Stunder, B. J. B., Cohen, M. D., and Ngan, F.: Noaa's HYSPLIT atmospheric transport and dispersion modeling system, B. Am. Meteorol. Soc., 96, 2059–2077, https://doi.org/10.1175/BAMS-D-14-00110.1, 2015.

Tilgner, A. and Herrmann, H.: Tropospheric aqueous-phase OH oxidation chemistry: current understanding, uptake of highly oxidized organics and its effects, in: Multiphase environmental chemistry in the atmosphere, vol. 1299, edited by: Hunt, S. W., Laskin, A., and Nizkorodov, S. A., American Chemical Society, Washington, DC, 49–85, https://doi.org/10.1021/bk-2018-1299.ch004, 2018.

Tong, H., Arangio, A. M., Lakey, P. S. J., Berkemeier, T., Liu, F., Kampf, C. J., Brune, W. H., Pöschl, U., and Shiraiwa, M.: Hydroxyl radicals from secondary organic aerosol decomposition in water, Atmos. Chem. Phys., 16, 1761–1771, https://doi.org/10.5194/acp-16-1761-2016, 2016.

U.S. Geological Survey: Dissolved oxygen: U.S. Geological Survey Techniques and Methods, book 9, chap. A6.2, 33 pp., https://doi.org/10.3133/tm9A6.2, 2020.

Verma, V., Fang, T., Xu, L., Peltier, R. E., Russell, A. G., Ng, N. L., and Weber, R. J.: Organic aerosols associated with the generation of reactive oxygen species (ROS) by water-soluble $PM_{2.5}$, Environ. Sci. Technol., 49, 4646–4656, https://doi.org/10.1021/es505577w, 2015.

Vicente, A., Alves, C., Calvo, A. I., Fernandes, A. P., Nunes, T., Monteiro, C., Almeida, S. M., and Pio, C.: Emission factors and detailed chemical composition of smoke particles from the 2010 wildfire season, Atmos. Environ., 71, 295–303, https://doi.org/10.1016/j.atmosenv.2013.01.062, 2013.

Wander, R., Neta, P., and Dorfman, L. M.: Pulse radiolysis studies. XII. Kinetics and spectra of the cyclohexadienyl radicals in aqueous benzoic acid solution, J. Phys. Chem., 72, 2946–2949, https://doi.org/10.1021/j100854a044, 1968.

Wang, G., Zhang, R., Gomez, M. E., Yang, L., Levy Zamora, M., Hu, M., Lin, Y., Peng, J., Guo, S., Meng, J., Li, J., Cheng, C., Hu, T., Ren, Y., Wang, Y., Gao, J., Cao, J., An, Z., Zhou, W., Li, G., Wang, J., Tian, P., Marrero-Ortiz, W., Secrest, J., Du, Z., Zheng, J., Shang, D., Zeng, L., Shao, M., Wang, W., Huang, Y., Wang, Y., Zhu, Y., Li, Y., Hu, J., Pan, B., Cai, L., Cheng, Y., Ji, Y., Zhang, F., Rosenfeld, D., Liss, P. S., Duce, R. A., Kolb, C. E., and Molina, M. J.: Persistent sulfate formation from London Fog to Chinese haze, P. Natl. Acad. Sci. USA, 113, 13630–13635, https://doi.org/10.1073/pnas.1616540113, 2016.

Wang, H., Zhou, H., Ma, J., Nie, J., Yan, S., and Song, W.: Triplet photochemistry of dissolved black carbon and its effects on the photochemical formation of reactive oxygen species, Environ. Sci. Technol., 54, 4903–4911, https://doi.org/10.1021/acs.est.0c00061, 2020.

Wang, X., Gemayel, R., Hayeck, N., Perrier, S., Charbonnel, N., Xu, C., Chen, H., Zhu, C., Zhang, L., Wang, L., Nizkorodov, S. A., Wang, X., Wang, Z., Wang, T., Mellouki, A., Riva, M., Chen, J., and George, C.: Atmospheric photosensitization: A new pathway for sulfate formation, Environ. Sci. Technol., 54, 3114–3120, https://doi.org/10.1021/acs.est.9b06347, 2020.

Wenk, J. and Canonica, S.: Phenolic antioxidants inhibit the triplet-induced transformation of anilines and sulfonamide antibiotics in aqueous solution, Environ. Sci. Technol., 46, 5455–5462, https://doi.org/10.1021/es300485u, 2012.

Wenk, J., von Gunten, U., and Canonica, S.: Effect of dissolved organic matter on the transformation of contaminants induced by excited triplet states and the hydroxyl radical, Environ. Sci. Technol., 45, 1334–1340, https://doi.org/10.1021/es102212t, 2011.

Wenk, J., Eustis, S. N., McNeill, K., and Canonica, S.: Quenching of excited triplet states by dissolved natural organic matter, Environ. Sci. Technol., 47, 12802–12810, https://doi.org/10.1021/es402668h, 2013.

Wilkinson, F., Helman, W. P., and Ross, A. B.: Rate constants for the decay and reactions of the lowest electronically excited singlet state of molecular oxygen in solution. an expanded and revised compilation, J. Phys. Chem. Ref. Data, 24, 663–677, https://doi.org/10.1063/1.555965, 1995.

Wong, J. P. S., Nenes, A., and Weber, R. J.: Changes in light absorptivity of molecular weight separated brown carbon due to photolytic aging, Environ. Sci. Technol., 51, 8414–8421, https://doi.org/10.1021/acs.est.7b01739, 2017.

Wong, J. P. S., Tsagkaraki, M., Tsiodra, I., Mihalopoulos, N., Violaki, K., Kanakidou, M., Sciare, J., Nenes, A., and Weber, R. J.: Effects of atmospheric processing on the oxidative potential of biomass burning organic aerosols, Environ. Sci. Technol., 53, 6747–6756, https://doi.org/10.1021/acs.est.9b01034, 2019.

Yu, L., Smith, J., Laskin, A., Anastasio, C., Laskin, J., and Zhang, Q.: Chemical characterization of SOA formed from aqueous-phase reactions of phenols with the triplet excited state of carbonyl and hydroxyl radical, Atmos. Chem. Phys., 14, 13801–13816, https://doi.org/10.5194/acp-14-13801-2014, 2014.

Zeinali, N., Oluwoye, I., Altarawneh, M. K., Almatarneh, M. H., and Dlugogorski, B. Z.: Probing the Reactivity of Singlet Oxygen with Cyclic Monoterpenes, ACS Omega, 4, 14040–14048, https://doi.org/10.1021/acsomega.9b01825, 2019.

Zeng, L., Dibb, J., Scheuer, E., Katich, J. M., Schwarz, J. P., Bourgeois, I., Peischl, J., Ryerson, T., Warneke, C., Perring, A. E., Diskin, G. S., DiGangi, J. P., Nowak, J. B., Moore, R. H., Wiggins, E. B., Pagonis, D., Guo, H., Campuzano-Jost, P., Jimenez, J. L., Xu, L., and Weber, R. J.: Characteristics and evolution of brown carbon in western United States wildfires, Atmos. Chem. Phys., 22, 8009–8036, https://doi.org/10.5194/acp-22-8009-2022, 2022.

Zhang, X., Lin, Y.-H., Surratt, J. D., and Weber, R. J.: Sources, Composition and Absorption Ångström Exponent of Light-absorbing Organic Components in Aerosol Extracts from the Los Angeles Basin, Environ. Sci. Technol., 47, 3685–3693, https://doi.org/10.1021/es305047b, 2013.

Zhao, R., Lee, A. K. Y., Huang, L., Li, X., Yang, F., and Abbatt, J. P. D.: Photochemical processing of aqueous atmospheric brown carbon, Atmos. Chem. Phys., 15, 6087–6100, https://doi.org/10.5194/acp-15-6087-2015, 2015.

Zuo, Y. and Hoigné, J.: Formation of hydrogen peroxide and depletion of oxalic acid in atmospheric water by photolysis of iron(III)-oxalato complexes, Environ. Sci. Technol., 26, 1014–1022, https://doi.org/10.1021/es00029a022, 1992.

Supplement of Atmos. Chem. Phys., 24, 1–21, 2024
https://doi.org/10.5194/acp-24-1-2024-supplement

Atmospheric Chemistry and Physics Open Access

Supplement of

Seasonal variations in photooxidant formation and light absorption in aqueous extracts of ambient particles

Lan Ma et al.

Correspondence to: Cort Anastasio (canastasio@ucdavis.edu)

Table of contents

Table S1. Particle collection and PME sample information

Sample Type	Sample ID	Collection dates[a]	Sampling duration (days)	Average $PM_{2.5}$ conc.[b] ($\mu g/m^3$)	PME particle mass/water ratio[c] (10^{-4} µg PM/µg H_2O)	α_{300}[d] (cm^{-1})	α_{365}[e] (cm^{-1})	R_{abs} (300-450 nm) (10^{-6} mol-photons $L^{-1}s^{-1}$)[f]	AAE[g]	E_2/E_3[h]	MAC_{DOC} (300 nm) (m^2 (g C)$^{-1}$)[i]	MAC_{DOC} (365 nm) (m^2 (g C)$^{-1}$)[i]	DOC (mg C L^{-1})	Light screening factor[j]	
														PME	PME+ DMB
Winter & Spring	PME-111519	11/12/19-11/19/19	7.00	13.2	9.1 (0.3)	1.534	0.431	25	7.59	7.45	1.82	0.52	192	0.67	0.59
	PME-120319	12/3/19	1.00	10.6	1.2 (0.2)	0.112	0.027	1.6	8.17	8.84	1.57	0.40	16	0.97	0.75
	PME-122019	12/17/19-12/24/19	7.01	9.0	5.4 (0.4)	0.718	0.206	12	7.64	7.37	2.33	0.69	69	0.82	0.69
	PME-010220	1/2/20	1.01	10.2	1.1 (0.1)	0.116	0.031	1.8	7.78	8.28	1.54	0.43	17	0.97	0.75
	PME-010620	1/3/20-1/10/20	7.01	10.0	6.2 (0.5)	0.552	0.144	8.4	7.57	8.65	1.92	0.52	64	0.86	0.71
	PME-021620[k]	2/5/20-2/28/20	7.07	9.1	4.6 (0.5)	0.868	0.269	16	7.21	7.16	2.08	0.65	95	0.60	0.53
	PME-022020	2/20/20	1.00	9.0	0.89 (0.10)	0.231	0.070	4.1	7.26	6.91	2.50	0.76	21	0.94	0.75
	PME-030420	3/4/20	1.01	8.4	1.2 (0.2)	0.090	0.022	1.3	8.05	9.61	1.27	0.32	16	0.98	0.75
Summer & Fall	PME-070720	7/7/20	0.99	7.0	1.0 (0.2)	0.039	0.009	0.50	8.77	10.9	0.74	0.18	12	0.99	0.75
	PME-080420	8/4/20	1.01	7.2	0.79 (0.14)	0.019	0.004	0.22	8.97	17.0	0.43	0.09	9.9	1.00	0.75
	PME-101520	10/15/20	1.00	7.9	0.66 (0.25)	0.017	0.004	0.18	9.63	13.3	0.78	0.16	5.0	1.00	0.75
Fresh wildfire	PME-081920	8/19/20	0.99	67.9	3.7 (0.3)	1.960	0.812	43	7.26	4.22	3.82	1.59	118	0.55	0.50
	PME-082220[k]	8/21/20-8/24/20	1.20	49.3	4.1 (0.1)	2.017	0.653	38	7.15	6.50	3.10	1.00	150	0.78	0.67
	PME-082420	8/24/20	0.92	57.2	3.1 (0.2)	1.511	0.540	29	7.57	5.00	3.32	1.19	105	0.64	0.57
	PME-090920	9/9/20	1.00	44.6	3.0 (0.2)	0.871	0.259	15	7.42	7.46	2.90	0.86	69	0.78	0.67
Aged wildfire	PME-090120	9/1/20	0.99	19.2	1.4 (0.1)	0.199	0.048	2.8	8.19	10.6	1.75	0.42	26	0.95	0.75
	PME-091520	9/15/20	1.00	19.5	1.3 (0.1)	0.245	0.058	3.5	7.85	11.8	1.54	0.36	37	0.88	0.72
	PME-100820	10/8/20	0.99	33.9	2.7 (0.2)	0.441	0.090	5.4	7.58	15.1	1.25	0.26	81	0.90	0.73
Averages															
Winter & Spring (Win-Spr)				9.9 (1.5)					7.7 (0.3)	8.0 (1.0)	1.88 (0.42)	0.53 (0.15)			
Summer & Fall (Sum-Fall)				7.4 (0.4)					9.1 (0.5)	13.7 (3.1)	0.65 (0.19)	0.14 (0.05)			
Fresh wildfire (FBB)				55 (10)					7.3 (0.2)	5.8 (1.5)	3.29 (0.40)	1.16 (0.31)			
Aged wildfire (ABB)				24 (8)					7.9 (0.3)	12.5 (2.3)	1.51 (0.25)	0.35 (0.08)			

Field blanks[l]														
FB1	8/4/20	3 min	6.9	0.16 (0.06)	0.0022	0.0004	0.017				0	2.12	1	
FB2	1/2/20	3 min	15.6	0.13 (0.06)	0.0015	0	0.0013				0.16	2.04	1	
FB3	10/5/20	3 min	39.6	0.47 (0.38)	0.0065	0.0014	0.086				0	2.98	1	

Listed uncertainties (in parentheses) are ± 1 standard deviation. Values in the table are not normalized by the sampling duration.

[a] For 24-h samples, sampling started in the morning of the first date shown and ended on the second date.

[b] Average ambient $PM_{2.5}$ concentration for each sampling period measured at the UC Davis sampling site by the California Air Resources as reported on the AQMIS online database (California Air Resources Board AQMIS Database: https://www.arb.ca.gov/aqmis2/aqmis2.php, last access: 12 July 2022.)

[c] Average particle mass/water mass ratio (± 1σ) in each extract, calculated as the extracted particle mass per square (determined as the difference of filter weights before and after extraction) divided by the mass of water used to extract the square. Each value is an upper bound because the measured mass of PM extracted includes insoluble material that would be removed by the subsequent filtration step.

[d] Base-10 absorption coefficient of the extract (in cm^{-1}) at 300 nm.

[e] Base-10 absorption coefficient of the extract (in cm^{-1}) at 365 nm.

[f] Rate of sunlight absorption by PME between 300 and 450 nm, calculated by equation 2 in Kaur et al. (2019), using midday actinic flux on the winter solstice in Davis (photons cm^{-2} s^{-1} nm^{-1}) from the Tropospheric Ultraviolet and Visible (TUV) Radiation Model version 4.1.

[g] AAE (Ångstrom Absorption Exponent) is calculated as the negative slope of a linear regression between ln(absorbance) vs. ln(wavelength) in the 300 – 450 nm wavelength range.

[h] The ratio of absorbance at 250 nm divided by absorbance at 365 nm.

[i] Mass absorption coefficient at 300 or 365 nm normalized by dissolved organic carbon, calculated as $MAC_{DOC,\lambda} = \frac{\alpha_\lambda \times \ln(10) \times 10^6}{[DOC]}$ (Kaur et al., 2019). The nitrate and nitrite contributions to absorbance at each wavelength were subtracted but were very small, < 5 % of total absorbance at either wavelength.

[j] Light-absorption-weighted internal screening factor, calculated with equation 2 in Smith et al. (2016), using the midday winter solstice actinic flux in Davis. The wavelength range used is 280-364 nm. A value of 1 indicates no light screening while a low value represents a strong screening effect. The "PME" column shows light screening factors in PME samples, while the "PME+DMB" column shows values in the PME with added 80 μM DMB (which was used for inhibition factor measurements; see Section S1). The cell pathlength was 0.5 cm.

[k] These two samples are the interpolations of the winter and summer samples, respectively, from our previous work on the dependence of photooxidant concentration on dilution (Ma et al., 2023a). Their particle mass/water mass ratios, absorbances, and DOC values were estimated for an equivalent extraction volume of 1.0 mL water/square by interpolating from the winter or summer linear trend for each variable as a function of concentration factor.

[l] Field blank filters were obtained using the same procedure as for samples, by loading clean filters into the sampler and turning on the pump for 3 min. Field blank samples were extracted with 1.0 mL water/square.

Table S2. Ion concentrations in PMEs

Sample Type	Sample ID	Sampling duration (days)	$[NO_3^-]$ (μM)	$[NO_2^-]$ (μM)	$[SO_4^{2-}]$ (μM)[a]	$[Cl^-]$ (μM)	$[HCOO^-]$ (μM)	$[NH_4^+]$ (μM)	$[Na^+]$ (μM)	$[K^+]$ (μM)	$[Ca^{2+}]$ (μM)
Winter & Spring	PME-111519	7.00	2660	8.98	838	811[b]	76.4	4857	718	1187[b]	373
	PME-120319	1.00	541	0.87	39.6	17.4	3.5	653	151	79.1	28.0
	PME-122019	7.01	3309	2.65	296	167[b]	61.0	2198	246	84.7[b]	70.1
	PME-010220	1.01	424	0.69	25.2	10.7	3.4	516	147	64.7	28.0
	PME-010620	7.01	3075	3.14	400	750[b]	56.0	1620	183	272[b]	141
	PME-021620[e]	7.07	1480	6.08	617	37.3	51.5	1300	1159	214	402
	PME-022020	1.00	84.0	0.81	58.0	0.3	3.8	168	165	61.8	28.1
	PME-030420	1.01	356	0.75	65.2	66.7	18.2	99.4	138	26.3	28.0
Summer & Fall	PME-070720	0.99	117	0.63	69.5	238	5.8	65.5	548	36.9	187
	PME-080420	1.01	90.0	0.50	87.1	1654[b]	10.3	78.7	457	1559[b]	143
	PME-101520	1.00	25.5	0.44	-9.1	17.1	0.5	58.5	240	22.7	28.0
Fresh wildfire	PME-081920	0.99	288	1.88	76.3	72.3	81.6	46.2	127	122	200
	PME-082220[e]	1.20	299	2.50	173	51.8	64.2	460	529	219	233
	PME-082420	0.92	179	1.72	157	516[b]	32.9	502	292	676[b]	184
	PME-090920	1.00	219	1.42	82.9	23.7	69.3	66.3	109	64.3	210
Aged wildfire	PME-090120	0.99	180	0.75	99.1	64.1	14.6	65.8	538	53.8	193
	PME-091520	1.00	66.1	0.63	29.8	0.5	< LOD[d]	112	195	55.3	111
	PME-100820	0.99	204	1.26	83.0	1164[b]	20.8	803	300	1310[b]	137
Field blanks											
FB1[c]		3 min	3.12	<LOD[d]	< 0	2458	3.03	0.12	96.0	ND[f]	7.01
FB2		3 min	4.58	<LOD[d]	< 0	1.07	2.94	1.42	93.8	5.92	7.02
FB3		3 min	1.99	<LOD[d]	12.4	0.65	5.54	1.11	124.6	8.88	7.08

Values in the table are not normalized by the sampling duration.

[a] The amount of added sulfuric acid for pH adjustment (typically 90 μM) has been subtracted.

[b] These samples were contaminated by pH electrode filling solution (potassium chloride) during pH adjustment. These samples are not included in the discussion of K^+ concentrations in the main text.

[c] This field blank sample was contaminated by the pH electrode filling solution, resulting in an extremely high Cl^- concentration.

[d] Below limit of detection.

[e] These two samples are the interpolations of the winter and summer samples, respectively, from our previous work on the dependence of photooxidant concentration on dilution (Ma et al., 2023a). Their ion concentration values were estimated by interpolation from the winter or summer linear trend for each variable with concentration factor to an equivalent extraction volume of 1.0 mL water/square.

[f] Not determined due to the poor ion chromatogram result.

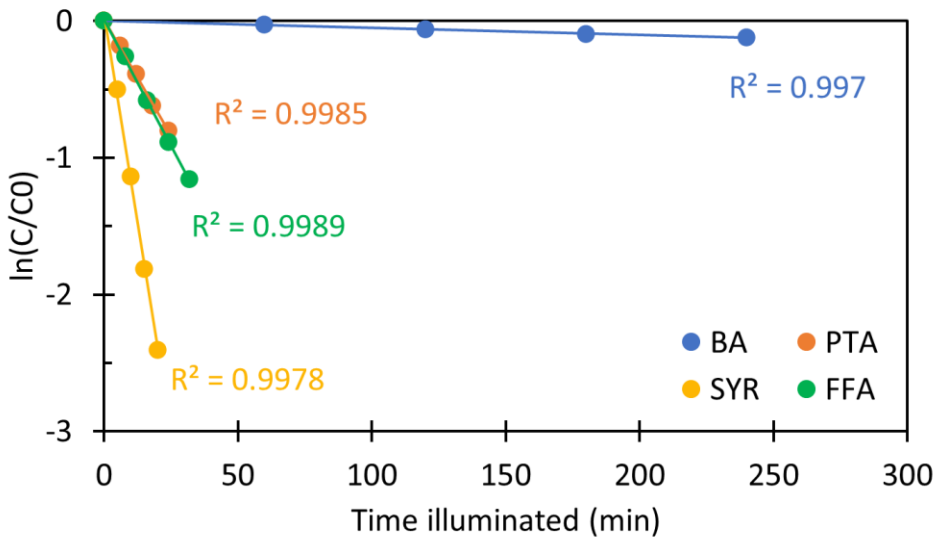

Figure S1. Representative plots of probe decay kinetics, from extract PME-090120, for our four probes: benzoic acid (BA, blue), (phenylthio)acetic acid (PTA, orange), syringol (SYR, yellow), and furfuryl alcohol (FFA, green). Solid lines are linear regressions for the probes. For FFA, SYR, and PTA, around 90% of our probe kinetics were pseudo first order. For BA, over 60% of the samples followed pseudo first order decay.

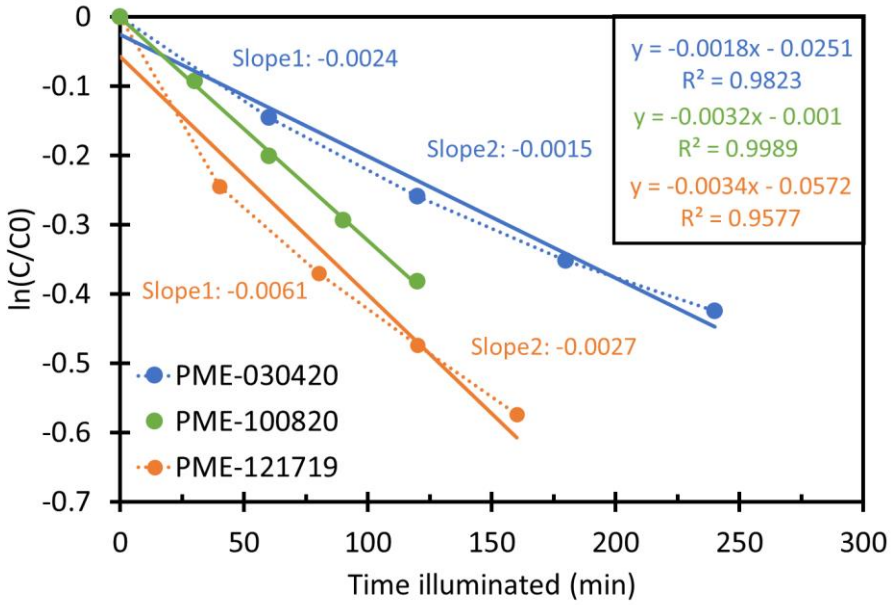

Figure S2. Representative plots of benzoic acid decay kinetics in aqueous particle extracts showing samples where: (1) the initial rate of BA loss is roughly twice as fast as the later rate (orange), (2) the initial rate is roughly 50% higher than the later rate (blue) and (3) there is no difference in BA decay over the course of illumination (green). For roughly half of our samples, BA decay was first order, i.e., there was no change in the rate of loss during illumination. Solid lines are linear regressions to all points for a given sample, while their regression equations are shown in the right top box. For the orange and blue data, Slope 1 and Slope 2 represent slopes from linear regressions of the first two and last four data points, respectively.

Table S3. Hydroxyl radical measurements

Sample Type	Sample ID	P_{OH} (10^{-9} $M^{-1}s^{-1}$)[a]	k'_{OH} (10^{6} s^{-1})[b]	[•OH][c] (10^{-15} M) from BA	[•OH][d] (10^{-15} M) from *p*-HBA	Average [•OH] (10^{-15} M)[e]	$10^4 \times \Phi_{OH}$[f]	$\%P_{OH,NO3-}$[g]	$\%P_{OH,NO2-}$[h]
Winter & Spring	PME-111519	14 (2)	4.3 (0.6)	2.4 (0.3)	3.9 (0.5)	3.2 (0.3)	5.4 (0.9)	2.7 (0.4)	1.7 (0.3)
	PME-120319	0.44 (0.06)	0.36 (0.05)	1.4 (0.1)	1.1 (0.1)	1.2 (0.1)	2.7 (0.4)	17 (2)	5.1 (0.7)
	PME-122019	6.0 (0.9)	1.6 (0.2)	3.0 (0.4)	4.8 (0.5)	3.9 (0.3)	5.1 (0.8)	7.7 (1.2)	1.1 (0.2)
	PME-010220	0.60 (0.08)	0.38 (0.05)	1.6 (0.1)	1.5 (0.1)	1.6 (0.1)	3.3 (0.4)	9.9 (1.3)	3.0 (0.4)
	PME-010620	6.7 (1.0)	1.4 (0.2)	3.5 (0.3)	5.8 (0.5)	4.7 (0.3)	7.9 (1.1)	6.5 (0.9)	1.2 (0.2)
	PME-021620[i]	10 (2)	2.1 (0.3)			4.7 (0.4)	6.3 (0.1)	2.1 (0.4)	1.6 (0.2)
	PME-022020	0.45 (0.06)	0.48 (0.06)	1.1 (0.1)	0.83 (0.1)	0.94 (0.05)	1.1 (0.2)	2.6 (0.4)	4.7 (0.7)
	PME-030420	0.52 (0.08)	0.36 (0.05)	1.4 (0.1)	1.5 (0.2)	1.5 (0.1)	4.0 (0.6)	9.5 (1.4)	3.7 (0.6)
Summer & Fall	PME-070720	0.20 (0.03)	0.26 (0.03)	0.90 (0.03)	0.59 (0.1)	0.74 (0.05)	3.9 (0.6)	8.4 (1.2)	8.4 (1.2)
	PME-080420	0.050 (0.026)	0.22 (0.03)		0.23 (0.03)	0.23 (0.03)	2.3 (0.4)	25 (13)	26 (13)
	PME-101520	0.038 (0.015)	0.11 (0.01)	0.28 (0.19)	0.30 (0.15)	0.34 (0.12)	1.6 (0.6)	9.2 (3.5)	30 (11)
Fresh wildfire	PME-081920	7.3 (1.3)	2.7 (0.3)	2.6 (0.5)	2.9 (0.4)	2.8 (0.3)	1.7 (0.3)	0.55 (0.10)	0.67 (0.12)
	PME-082220[i]	8.7 (1.3)	3.4 (0.4)			2.6 (0.2)	2.3 (0.3)	0.48 (0.07)	0.75 (0.11)
	PME-082420	4.8 (1.2)	2.4 (0.3)	2.1 (0.2)	1.9 (0.9)	2.0 (0.4)	1.7 (0.3)	0.52 (0.13)	0.93 (0.24)
	PME-090920	4.2 (0.9)	1.6 (0.2)	2.0 (0.1)	3.4 (0.9)	2.7 (0.5)	2.8 (0.3)	0.73 (0.16)	0.88 (0.19)
Aged wildfire	PME-090120	0.28 (0.04)	0.59 (0.08)	0.43 (0.01)	0.53 (0.1)	0.48 (0.03)	1.0 (0.1)	9.0 (1.3)	7.0 (1.0)
	PME-091520	1.1 (0.1)	0.82 (0.11)	1.6 (0.01)	1.2 (0.1)	1.4 (0.1)	3.2 (0.4)	0.82 (0.11)	1.4 (0.2)
	PME-100820	5.7 (0.8)	1.8 (0.2)	3.0 (0.2)	3.3 (0.2)	3.2 (0.2)	10 (1.5)	0.50 (0.07)	0.57 (0.08)
Averages[j]									
Winter & Spring						1.5 (0.3)	4.5 (2.2)	7.2 (5.0)	2.8 (1.6)
Summer & Fall						0.41 (0.03)	2.8 (1.0)	7.1 (6.5)	17 (22)
Fresh wildfire						2.5 (0.3)	2.1 (0.5)	0.57 (0.11)	0.81 (0.12)
Aged wildfire						1.7 (1.4)	4.9 (5.0)	3.4 (4.8)	3.0 (3.5)
Field Blanks									
FB1						0.57 (0.03)			
FB2[k]		0.011 (0.001)	0.20 (0.02)			0.06 (0.01)		5.7 (0.5)	36 (3)
FB3[k]		0.008 (0.001)	0.05 (0.02)			0.15 (0.01)		3.6 (0.4)	26 (3)

Listed uncertainties (in parentheses) are ± 1 standard error from the errors in regressions, except for the averages, which are ± 1σ. Values in the table are not normalized by the sampling duration, but the average [•OH] was calculated after normalizing 7-day concentrations to 1 day.

[a] Davis winter solstice-normalized rate of •OH photoproduction, calculated as $P_{OH} = k'_{OH} \times$ [•OH].

[b] Apparent pseudo-first-order rate constant for destruction of •OH due to natural sinks, estimated as $k'_{OH} = k_{OH+DOC} \times$ [DOC], where k_{OH+DOC} is (2.7 (±0.4) $\times 10^8$ L (mol C)$^{-1}$ s^{-1}), the average second-order rate constant of DOC reacting with •OH from the samples in Ma et al. (2023a).

[c] Winter solstice-normalized steady-state concentration of •OH determined from BA decay.

[d] Winter solstice-normalized steady-state concentration of •OH determined from *p*-HBA formation.

[e] Average of concentrations of $^{\bullet}OH$ determined by BA and *p*-HBA. For PME-080420 with a poor BA decay, only the value from *p*-HBA is used.

[f] Apparent quantum yield of $^{\bullet}OH$ during simulated sunlight illumination, calculated as $\Phi_{OH} = P_{OH}/R_{abs.}$

[g] Percentage of $^{\bullet}OH$ photoproduction due to nitrate photolysis. This was calculated as $(j_{NO3^-\rightarrow OH} \times [NO_3^-])/P_{OH}$, using an aqueous nitrate photolysis rate constant, $j_{NO3^-\rightarrow OH} = 1.4 \times 10^{-7}\ s^{-1}$ (Anastasio and McGregor, 2001) and the measured molar concentration of NO_3^-.

[h] Percentage of $^{\bullet}OH$ photoproduction due to of nitrite photolysis. This was calculated as $(j_{NO2^-\rightarrow OH} \times [NO_2^-])/P_{OH}$, using an aqueous nitrite photolysis rate constant, $j_{NO2^-\rightarrow OH} = 2.6 \times 10^{-5}\ s^{-1}$ (Anastasio and McGregor, 2001) and the measured molar concentration of NO_2^-.

[i] These two samples are the interpolated winter and summer samples, respectively, from our previous work on the dependence of photooxidant concentration on dilution (Ma et al., 2023a). The $^{\bullet}OH$ concentration in PME-021620 was the average concentration of the winter dilution series because their concentration is independent of concentration factor. The $^{\bullet}OH$ concentration in PME-081920 was estimated by interpolating the linear trends between [$^{\bullet}OH$] and concentration factor in the summer dilution series to an equivalent extraction volume of 1 mL water/square.

[j] The average value of each sample type. For the average [$^{\bullet}OH$] calculation, the $^{\bullet}OH$ concentration normalized by sampling duration is used.

[k] The $^{\bullet}OH$ production rate in field blanks was determined by adding 1.2 mM benzoic acid to 1.0 mL FB sample and monitoring the formation of *p*-hydroxy benzoic acid, assuming that all $^{\bullet}OH$ produced reacts with benzoic acid.

Table S4. Singlet molecular oxygen measurements

Sample Type	Sample ID	$[^1O_2^*]$[a] (10^{-12} M)	P_{1O2^*}[b] (10^{-7} M s^{-1})	$f_{FFA,1O2^*}$[c]	$f_{FFA,OH}$[d]	Φ_{1O2^*}[e] (%)	$\Phi_{3C^*,SYR}/(\Phi_{1O2^*}/f_\Delta)$[f]	$\Phi_{3C^*,PTA}/(\Phi_{1O2^*}/f_\Delta)$[g]	$[^3C^*]_{SYR}/[^1O_2^*]$[h]	$[^3C^*]_{PTA}/[^1O_2^*]$[i]
Winter & Spring	PME-111519	4.5 (0.4)	9.9 (1.0)	0.85 (0.09)	0.17 (0.02)	4.0 (0.4)	0.81 (0.23)	0.45 (0.12)	0.17 (0.05)	0.10 (0.03)
	PME-120319	0.37 (0.07)	0.81 (0.16)	0.73 (0.15)	0.35 (0.01)	5.0 (1.0)	0.28 (0.08)	0.21 (0.07)	0.13 (0.04)	0.10 (0.03)
	PME-122019	2.5 (0.2)	5.5 (0.4)	0.76 (0.07)	0.37 (0.03)	4.6 (0.4)	0.52 (0.16)	0.24 (0.06)	0.18 (0.06)	0.08 (0.02)
	PME-010220	0.27 (0.06)	0.59 (0.12)	0.51 (0.11)	0.83 (0.04)	3.2 (0.7)	0.28 (0.09)	0.32 (0.10)	0.13 (0.04)	0.15 (0.05)
	PME-010620	2.3 (0.2)	5.1 (0.4)	0.81 (0.07)	0.47 (0.03)	6.0 (0.5)	0.24 (0.05)	0.26 (0.07)	0.08 (0.02)	0.09 (0.02)
	PME-021620[j]	1.9 (0.3)	4.2 (0.7)			2.7 (0.4)	0.58 (0.18)	0.38 (0.11)	0.18 (0.06)	0.11 (0.03)
	PME-022020	0.59 (0.06)	1.3 (0.1)	0.92 (0.11)	0.42 (0.02)	3.2 (0.3)	0.42 (0.09)	0.21 (0.06)	0.19 (0.04)	0.10 (0.03)
	PME-030420	0.20 (0.03)	0.44 (0.06)	0.52 (0.07)	1.03 (0.07)	3.4 (0.5)	0.14 (0.05)	0.24 (0.07)	0.07 (0.02)	0.11 (0.03)
Summer & Fall	PME-070720	0.17 (0.02)	0.38 (0.04)	1.01 (0.11)	1.23 (0.08)	7.5 (0.7)	0.29 (0.06)	0.10 (0.03)	0.14 (0.03)	0.05 (0.01)
	PME-080420	0.081 (0.027)	0.18 (0.06)	0.97 (0.33)	0.78 (0.39)	7.9 (2.7)	0.22 (0.09)	0.07 (0.04)	0.11 (0.04)	0.04 (0.02)
	PME-101520	0.068 (0.006)	0.15 (0.01)	1.46 (0.31)	0.82 (0.30)	8.4 (0.8)	0.54 (0.11)	0.15 (0.05)	0.28 (0.06)	0.08 (0.02)
Fresh wildfire	PME-081920	3.3 (0.6)	7.2 (1.2)	1.13 (0.22)	0.26 (0.03)	1.7 (0.3)	0.44 (0.12)	0.20 (0.07)	0.12 (0.03)	0.06 (0.02)
	PME-082220[j]	3.8 (1.0)	8.4 (2.1)			2.2 (0.6)	0.54 (0.18)	0.20 (0.07)	0.13 (0.05)	0.05 (0.02)
	PME-082420	3.0 (0.2)	6.7 (0.5)	0.80 (0.06)	0.02 (0.01)	2.3 (0.2)	0.71 (0.19)	0.19 (0.05)	0.21 (0.06)	0.06 (0.01)
	PME-090920	1.9 (0.2)	4.2 (0.5)	0.73 (0.09)	0.15 (0.03)	2.8 (0.3)	0.59 (0.34)	0.29 (0.19)	0.21 (0.12)	0.10 (0.06)
Aged wildfire	PME-090120	0.45 (0.06)	0.99 (0.12)	0.65 (0.09)	0.20 (0.01)	3.5 (0.4)	0.78 (0.19)	0.26 (0.07)	0.34 (0.08)	0.12 (0.03)
	PME-091520	0.50 (0.04)	1.1 (0.1)	0.56 (0.05)	0.44 (0.02)	3.2 (0.2)	0.63 (0.15)	0.27 (0.07)	0.26 (0.06)	0.11 (0.03)
	PME-100820	1.2 (0.2)	2.7 (0.4)	0.98 (0.13)	0.71 (0.04)	5.0 (0.7)	0.45 (0.10)	0.16 (0.04)	0.15 (0.03)	0.05 (0.01)
Averages[k]										
Winter & Spring		0.38 (0.16)				4.0 (1.1)	0.41 (0.22)	0.29 (0.09)	0.14 (0.05)	0.11 (0.02)
Summer & Fall		0.11 (0.06)				7.9 (0.4)	0.35 (0.17)	0.11 (0.04)	0.17 (0.09)	0.05 (0.02)
Fresh wildfire		2.9 (0.7)				2.2 (0.5)	0.57 (0.11)	0.22 (0.04)	0.17 (0.05)	0.07 (0.02)
Aged wildfire		0.73 (0.44)				3.9 (1.0)	0.62 (0.17)	0.23 (0.06)	0.25 (0.10)	0.09 (0.04)
Field blanks										
FB1		0.016 (±0.001)		0.81 (±0.15)	8.3 (±4.8)					
FB2		0.021 (±0.001)		0.66 (±0.33)	0.54 (±0.07)					
FB3		0.028 (±0.001)		0.97 (±0.17)	0.73 (±0.09)					

Listed uncertainties (in parentheses) are ± 1 standard error propagated from the errors in regressions and rate constants, except for the averages, where uncertainties are ± 1σ. Values in the table are not normalized by the sampling duration, but the average $[^1O_2^*]$ was calculated using 7-day concentrations normalized to 1 day.

[a] Davis winter solstice-normalized steady-state concentration of $^1O_2^*$.

[b] Production rate of $^1O_2^*$, calculated as $P_{1O2^*} = [^1O_2^*] \times k'_{H2O}$, where k'_{H2O} is the first-order rate constant for loss of $^1O_2^*$ in H_2O (2.2×10^5 s^{-1}) (Bilski et al., 1997).

[c] Fraction of FFA lost due to $^1O_2$* in PME diluted with H_2O (i.e., 0.5 mL PME + 0.5 mL H_2O), calculated as $f_{FFA,1O2*} = [^1O_2*]/2 \times k_{FFA+1O2*}/k'_{FFA,H2O}$, where $k_{FFA+1O2*}$ is the second-order rate constant of FFA reacting with $^1O_2$*, and $k'_{FFA,H2O}$ is the normalized first-order decay rate of FFA in the PME diluted with H_2O.

[d] Fraction of FFA lost due to $^{\bullet}OH$ in PME diluted with H_2O, estimated as $f_{FFA,OH} = [^{\bullet}OH] \times k_{FFA+OH}/k'_{FFA,H2O}$, where k_{FFA+OH} is the second-order rate constant of FFA reacting with $^{\bullet}OH$ (1.5×10^{10} M^{-1} s^{-1}) (Ross and Ross, 1977), assuming $^{\bullet}OH$ concentration is the same in the diluted and undiluted PME.

[e] Apparent quantum yield of $^1O_2$*, calculated as $\Phi_{1O2*} = P_{1O2*}/R_{abs}$.

[f] Fraction of oxidizing triplets determined by SYR to the total triplet pool (Kaur and Anastasio, 2018). f_{Δ} is the yield of $^1O_2$* from oxygen quenching of triplet states, assumed to be 0.53 (McNeill and Canonica, 2016). $\Phi_{3C*,SYR}$ is the apparent quantum yield of ^3C* determined by SYR (See Table S7).

[g] Fraction of oxidizing triplets determined by PTA to the total triplet pool.

[h] Ratio of triplet concentration determined by SYR to the singlet oxygen concentration.

[i] Ratio of triplet concentration determined by PTA to the singlet oxygen concentration.

[j] These two samples are the interpolated winter and summer samples, respectively, from Ma et al. (2023a). $^1O_2$* concentrations were estimated by interpolating the linear trends between [$^1O_2$*] and concentration factor in PME-10, PME-2, and PME-0.7 samples, to an equivalent extraction volume of 1 mL water/square.

[k] Average value of each sample type. The $^1O_2$* concentration normalized by sampling duration was used for calculating average $^1O_2$* concentrations.

Table S5. Rate constants of SYR and PTA reacting with triplet excited states, singlet oxygen, and hydroxyl radical at pH 4.2

Oxidants	k_{SYR+Ox} (M^{-1} s^{-1})	Reference	k_{PTA+Ox} (M^{-1} s^{-1})	Reference
$^{\bullet}OH$	20 (±4) × 10^9	(Smith et al., 2015)	10.3 (±0.6) × 10^9	(Ma et al., 2023b)
$^1O_2$*	3.6 (±0.7) × 10^7	(Tratnyek and Hoigne, 1991)	8.8 (±0.6) × 10^6	
^{3}DMB*	3.9 (±0.7) × 10^9	(Smith et al., 2015)	2.5 (±0.6) ×10^9	
Direct photodegradation	j_{SYR} (s^{-1})		j_{PTA} (s^{-1})	
	< 4.3 × 10^{-6}	(Kaur and Anastasio, 2018)	6.2 (±0.2) × 10^{-4}	(Ma et al., 2023b)

Section S1. Determining inhibition factors and correcting ^{3}C* concentrations

Dissolved organic matter in PME may inhibit the decay of SYR or PTA by triplets, leading to an underestimation of triplet concentration. Based on our previous research, SYR as a probe is more strongly inhibited than PTA (Ma et al., 2023b). To investigate and quantify the inhibition effect of PME on these two triplet probes, we measured inhibition factors (*IF*s) of FFA, SYR, and PTA for each sample, and used the *IF* values to correct meaasured ^{3}C* concentrations in PME. Details of inhibition factors are described in Canonica et al. (2008), Wenk et al. (2011), and Ma et al. (2023b). To measure *IF*, we monitored the loss of 10 μM probe in three illuminated solutions for each sample: (1) in the pH 4.2 PME; (2) in pH 4.2 Milli-Q water containing 80 μM of triplet precursor 3,4-dimethoxybenzaldehyde (DMB); and (3) in the pH 4.2 PME with added 80 μM DMB. During each illumination we determined the first-order rate constant of probe decay. The inhibition factor for the probe was calculated using

$$IF_P = \frac{k'_{DMB,PME} - k'_{PME}}{k'_{DMB}} \quad (S1)$$

where $k'_{DMB,PME}$ is the first-order decay rate constant of probe in solution containing both DMB and PME, while k'_{PME} and k'_{DMB} are the probe loss rate constants in PME alone and in Milli-Q water with DMB, respectively. All *k'* values were corrected for internal light screening using screening factors (S_λ); the PME and PME+DMB values are listed in Table S1, while the light screening factor for 80 μM DMB is 0.75. An *IF* value of 1 indicates there is no DOM inhibition on probe decay, while *IF* = 0 indicates complete inhibition of probe decay. Since IF_P can also be affected by DOM suppressing the ^{3}DMB* concentration, we use IF_{FFA} to quantify this triplet suppression (Ma et al., 2023b). To exclude the effect of triplet suppression on IF_{SYR} and IF_{PTA} (i.e., to quantify only inhibition due to probe regeneration), we use $IF_{SYR,corr}$ and $IF_{PTA,corr}$

$$IF_{P,corr} = \frac{IF_P}{IF_{FFA}} \quad (S2)$$

Theoretically, *IF* should not exceed 1, but we sometimes see this result. When *IF* is greater than 1, it suggests there is interaction between DOM in PME with DMB to form reactive species, and thus indicates no inhibition or suppression. Therefore, when IF_{FFA} or IF_P is greater than 1, we assume that $IF_{P,corr} = IF_P$ and we do not correct the ^{3}C* concentration if $IF_{P,corr} > 1$. In addition, IF_{PTA} and IF_{SYR} values are expected to be lower than IF_{FFA} because IF_{PTA} and IF_{SYR} are affected by both the triplet suppression and probe inhibition effects, while IF_{FFA} is only impacted by triplet suppression. However, in some samples the IF_{PTA} value is greater than IF_{FFA}, which might be attributed to the large error in IF_{FFA} measurement in cases where the difference between $k'_{DMB,PME}$ and k'_{PME} is small for FFA. In this case, we

assume the IF_{FFA} value equals IF_{PTA} (since PTA is very resistant to suppression; (Ma et al., 2023b)) and use this value to calculate $IF_{P,corr}$. The determined *IF* and $IF_{P,corr}$ values are shown in Table S6.

The uncorrected $^3C^*$ concentration is calculated with:

$$[^3C^*]_{P,uncorr} = \frac{k'_{P,3C*}}{k_{P+3DMB*}} \quad (S3)$$

where $k'_{P,3C*}$ is measured first-order rate constant of probe loss due to triplets and $k_{P+3DMB*}$ is the second-order rate constant of probe reacting with ^{3}DMB*. This assumes that triplets in our extracts have reactivities similar to triplet DMB, as we have found in our past work (Kaur and Anastasio, 2018; Kaur et al., 2019). However, it is possible that we are overestimating the P + $^3C^*$ rate constant by using DMB as a model; this would lead to an underestimate of the oxidizing triplet concentrations (Ma et al., 2023). To correct for the probe inhibition effect, [^{3}C*] is calculated using

$$[^3C^*]_P = \frac{[^3C^*]_{P,uncorr}}{IF_{P,corr}} \quad (S4)$$

As stated earlier, if $IF_{P,corr} > 1$, we do not apply a correction, i.e., we use $[^3C^*]_{P,corr} = [^3C^*]_{P,uncorr}$ The $^3C^*$ concentrations shown in the main text are the values after *IF* correction.

Table S6. Inhibition factors for FFA, SYR, and PTA

Sample Type	Sample ID	IF_{FFA}	IF_{SYR}	IF_{PTA}	$IF_{SYR,corr}$	$IF_{PTA,corr}$
Winter & Spring	PME-111519	0.60 (0.45)	0.27 (0.04)	1.06 (0.13)	0.27 (0.04)	1.06 (0.13)
	PME-120319	1.15 (0.12)	0.78 (0.04)	1.16 (0.07)	0.78 (0.04)	1.16 (0.07)
	PME-122019	1.30 (0.12)	0.21 (0.04)	1.26 (0.03)	0.21 (0.04)	1.26 (0.03)
	PME-010220	1.06 (0.10)	0.53 (0.04)	1.24 (0.04)	0.53 (0.04)	1.24 (0.04)
	PME-010620	0.97 (0.20)	0.48 (0.03)	1.24 (0.06)	0.48 (0.03)	1.24 (0.06)
	PME-021620[a]	0.62 (0.07)	0.20 (0.02)	0.87 (0.19)	0.24 (0.03)	1.00 (0.08)
	PME-022020	1.36 (0.08)	0.81 (0.05)	1.40 (0.08)	0.81 (0.05)	1.40 (0.08)
	PME-030420	1.16 (0.03)	0.58 (0.05)	1.28 (0.08)	0.58 (0.06)	1.28 (0.08)
Summer & Fall	PME-070720	1.28 (0.05)	0.76 (0.06)	1.47 (0.07)	0.76 (0.03)	1.47 (0.07)
	PME-080420	1.14 (0.07)	0.76 (0.03)	0.75 (0.02)	0.76 (0.05)	0.75 (0.02)
	PME-101520	1.03 (0.04)	1.02 (0.05)	1.15 (0.05)	1.02 (0.05)	1.15 (0.05)
Fresh wildfire	PME-081920	0.27 (0.05)	0.23 (0.01)	0.51 (0.04)	0.46 (0.05)	1.00 (0.12)
	PME-082220[a]	0.52 (0.05)	0.25 (0.02)	0.57 (0.07)	0.47 (0.05)	0.96 (0.11)
	PME-082420	1.01 (0.12)	0.31 (0.02)	0.60 (0.04)	0.31 (0.02)	0.60 (0.04)
	PME-090920	0.90 (0.47)	0.88 (0.03)	0.79 (0.03)	0.98 (0.51)	0.88 (0.52)
Aged wildfire	PME-090120	1.18 (0.12)	0.85 (0.09)	0.98 (0.04)	0.85 (0.09)	0.98 (0.04)
	PME-091520	0.95 (0.04)	0.82 (0.11)	0.87 (0.04)	0.87 (0.12)	0.92 (0.06)
	PME-100820	1.18 (0.09)	1.19 (0.15)	1.32 (0.10)	1.19 (0.15)	1.32 (0.10)
Averages						
Winter & Spring					0.49 (0.23)	1.20 (0.13)
Summer & Fall					0.85 (0.15)	1.12 (0.36)
Fresh wildfire					0.55 (0.29)	0.86 (0.18)
Aged wildfire					0.97 (0.19)	1.07 (0.22)
Field blanks						
FB1		0.95 (±0.12)	0.52 (±0.05)[b]	0.86 (±0.13)	0.54 (±0.08)[b]	0.90 (±0.19)
FB2		1.10 (±0.05)	0.95 (±0.19)	0.93 (±0.06)	0.95 (±0.19)	0.93 (±0.06)
FB3		1.21 (±0.06)	1.20 (±0.08)	1.15 (±0.09)	1.20 (±0.08)	1.15 (±0.09)

Listed uncertainties (in parentheses) are ± 1 standard error propagated from the errors in data regression, except for the averages (± 1σ)

[a] These two samples are interpolated from the winter and summer samples, respectively, in Ma et al. (2023a). *IF* values were estimated by interpolating the linear regression between 1/*IF* for each probe vs. concentration factor, to an equivalent extraction volume of 1 mL water/square.

[b] The low IF_{SYR} might be attributed to the contamination of this field blank by pH electrode filling solution.

Table S7. Oxidizing triplet excited state measurements by syringol (SYR)

Sample Type	Sample ID	k'_{SYR}[a] (10^{-4} s^{-1})	$f_{SYR,OH}$[b]	$f_{SYR,1O2*}$[c]	$f_{SYR,3C*}$[d]	$[^3C*]_{SYR,uncorr}$[e] (10^{-14} M)	$[^3C*]_{SYR}$[f] (10^{-14} M)	$k'_{3C*,SYR}$[g] (10^6 s^{-1})	$P_{3C*,SYR}$[h] (10^{-7} M s^{-1})	$\Phi_{3C*,SYR}$[i] (%)
Winter & Spring	PME-111519	11 (0.7)	0.06 (0.01)	0.15 (0.04)	0.79 (0.09)	22 (4)	79 (21)	1.9	15 (4)	6.0 (1.6)
	PME-120319	1.9 (0.1)	0.14 (0.03)	0.07 (0.02)	0.79 (0.10)	3.8 (0.8)	4.9 (1.0)	0.88	0.43 (0.09)	2.6 (0.6)
	PME-122019	5.3 (0.5)	0.15 (0.03)	0.17 (0.04)	0.69 (0.12)	9.4 (2.2)	45 (13)	1.2	5.4 (1.6)	4.6 (1.4)
	PME-010220	1.1 (0.1)	0.29 (0.06)	0.09 (0.03)	0.63 (0.11)	1.8 (0.4)	3.4 (0.9)	0.88	0.31 (0.08)	1.7 (0.4)
	PME-010620	5.4 (0.2)	0.17 (0.04)	0.15 (0.03)	0.67 (0.06)	9.3 (1.9)	19 (4)	1.2	2.3 (0.5)	2.7 (0.6)
	PME-021620[j]						35 (9)	1.4	4.7 (1.3)	2.9 (0.8)
	PME-022020	3.9 (0.2)	0.05 (0.01)	0.05 (0.01)	0.90 (0.05)	9.0 (1.7)	11 (2)	0.91	1.0 (0.2)	2.5 (0.5)
	PME-030420	0.66 (0.04)	0.44 (0.10)	0.11 (0.03)	0.45 (0.12)	0.77 (0.24)	1.3 (0.4)	0.88	0.12 (0.04)	0.9 (0.3)
Summer & Fall	PME-070720	0.91 (0.2)	0.16 (0.03)	0.07 (0.01)	0.77 (0.05)	1.8 (0.3)	2.4 (0.5)	0.85	0.20 (0.04)	4.0 (0.8)
	PME-080420	0.33 (0.03)	0.14 (0.08)	0.09 (0.04)	0.77 (0.13)	0.66 (0.15)	0.87 (0.21)	0.84	0.073 (0.017)	3.3 (0.8)
	PME-101520	0.81 (0.02)	0.08 (0.03)	0.03 (0.01)	0.89 (0.05)	1.9 (0.3)	1.9 (0.3)	0.81	0.15 (0.03)	8.5 (1.6)
Fresh wildfire	PME-081920	8.8 (0.1)	0.06 (0.01)	0.13 (0.03)	0.80 (0.04)	18.3 (3.5)	40 (9)	1.5	5.9 (1.3)	1.4 (0.3)
	PME-082220[j]						51 (12)	1.7	8.6 (2.0)	2.2 (0.5)
	PME-082420	9.2 (1.2)	0.04 (0.01)	0.12 (0.03)	0.84 (0.18)	20 (5)	64 (16)	1.4	9.0 (2.3)	3.1 (0.8)
	PME-090920	16 (4)	0.03 (0.01)	0.04 (0.01)	0.92 (0.04)	39 (7)	40 (22)	1.2	4.8 (2.6)	3.1 (1.7)
Aged wildfire	PME-090120	5.3 (0.1)	0.02 (0.01)	0.03 (0.01)	0.95 (0.04)	13 (8)	15 (3)	0.94	1.5 (0.3)	5.2 (1.1)
	PME-091520	4.8 (0.1)	0.06 (0.01)	0.04 (0.01)	0.91 (0.03)	11 (2)	13 (3)	1.0	1.3 (0.3)	3.8 (0.9)
	PME-100820	8.0 (0.3)	0.08 (0.02)	0.06 (0.01)	0.87 (0.05)	18 (3)	18 (3)	1.3	2.3 (0.4)	4.2 (0.8)
Averages[k]										
Winter & Spring							5.8 (3.7)			3.3 (1.6)
Summer & Fall							1.2 (0.78)			5.3 (2.8)
Fresh wildfire							48 (14)			2.5 (0.8)
Aged wildfire							16 (2.5)			4.4 (0.7)
Field blanks										
FB1		0.052 (±0.004)	2.20 (±1.34)	0.11 (±0.02)	-1.31 (±1.34)	-0.018 (±0.018)	-0.32 (±0.33)			
FB2		0.13 (±0.01)	0.09 (±0.02)	0.05 (±0.01)	0.86 (±0.03)	0.30 (±0.05)	0.32 (±0.08)			
FB3		0.20 (±0.01)	0.15 (±0.04)	0.05 (±0.01)	0.80 (±0.06)	0.42 (±0.08)	0.42 (±0.08)			

Listed uncertainties (in parentheses) are ± 1 standard error propagated from the errors in the regression and rate constants, except for the averages, which are ± 1σ. Values in the table are not normalized by the sampling duration, but the average triplet concentrations are calculated using 7-day concentrations normalized to 1-day equivalent values.

[a] Davis winter-solstice-normalized pseudo-first-order rate constant for loss of syringol (SYR)

[b] Fraction of SYR loss due to hydroxyl radical, calculated as $f_{SYR,OH} = (k_{SYR+OH} \times [^{\bullet}OH])/k'_{SYR}$

[c] Fraction of SYR loss due to singlet oxygen, calculated as $f_{SYR,1O2*} = (k_{SYR+1O2*} \times [^1O_2*])/k'_{SYR}$.

[d] Fraction of SYR loss due to triplets, calculated as $f_{SYR,3C*} = (1 - f_{SYR,OH} - f_{SYR,1O2*})$.

[e] Uncorrected triplet steady-state concentration calculated from syringol loss as $k'_{SYR,3C*}/k_{SYR+3DMB*}$.

[f] Triplet concentration after correction for SYR inhibition, calculated as $[^3C*]_{SYR,uncorr}/IF_{SYR,corr}$.

[g] First-order rate constant for loss of SYR-determined oxidizing $^3C*$ due to DOC and dissolved oxygen. This is calculated as $k'_{3C*,SYR} = k_{rxn+Q,3C*}[DOC] + k_{3C*+O2}[O_2]$, where $k_{rxn+Q,3C*}$ is estimated from the fitting between $[^3C*]_{SYR}$ and DOC using samples from this work and Ma et al. (2023a) using the equation $[^3C^*]_{SYR} = \frac{a[DOC]}{1+b[DOC]}$ (Kaur et al., 2019). The resulting $k_{rxn+Q,3C*}$ value is 7.2 (± 2.2) × 10^7 L (mol-C)$^{-1}$ s^{-1}, while k_{3C*+O2} is 2.8 (± 0.4) × 10^9 L (mol C)$^{-1}$ s^{-1} from Kaur et al. (2019).

[h] Production rate of oxidizing triplets determined by SYR, calculated as $P_{3C*,SYR} = [^3C*]_{SYR} \times k'_{3C*,SYR}$.

[i] Apparent quantum yield of $^3C*$ determined by SYR during simulated sunlight illumination, calculated as $\Phi_{3C*,SYR} = P_{3C*,SYR}/R_{abs.}$

[j] These two samples are the interpolated winter and summer samples, respectively, from our previous work (Ma et al., 2023a). $^3C^*$ concentrations were estimated at an extraction volume of 1 mL water/square by interpolating the hyperbolic regression between $[^3C^*]$ and concentration factor.

[k] Average value of each sample type. The $^3C^*$ concentration normalized by sampling duration was used for the average $[^3C*]_{SYR}$ calculation.

Table S8. Oxidizing triplet excited state measurements by (phenylthio)acetic acid (PTA)

Sample Type	Sample ID	k'_{PTA}[a] (10^{-4} s^{-1})	$f_{PTA,OH}$[b]	$f_{PTA,1O2*}$[c]	$f_{PTA,3C*}$[d]	$[^3C^*]_{PTA,uncorr}$[e] (10^{-14} M)	$[^3C^*]_{PTA}$[f] (10^{-14} M)	$k'_{3C*,PTA}$[g] (10^6 s^{-1})	$P_{3C*,PTA}$[h] (10^{-7} M s^{-1})	$\Phi_{3C*,PTA}$[i] (%)	$[^3C^*]_{PTA}/[^3C^*]_{SYR}$[j]
Winter & Spring	PME-111519	12 (1)	0.03 (0.01)	0.03 (0.01)	0.94 (0.06)	44 (11)	44 (11)	2.0	8.5 (2.1)	3.4 (0.8)	0.55 (0.20)
	PME-120319	1.1 (0.1)	0.12 (0.01)	0.03 (0.01)	0.85 (0.02)	3.6 (0.9)	3.6 (0.9)	0.88	0.32 (0.08)	2.0 (0.5)	0.75 (0.24)
	PME-122019	5.7 (0.1)	0.07 (0.01)	0.04 (0.01)	0.89 (0.01)	20 (5)	20 (5)	1.2	2.4 (0.6)	2.1 (0.5)	0.45 (0.17)
	PME-010220	1.2 (0.1)	0.14 (0.01)	0.02 (0.01)	0.84 (0.02)	4.0 (1.0)	4.0 (1.0)	0.89	0.35 (0.08)	1.9 (0.5)	1.2 (0.4)
	PME-010620	5.9 (0.1)	0.08 (0.01)	0.03 (0.01)	0.89 (0.03)	21 (5)	21 (5)	1.2	2.5 (0.6)	2.9 (0.7)	1.1 (0.4)
	PME-021620[k]						22 (6)	1.4	3.0 (0.8)	1.9 (0.5)	0.64 (0.24)
	PME-022020	1.6 (0.1)	0.06 (0.02)	0.03 (0.01)	0.90 (0.08)	5.7 (1.4)	5.7 (1.4)	0.91	0.52 (0.13)	1.3 (0.3)	0.51 (0.16)
	PME-030420	0.74 (0.06)	0.20 (0.02)	0.02 (0.01)	0.77 (0.07)	2.3 (0.6)	2.3 (0.6)	0.88	0.20 (0.05)	1.5 (0.4)	1.7 (0.7)
Summer & Fall	PME-070720	0.31 (0.01)	0.25 (0.02)	0.05 (0.01)	0.70 (0.04)	0.85 (0.21)	0.85 (0.21)	0.86	0.073 (0.018)	1.4 (0.4)	0.36 (0.11)
	PME-080420	0.084 (0.014)	0.28 (0.15)	0.08 (0.03)	0.64 (0.25)	0.21 (0.09)	0.28 (0.12)	0.84	0.024 (0.010)	1.1 (0.5)	0.33 (0.16)
	PME-101520	0.17 (0.02)	0.21 (0.08)	0.03 (0.01)	0.76 (0.14)	0.52 (0.15)	0.52 (0.15)	0.81	0.042 (0.012)	2.4 (0.7)	0.28 (0.10)
Fresh wildfire	PME-081920	5.2 (0.1)	0.05 (0.01)	0.06 (0.01)	0.89 (0.03)	18 (4)	18 (4)	1.5	2.8 (0.8)	0.64 (0.17)	0.46 (0.16)
	PME-082220[k]						19 (5)	1.7	3.2 (0.9)	0.84 (0.23)	0.37 (0.13)
	PME-082420	3.0 (0.2)	0.07 (0.02)	0.09 (0.01)	0.84 (0.07)	10 (3)	17 (4)	1.4	2.4 (0.6)	0.85 (0.22)	0.27 (0.10)
	PME-090920	4.6 (0.1)	0.06 (0.01)	0.04 (0.01)	0.90 (0.04)	17 (4)	19 (12)	1.2	2.3 (1.5)	1.5 (1.0)	0.48 (0.41)
Aged wildfire	PME-090120	1.4 (0.1)	0.04 (0.01)	0.03 (0.01)	0.94 (0.03)	5.1 (1.2)	5.2 (1.3)	0.94	0.49 (0.12)	1.8 (0.4)	0.34 (0.11)
	PME-091520	1.5 (0.1)	0.10 (0.01)	0.03 (0.01)	0.87 (0.04)	5.1 (1.2)	5.5 (1.4)	1.0	0.56 (0.14)	1.6 (0.4)	0.42 (0.14)
	PME-100820	2.1 (0.1)	0.16 (0.01)	0.05 (0.01)	0.79 (0.03)	6.5 (1.6)	6.5 (1.6)	1.3	0.83 (0.20)	1.5 (0.4)	0.36 (0.11)
Averages[m]											
Winter & Spring							3.9 (1.4)			2.1 (0.7)	0.86 (0.43)
Summer & Fall							0.57 (0.29)			1.6 (0.7)	0.32 (0.04)
Fresh wildfire							18 (0.16)			0.96 (0.39)	0.39 (0.10)
Aged wildfire							5.7 (0.7)			1.6 (0.1)	0.37 (0.05)
Field blanks											
FB1[l]		4.6 (±0.6)	0.01 (±0.01)	0.00 (±0.01)	0.99 (±0.14)	18.1 (±5.0)	20.1 (±7.0)				
FB2		0.028 (±0.009)	0.22 (±0.03)	0.07 (±0.01)	0.71 (±0.32)	0.078 (±0.040)	0.084 (±0.043)				
FB3		0.051 (±0.019)	0.31 (±0.04)	0.05 (±0.01)	0.64 (±0.38)	0.13 (±0.08)	0.13 (±0.08)				

Listed uncertainties (in parentheses) are ± 1 standard error propagated from the errors in the regression and rate constants, except for the averages, which are ± 1σ. Values in the table are not normalized by the sampling duration, but the average triplet concentration was calculated using 7-day concentrations normalized to 1-day equivalent values.

[a] Davis winter-solstice-normalized value of the measured pseudo-first-order rate constant for loss of PTA. Contribution from PTA direct photodegradation was subtracted. The PTA direct photodegradation accounted for (0.9-55) % of PTA total decay in PME samples, with an average of 11 (± 15) % and for (2-79) % of PTA total decay in field blanks.

[b] Fraction of hydroxyl radical contribution to the loss of PTA, calculated as $f_{PTA,OH} = (k_{PTA+OH} \times [^{\bullet}OH])/k'_{PTA}$

[c] Fraction of singlet oxygen contribution to the loss of PTA, calculated as $f_{PTA,1O2^*} = (k_{PTA+1O2^*} \times [^1O_2{}^*])/k'_{PTA}$.

[d] Fraction of PTA loss due to triplets, calculated as $f_{PTA,3C^*} = (1 - f_{PTA,OH} - f_{PTA,1O2^*})$.

[e] Uncorrected triplet steady-state concentration calculated from PTA loss as $k'_{PTA,3C^*}/k_{PTA+3DMB^*}$.

[f] Triplet concentration with inhibition factor correction, calculated as $[^3C^*]_{PTA,uncorr}/IF_{PTA,corr}$.

[g] Apparent pseudo-first-order rate constant for quenching PTA-determined $^3C^*$ by organic sinks and dissolved oxygen, calculated as $k'_{3C^*,PTA} = k_{rxn+Q,3C^*}[DOC] + k_{3C^*+O2}[O_2]$, where $k_{rxn+Q,3C^*}$ is estimated from the fitting between $[^3C^*]_{PTA}$ and DOC using samples from this work and Ma et al. (2023a) using an equation of $[^3C^*]_{PTA} = \frac{a[DOC]}{1+b[DOC]}$ (Kaur et al., 2019). The corresponding value for $k_{rxn+Q,3C^*}$ is 7.4 (± 2.5) × 10^7 L (mol C)$^{-1}$ s^{-1}, while k_{3C^*+O2} = 2.8 (± 0.4) × 10^9 L (mol-C)$^{-1}$ s^{-1} from Kaur et al. (Kaur et al., 2019).

[h] Production rate of triplet determined by PTA, calculated as $P_{3C^*,PTA} = [^3C^*]_{PTA} \times k'_{3C^*,PTA}$.

[i] Apparent quantum yield of $^3C^*$ determined by PTA during simulated sunlight illumination, calculated as $\Phi_{3C^*,PTA} = P_{3C^*,PTA}/R_{abs}$.

[j] Ratio of triplet concentration determined by PTA to that determined by SYR.

[k] These two samples are the interpolations of the winter and summer samples, respectively, from our previous work (Ma et al., 2023a). $^3C^*$ concentrations were estimated by interpolating the hyperbolic regression between $[^3C^*]_{PTA}$ and concentration factor, to an equivalent extraction volume of 1 mL water/square.

[l] This field blank sample was contaminated by a pH electrode and possibly other unknown sources, leading to fast decay of PTA.

[m] Average value of each sample type. The $^3C^*$ concentration normalized by sampling duration was used in the calculation of average $[^3C^*]_{PTA}$.

Section S2. Satellite images and back trajectories for wildfire samples

The figures below show satellite images of Northern California with fire points detected by the NASA Visible Infrared Imaging Radiometer Suite (VIIRS) for seven wildfire particle samples on the day of collection. The bottom panel of each figure is a 24-h back trajectory that ends at the Davis sampling site at the middle of the sample period. Back trajectories were estimated by the Hybrid Single Particle Lagrangian Integrated Trajectory (HYSPLIT) model at heights of 20, 600, and 1200 m above the ground (Rolph et al., 2017; Stein et al., 2015).

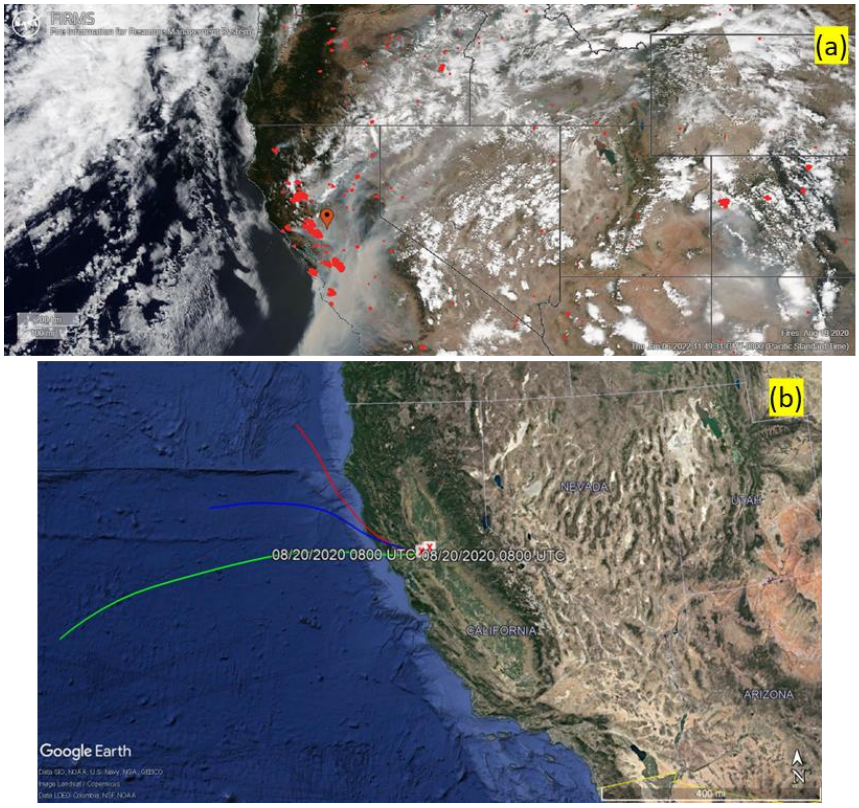

Figure S3. (a) Satellite image on 19 August 2020, with fires detected by VIIRS labeled by red dots. The location symbol represents Davis CA. (b) 24-hr back trajectories from the sampling site at a height of 20 m (red), 600 m (blue), and 1200 m (green) above the ground. It took approximately 1-2 h for the smoke plume from the Lake Berryessa area west of Davis to be transported to the sampling site.

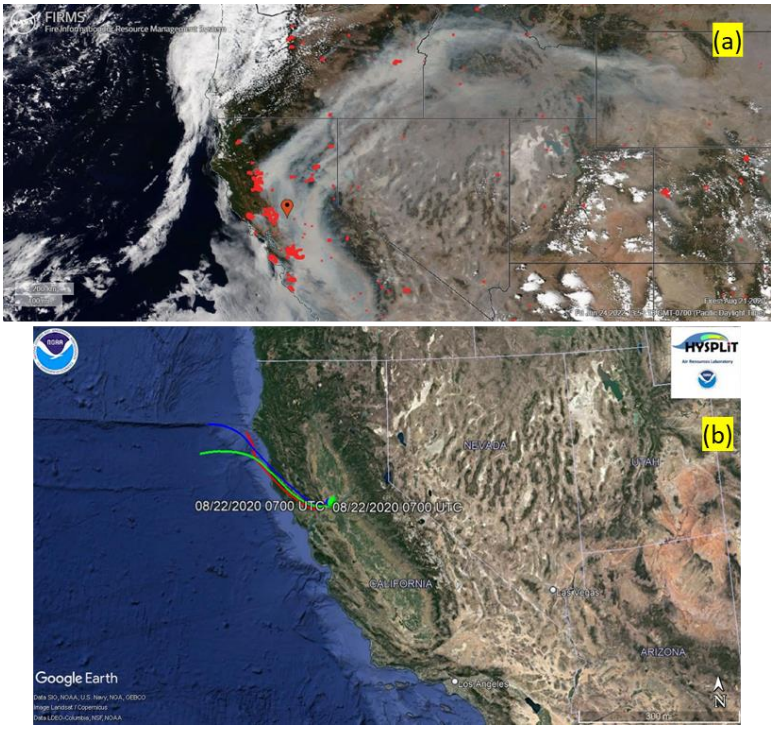

Figure S4. (a) Satellite image on 22 August 2020, with fires detected by VIIRS labeled by red dots. The location symbol represents Davis CA. (b) 24 hr back trajectories ending at the sampling site at heights of 20 m (red), 600 m (blue), and 1200 m (green) above the ground. It took approximately 1-2 h for the smoke plume from the Lake Berryessa area west of Davis to be transported to the sampling site.

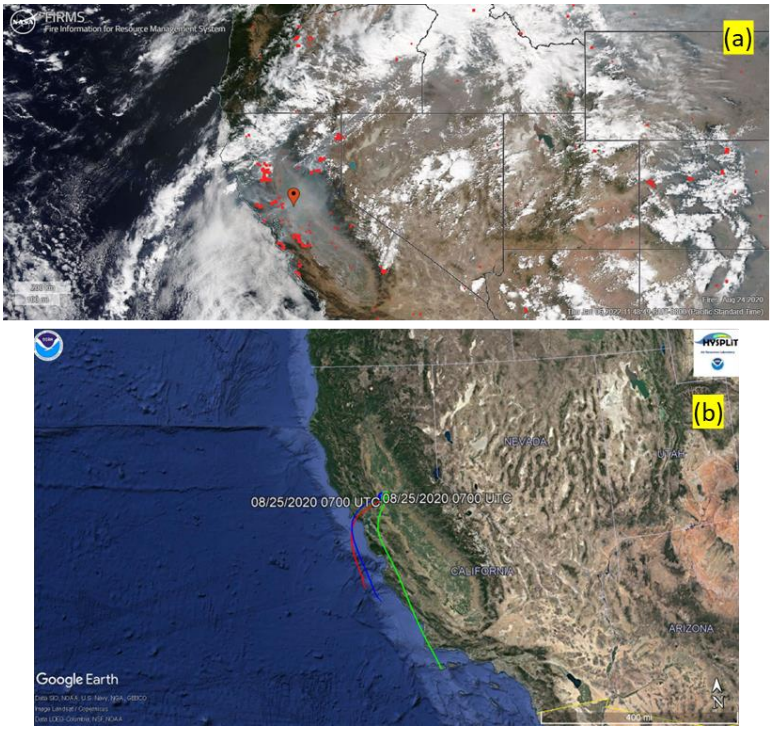

Figure S5. (a) Satellite image on 24 August 2020, with fires detected by VIIRS labeled by red dots. The location symbol represents Davis CA. (b) 24 hr-back trajectories ending at the sampling site at heights of 20 m (red), 600 m (blue), and 1200 m (green) above the ground.

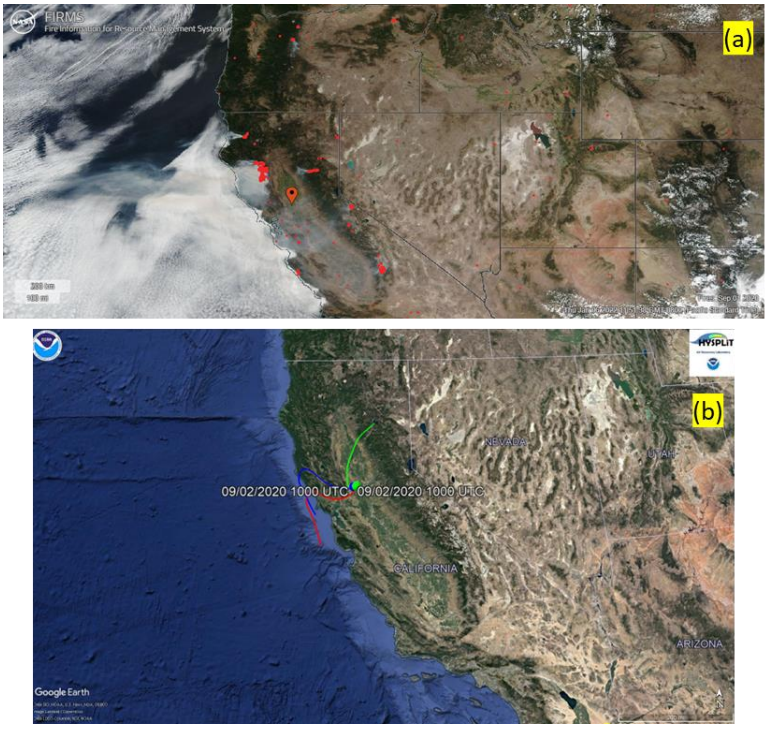

Figure S6. (a) Satellite image on 1 September 2020, with fires detected by VIIRS labeled by red dots. The location symbol represents Davis CA. (b) 24-hr back trajectories ending at the sampling site at heights of 20 m (red), 600 m (blue), and 1200 m (green) above the ground. Wildfire plumes from the Mendocino National Forest and Chico area took approximately 9 -12 h to transport to Davis.

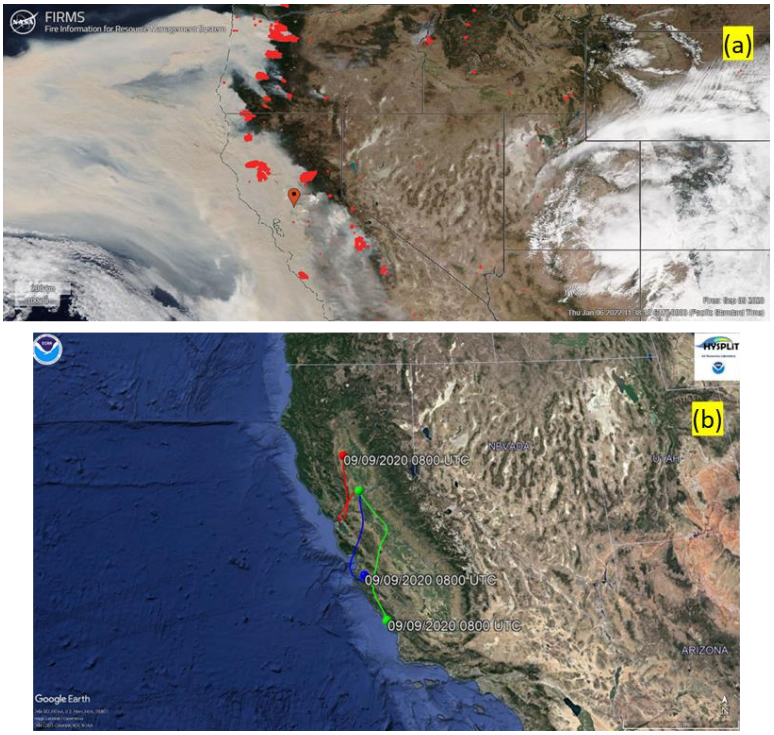

Figure S7. (a) Satellite image on 9 September 2020, with fires detected by VIIRS labeled by red dots. The location symbol represents Davis CA. (b) 24-hr back trajectories ending at the sampling site at heights of 20 m (red), 600 m (blue), and 1200 m (green) above the ground. Wildfire plumes from the Mendocino National Forest, the Chico area, and Oregon required approximately 7 to 24 h to transport to Davis during this time.

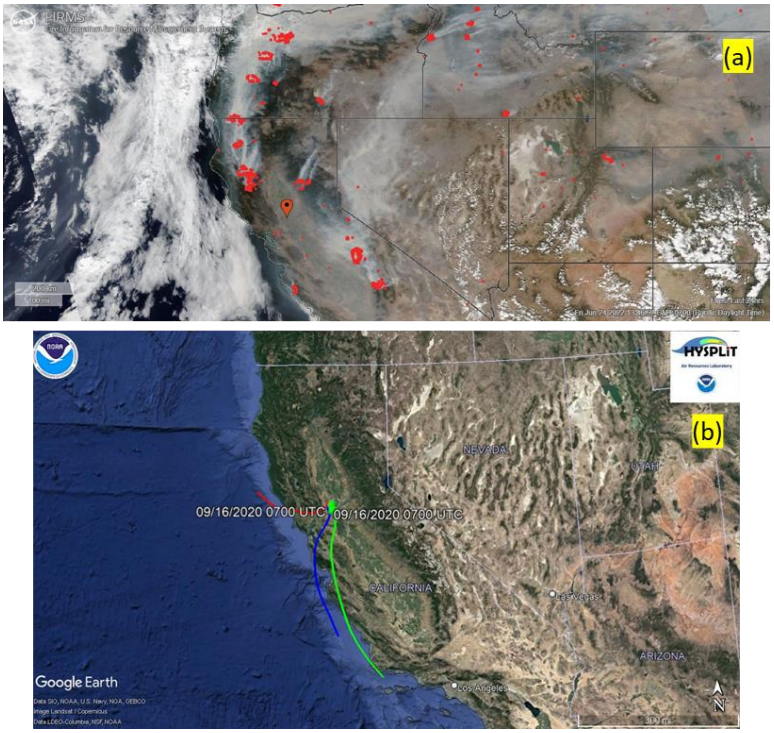

Figure S8. (a) Satellite image on 15 September 2020, with fires detected by VIIRS labeled by red dots. The location symbol represents Davis CA. (b) 24-hr back trajectories ending at the sampling site at heights of 20 m (red), 600 m (blue), and 1200 m (green) above the ground. Because the back trajectories do not pass through the burning regions it is difficult to estimate a plume aging time.

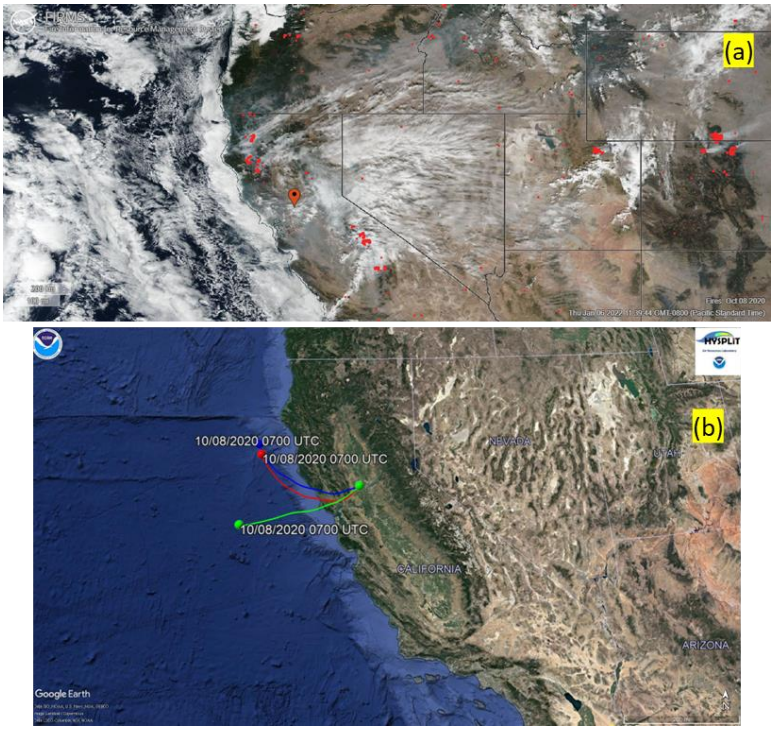

Figure S9. (a) Satellite image on 10 October 2020, with fire points detected by VIIRS labeled by red dots. The location symbol represents Davis CA. (b) 24-hr back trajectories ending at the sampling site at heights of 20 m (red), 600 m (blue), and 1200 m (green) above the ground. The back trajectories appeared not to pass through the burning areas directly, making it difficult to estimate the aging time.

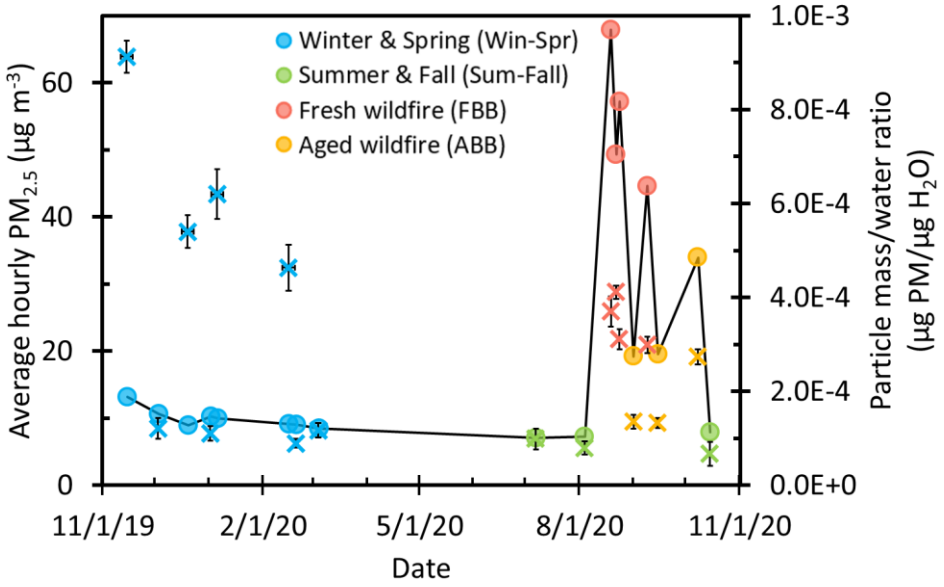

Figure S10. Average $PM_{2.5}$ concentration during sampling period (circles) from a regulatory monitor during each sampling period and measured particle mass/water mass ratios (crosses) from filter extracts for each sample. Vertical error bars represent ±1 standard deviation, while horizontal error bars represent the duration of sampling (either 1 or 7 days).

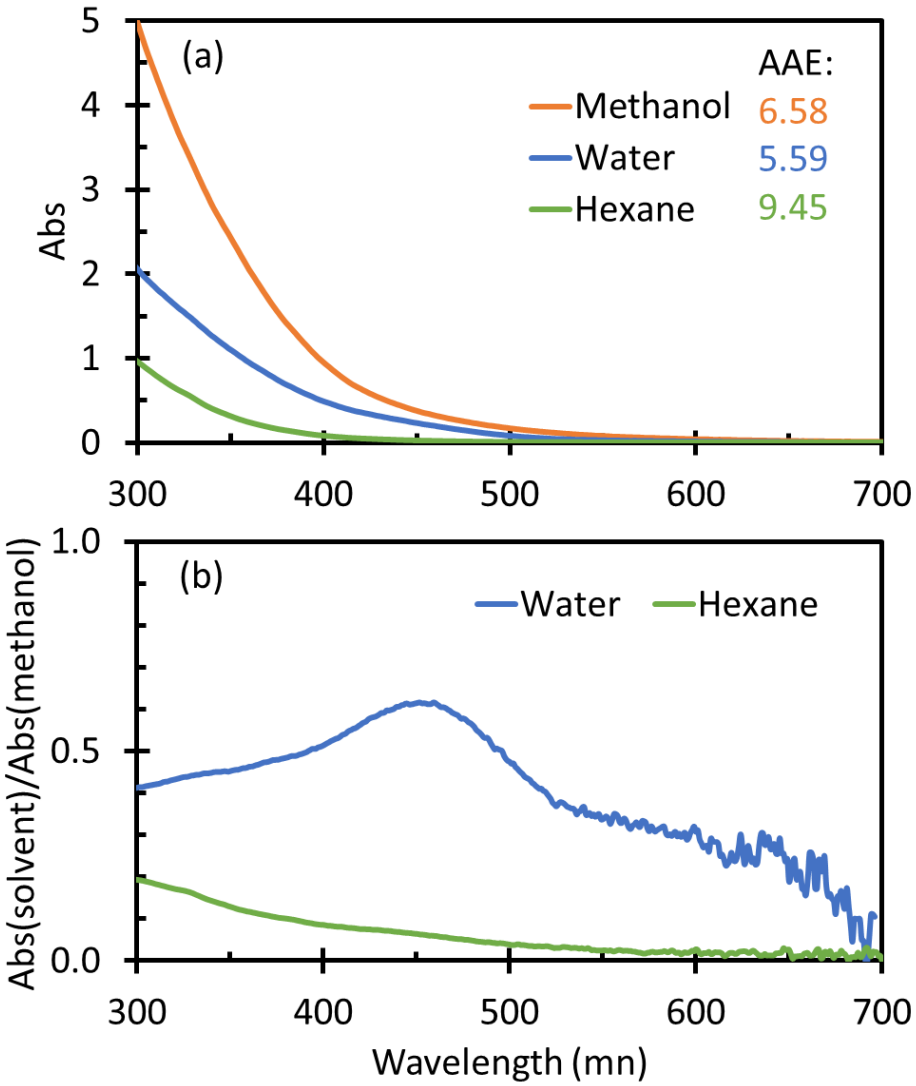

Figure S11. (a) UV-Vis spectra of different solvent extracts of the particle sample collected on 8/19/2020. Each line represents the absorbance spectrum for a square of filter that was extracted in the listed solvent then filtered. AAE values were determined for each spectrum based on absorbance over 300 to 450 nm. Spectra were measured in 1-cm cuvettes. (b) Ratio of the absorbance in the water (blue) and hexane (green) extracts to the absorbance of the methanol extract.

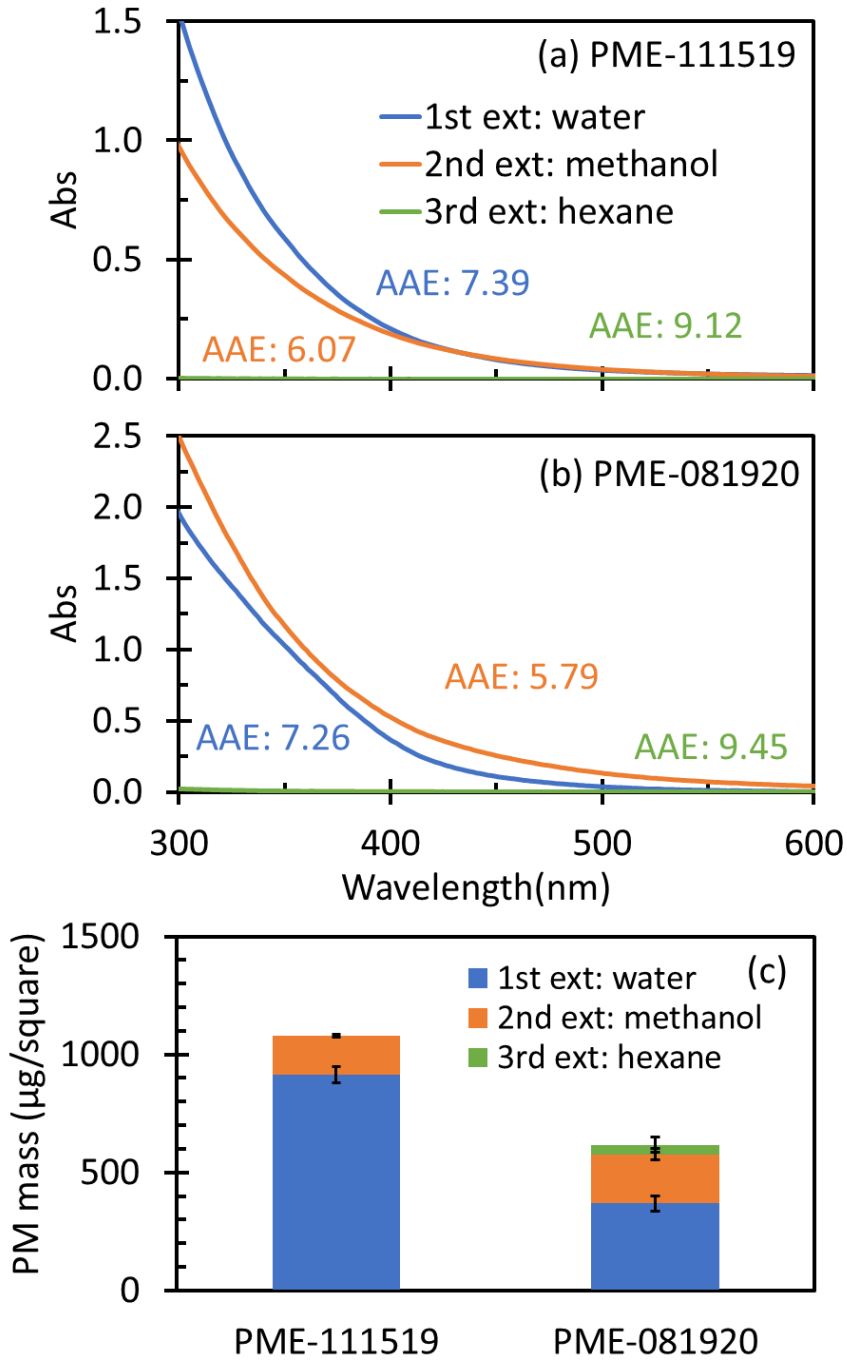

Figure S12. UV-Vis spectra for sequential extracts of a given filter square, each with 1.0 mL of the solvent listed, as measured in a 1-cm cuvette. The blue line or bar represents the first extraction, which was with water; the orange line or bar represents the second extraction, which was in methanol, and the green line or bar represents the third extraction, which was done with hexane. Panel (a) shows results for sample PME-111519, while panel (b) is for PME-081920. Panel (c) shows the particle mass extracted per filter square in the sequential extraction sequence with water, methanol, and hexane. The particle mass extracted by hexane in PME-111519 was not measured.

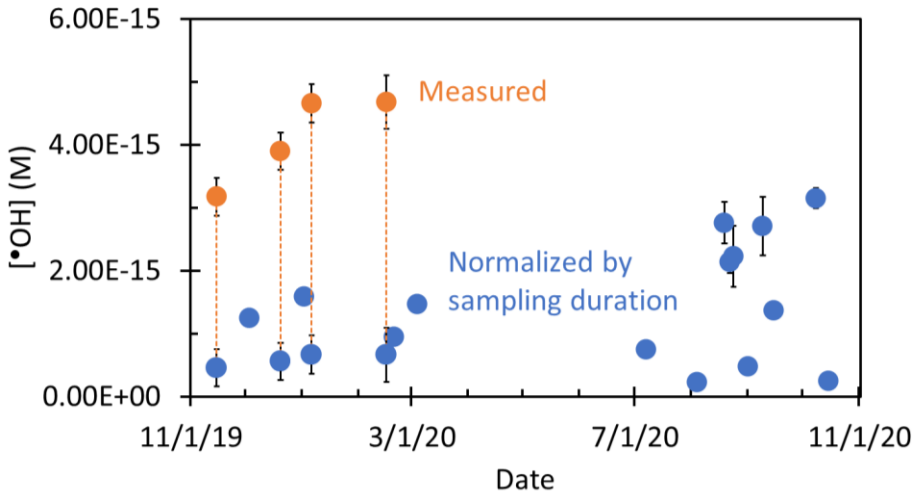

Figure S13. Comparison between measured •OH concentrations (orange) and values normalized by sampling duration in four 7-day samples (blue). Figure 4 shows the •OH data normalized by PM mass/water mass ratio, which was what we used as the standard normalization for these 7-day samples.

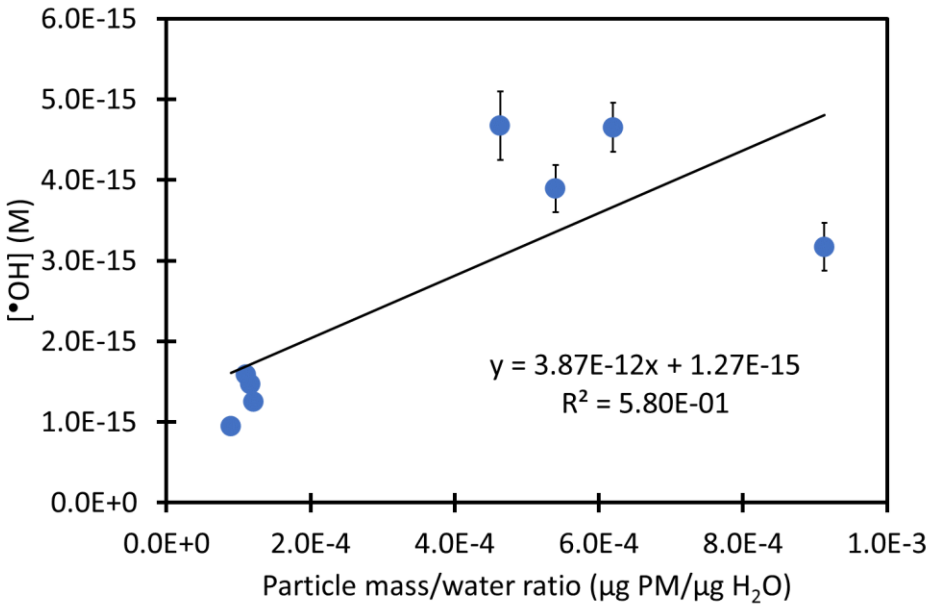

Figure S14. Dependence of hydroxyl radical concentration on particle mass/water mass ratio for Winter & Spring samples. The line represents the linear regression.

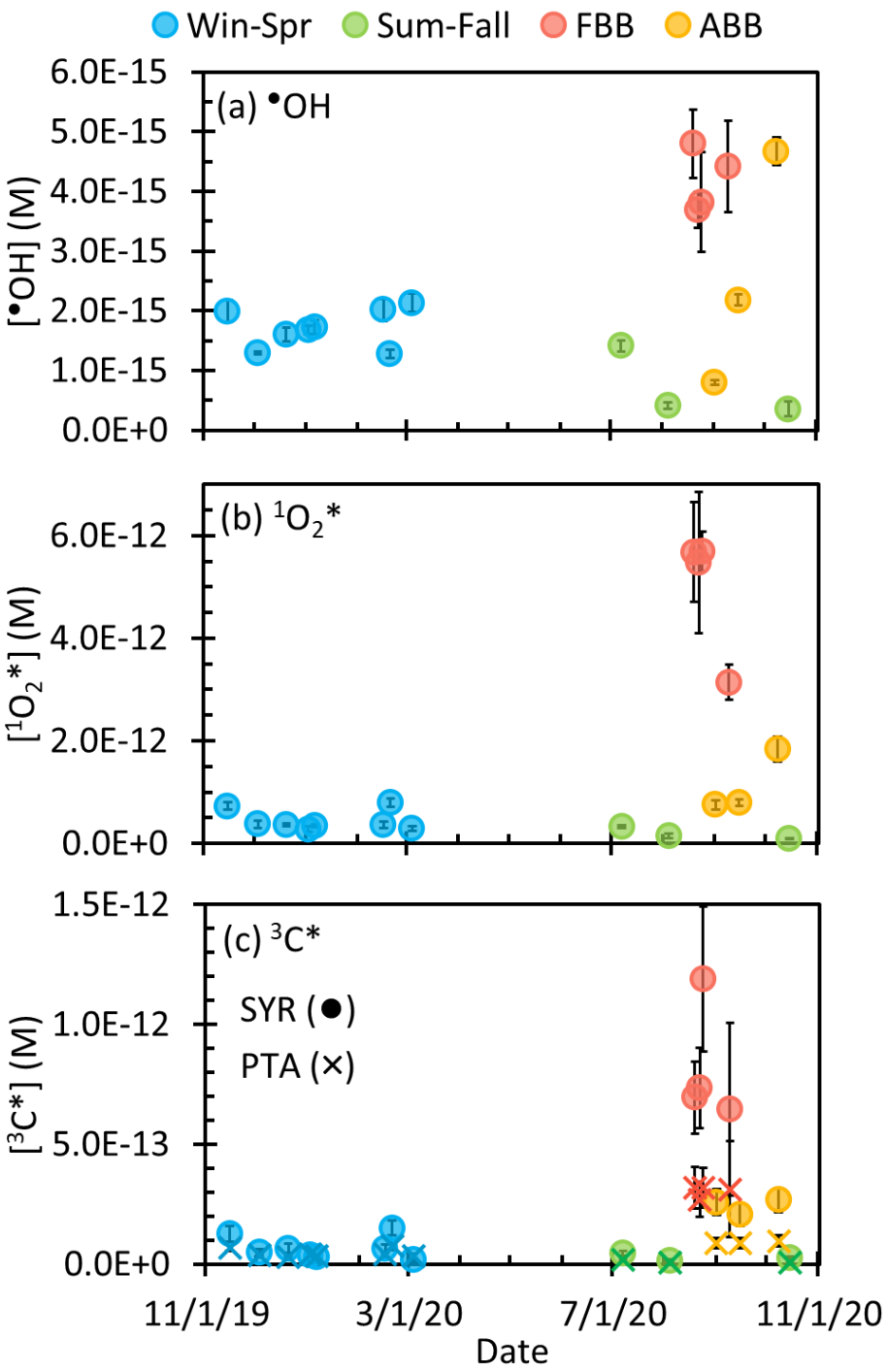

Figure S15. Steady-state concentrations of (a) hydroxyl radical, (b) singlet molecular oxygen, and (c) oxidizing triplet excited states of light-absorbing organics determined by syringol (SYR, circles) and (phenylthio)acetic acid (PTA, crosses) in particle extracts. Concentrations are normalized to the midday sunlight of each sampling period to account for the seasonal differences in actinic flux. Seven-day samples were normalized to the expected one-day result as described in section 3.3.1 and Table S9. The equivalent plots with concentrations all normalized to the same midday winter solstice sunlight in Davis are shown in Figure 4.

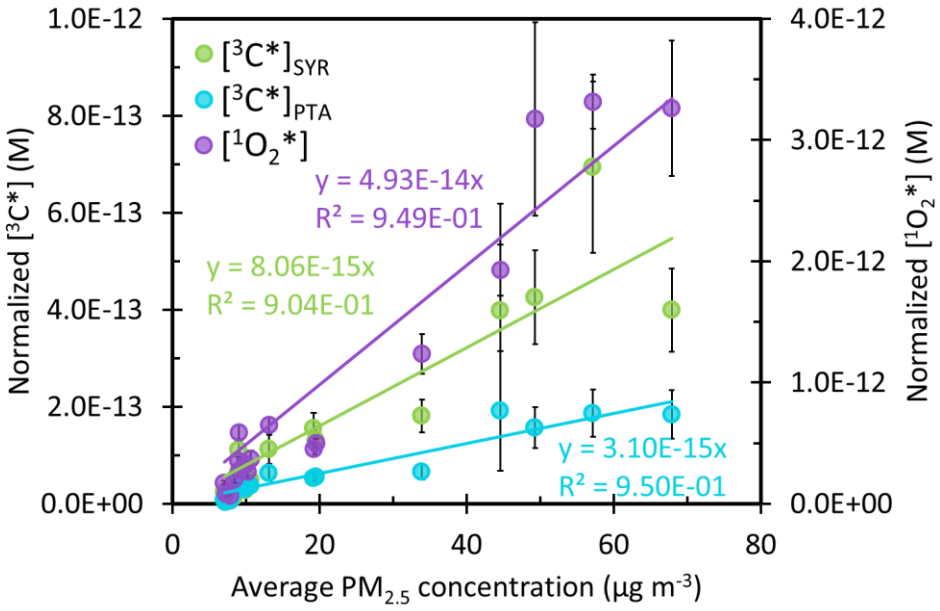

Figure S16. Normalized singlet oxygen (purple, right *y*-axis) and triplet excited state of organic matter determined by syringol (green) and (phenylthio)acetic acid (blue) as a function of average $PM_{2.5}$ concentration. Solid lines are linear regressions with the *y*-intercepts fixed at zero.

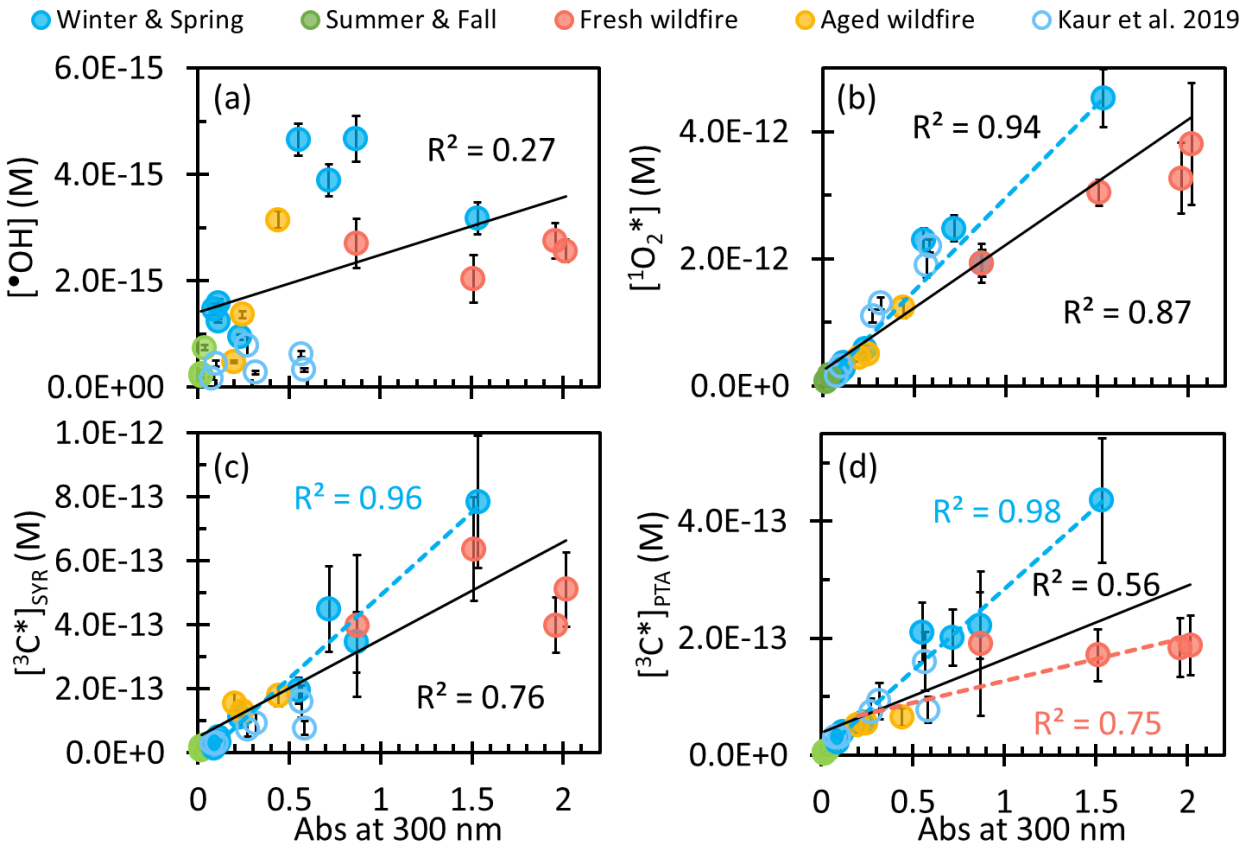

Figure S17. Steady-state concentrations of (a) hydroxyl radical, (b) singlet molecular, and oxidizing triplet excited states of organic matter determined by (c) syringol and (d) (phenylthio)acetic acid as a function of absorbance at 300 nm for each sample type (solid circles). Previous measurements made on Davis winter particle extracts are shown by open blue circles (Kaur et al., 2019). Solid lines are linear regressions between oxidant concentrations of all samples in this work and extract absorbance in a 1-cm cell. Blue dashed lines are the linear regressions of our Win-Spr samples, while the red dashed line is a regression of the FBB and ABB samples.

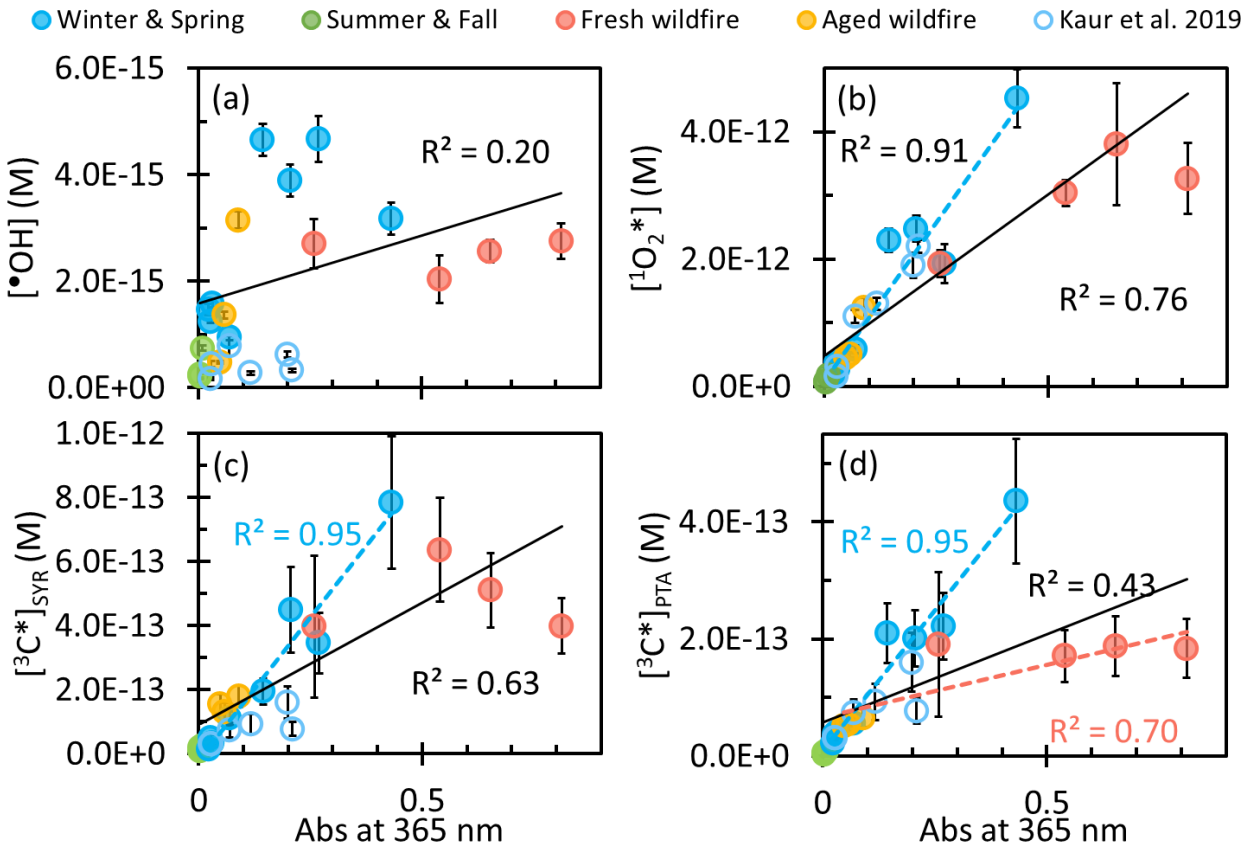

Figure S18. Steady-state concentrations of (a) hydroxyl radical, (b) singlet molecular, and oxidizing triplet excited state of organic matter determined by (c) syringol and (d) (phenylthio)acetic acid as a function of absorbance (in a 1 cm cell) at 365 nm for each sample type (solid circles). Previous measurements made in Davis winter particle extracts are included (open circles) (Kaur et al., 2019). Solid lines are linear regressions between oxidant concentration and absorbance for all samples in our current work. Blue dashed lines are the linear regressions of current Win-Spr samples, while the red dashed line is the regression of the combined FBB and ABB samples.

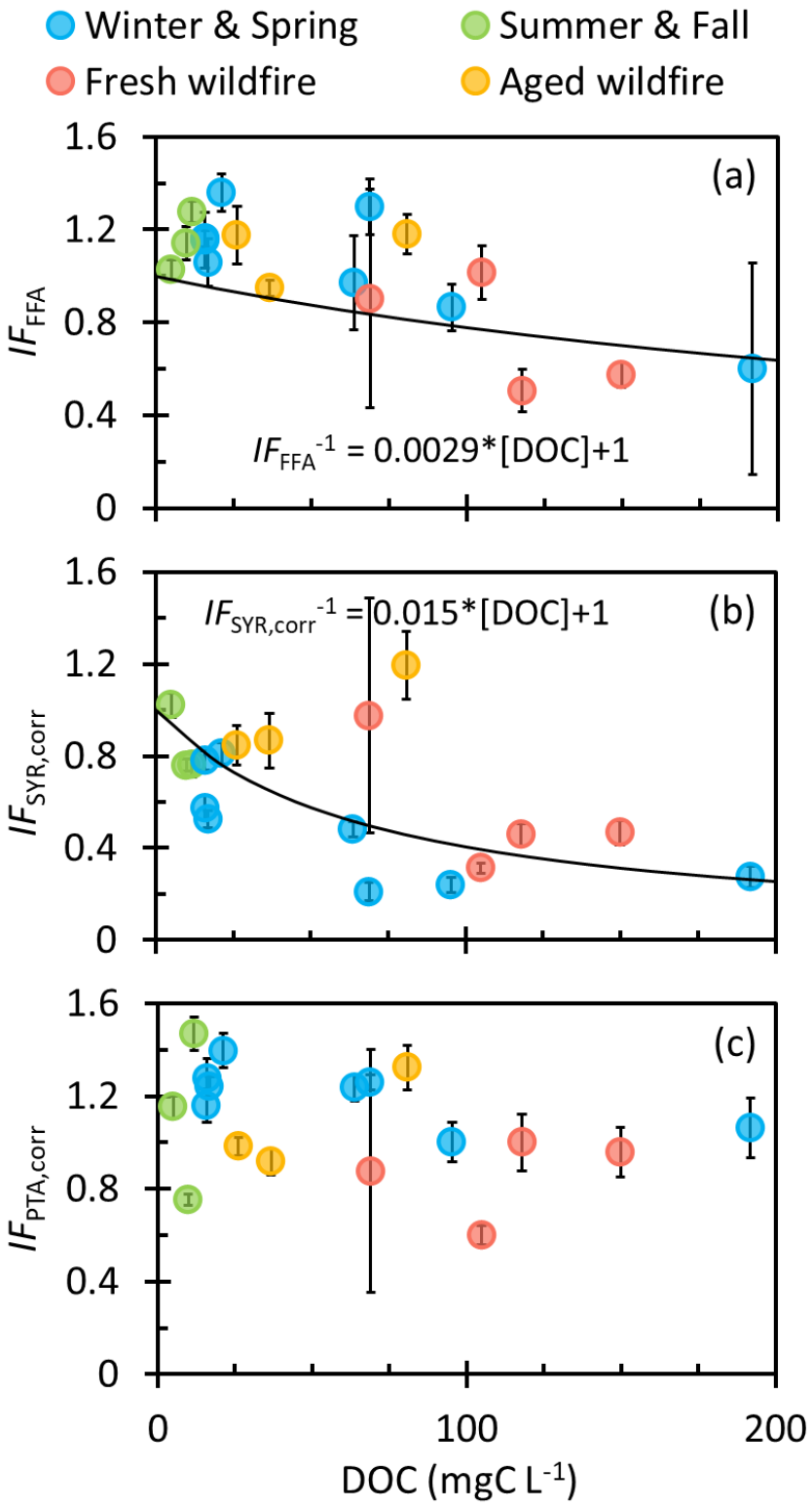

Figure S19. Inhibition factor of (a) furfuryl alcohol, and corrected inhibition factors of (b) syringol and (c) (phenylthio)acetic acid as a function of dissolved organic carbon. Solid lines represent linear regressions of IF_P^{-1} = a[DOC] + b (Ma et al., 2023b; Wenk et al., 2011).

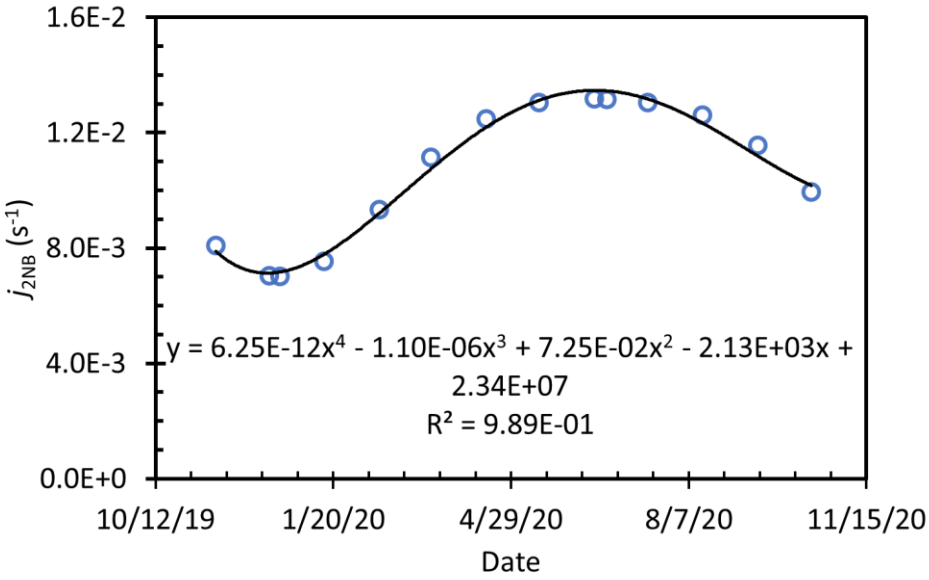

Figure S20. Estimated midday j_{2NB} values as a function of date based on TUV actinic fluxes (points) and the corresponding 4th-order polynomial fit (solid line). Details about the estimation of j_{2NB} values are provided in Section S3.

Section S3. Seasonal variation of j_{2NB}

We obtained the modeled actinic flux (photons s^{-1} nm^{-1} cm^{-2}) on the midday of the15th of each month in Davis CA (38.545 ° N, 121.741 ° W) from November 2019 to October 2020 from the Tropospheric Ultraviolet and Visible (TUV) Radiation Model version 5.3 (https://www.acom.ucar.edu/Models/TUV/Interactive_TUV/, last access: 7 August 2022). For the TUV model runs, other input parameters like ozone column and aerosols were set at default values:

Ozone column: 300 du

Surface albedo: 0.1

Ground elevation & Measurement altitude: 0 km asl

Aerosols: Option depth: 0.235; S-S Alb: 0.990; Alpha: 1.000.

j_{2NB} values for each date were calculated using (Galbavy et al., 2010):

$$j_{2NB} = 2.303 \times (10^3\ cm^3 L^{-1} \div N_A) \times \sum (I'_\lambda \times \Delta\lambda \times \varepsilon_{2NB,\lambda} \times \Phi_{2NB,\lambda})$$

where N_A is Avogadro's number, I'_λ is the actinic flux (photons s^{-1} nm^{-1} cm^{-2}), $\Delta\lambda$ is the wavelength interval between actinic flux data points (1 nm here), ε_{2NB} is the base-10 molar absorption coefficient of 2-nitrobenzaldehyde (M^{-1} cm^{-1}) (Galbavy et al., 2010), and Φ_{2NB} is the 2NB quantum yield (0.41 molecule $photon^{-1}$, independent of wavelength (Galbavy et al., 2010)). From our calculations, j_{2NB} on the midday of the winter solstice is 0.0053 s^{-1}, which is lower than the value (0.0070 s^{-1}) measured in Davis on this day

(Anastasio and McGregor, 2001). To approximately compensate for the difference between the measured and modeled values, we added 0.0017 s^{-1} to each calculated j_{2NB} value and plotted them as a function of date (Figure S19). We then fitted the data with a 4th-order polynomial with Excel dates as x values, and use this regression to calculate j_{2NB} on each day of sampling. The calculated j_{2NB} values are in Table S9.

Table S9. Calculated j_{2NB} values for each sample

Sample Type	Sample ID	j_{2NB} (s^{-1})[a]
Winter & Spring	PME-111519	0.0079
	PME-120319	0.0072
	PME-122019	0.0072
	PME-010220	0.0074
	PME-010620	0.0075
	PME-021620	0.0093
	PME-022020	0.0095
	PME-030420	0.010
Summer & Fall	PME-070720	0.013
	PME-080420	0.013
	PME-101520	0.010
Fresh wildfire	PME-081920	0.012
	PME-082220	0.012
	PME-082420	0.012
	PME-090920	0.011
Aged wildfire	PME-090120	0.012
	PME-091520	0.011
	PME-100820	0.010
Averages		
Winter & Spring		0.0083
Summer & Fall		0.012
Fresh wildfire		0.012
Aged wildfire		0.011

[a] Values are calculated for midday on the middle day of each sampling period in Davis; see Section S3.

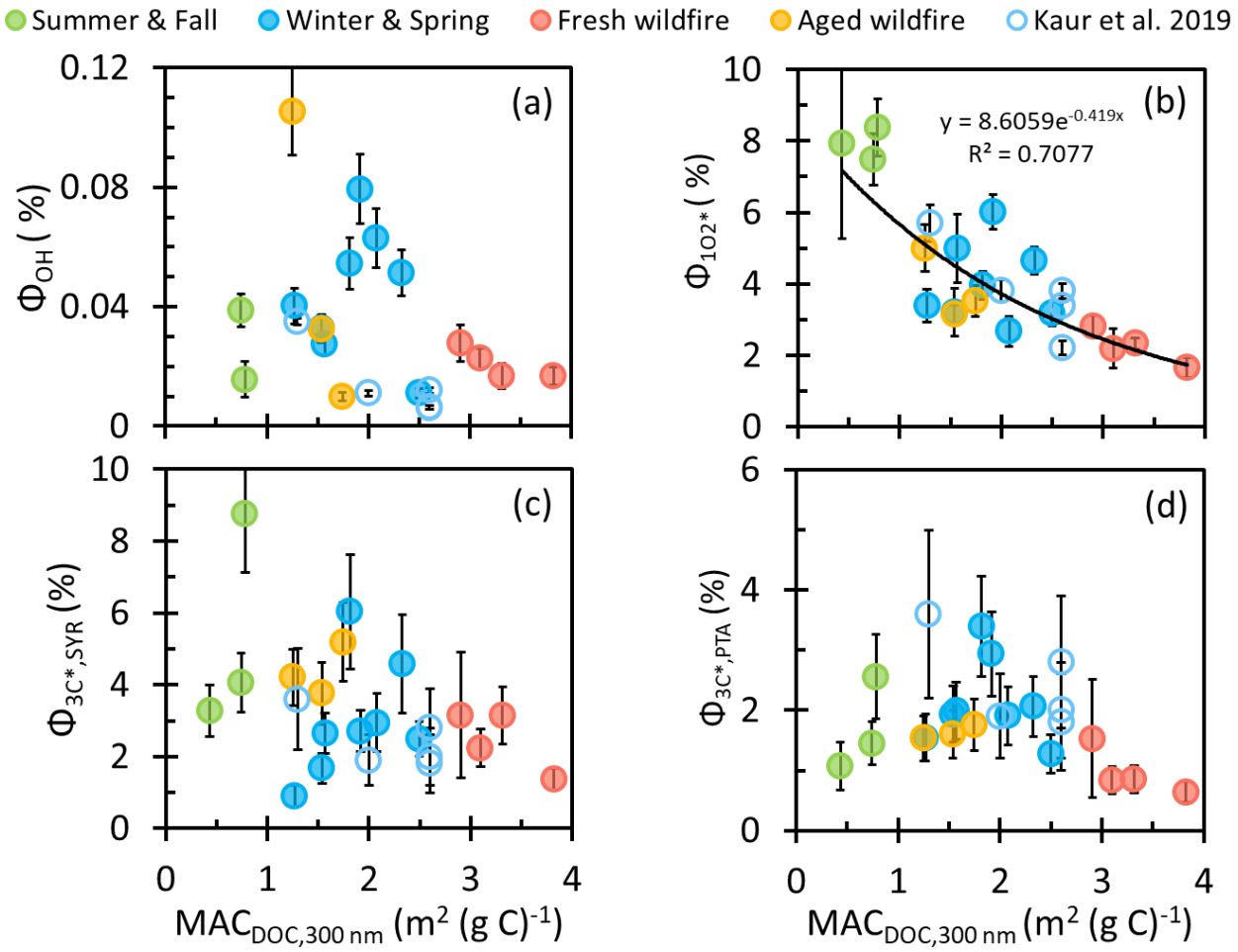

Figure S21. Apparent quantum yields of (a) hydroxyl radical, (b) singlet molecular oxygen, and oxidizing triplet excited states of organic matter determined by (c) syringol and (d) (phenylthio)acetic acid as a function of DOC-normalized mass absorption coefficient at 300 nm (solid circles). Previous measurements made in Davis winter particle extracts are shown in blue open circles (Kaur et al., 2019). The solid black line represents an exponential regression to all of the $^1O_2$* data in this work, not including data from Kaur et al. (2019).

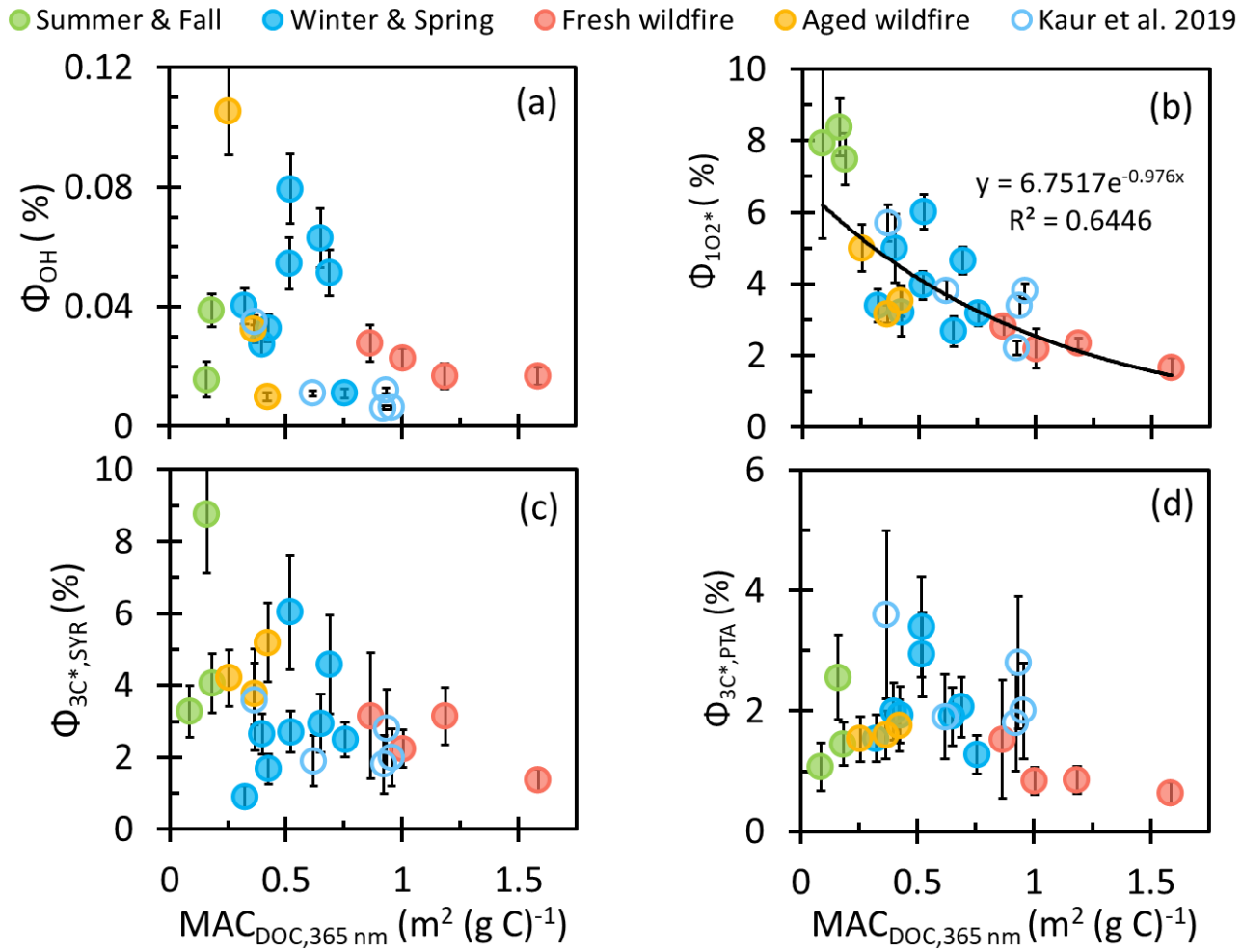

Figure S22. Apparent quantum yields of (a) hydroxyl radical, (b) singlet molecular oxygen, and oxidizing triplet excited states of organic matter determined by (c) syringol and (d) (phenylthio)acetic acid as a function of DOC-normalized mass absorption coefficient at 365 nm (solid circles). Previous measurements made in Davis winter particle extracts are shown in blue open circles (Kaur et al., 2019). The solid black line represents an exponential regression to all of the $^1O_2$* data in this work, not including data from Kaur et al. (2019).

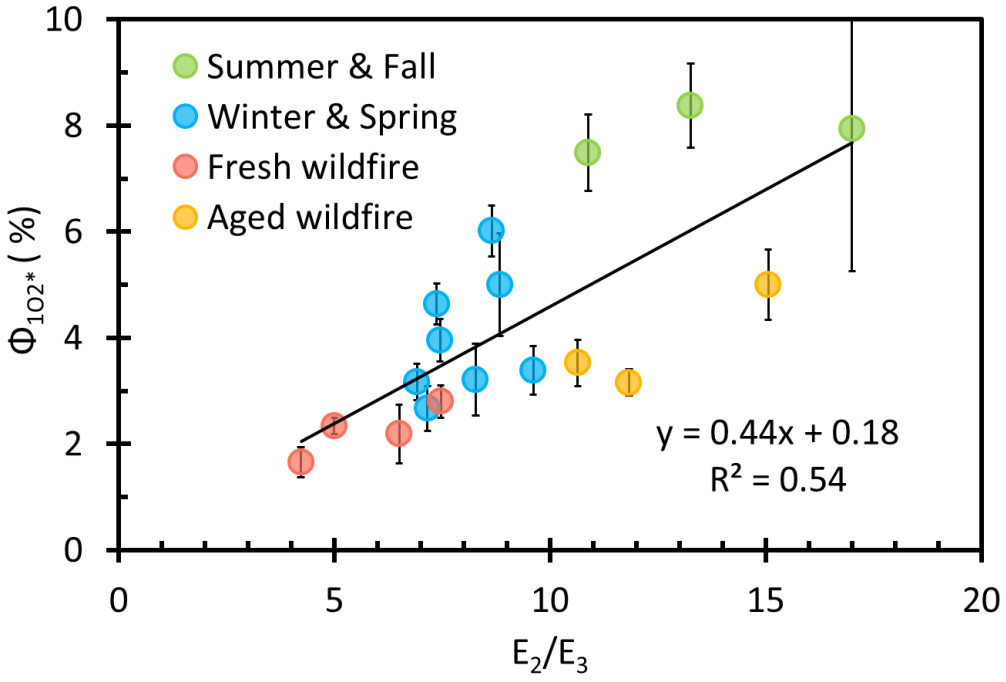

Figure S23. Apparent quantum yields of $^1O_2$* as a function of E_2/E_3.

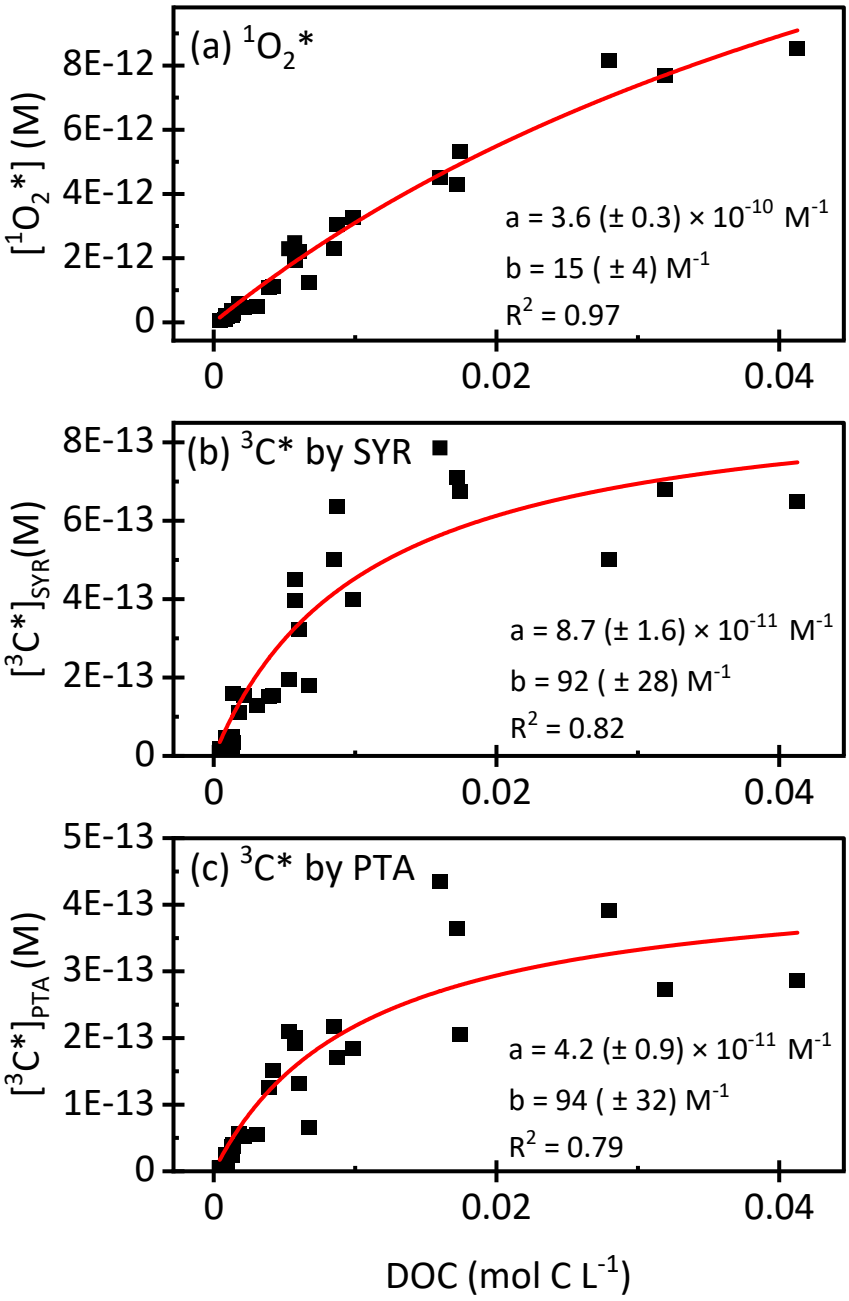

Figure S24. Dependence of (a) $^1O_2$*, (b) ^{3}C* determined by SYR, and (c) ^{3}C* determined by PTA on dissolved organic carbon. Solid lines represent hyperbolic regressions with the equation $[Ox] = \frac{a[DOC]}{1+b[DOC]}$. The equation is derived in Kaur et al. (2019); as described in this past work, we obtain the rate constant for quenching and reaction of the oxidant by DOC using the fitted value of the *b* parameter. The data points include the two previous measurements made in Davis winter particle and wildfire particle extracts from Ma et al. (2023a), but not data from Kaur et al. (2019).

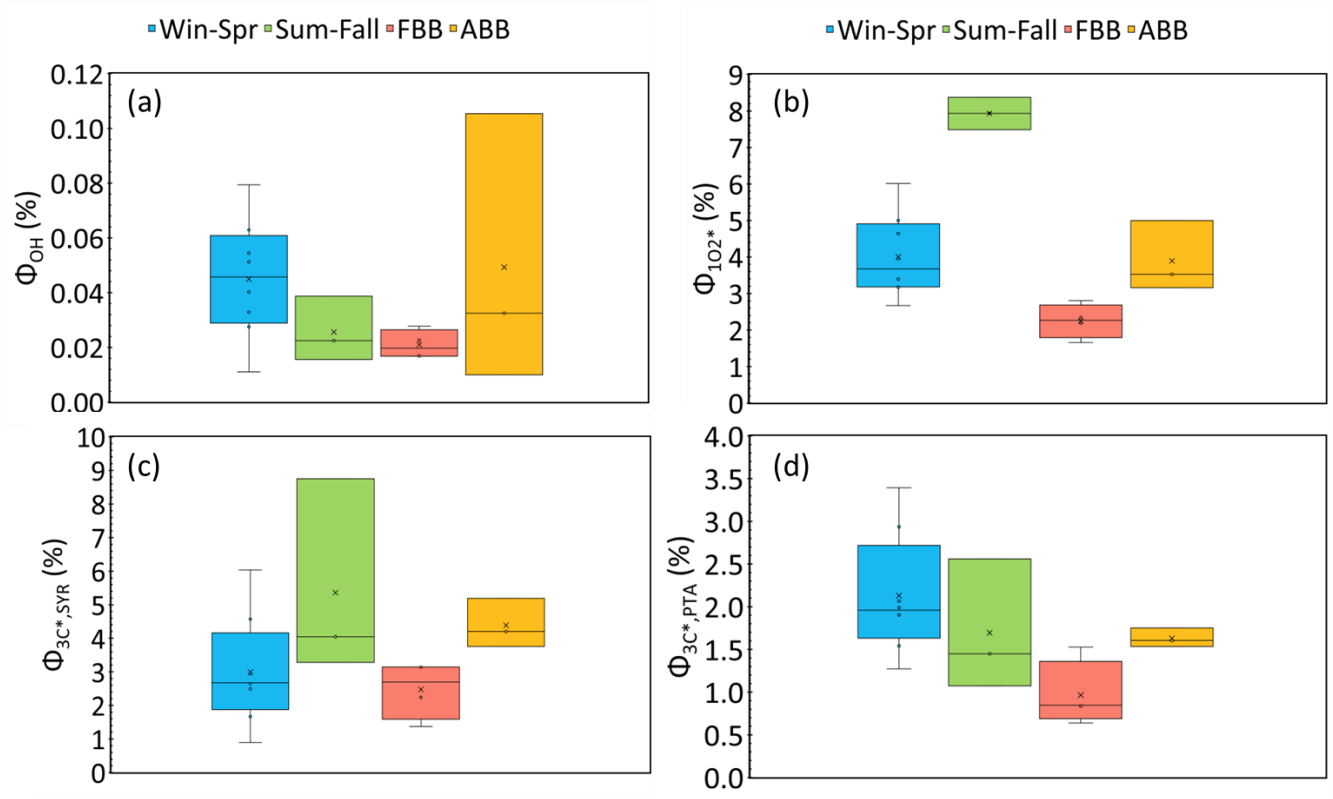

Figure S25. Box plots of apparent quantum yields of (a) $^{\bullet}$OH, (b) $^1O_2$*, (c) ^{3}C* determined by SYR, and (d) ^{3}C* determined by PTA for each sample type. For each box, the horizontal line within the box is the median value, while the top and bottom of the box represent the 75th and 25th percentiles, and the cross symbol and open circles are the mean value and data points, respectively. Whiskers represent the minimum and maximum data points.

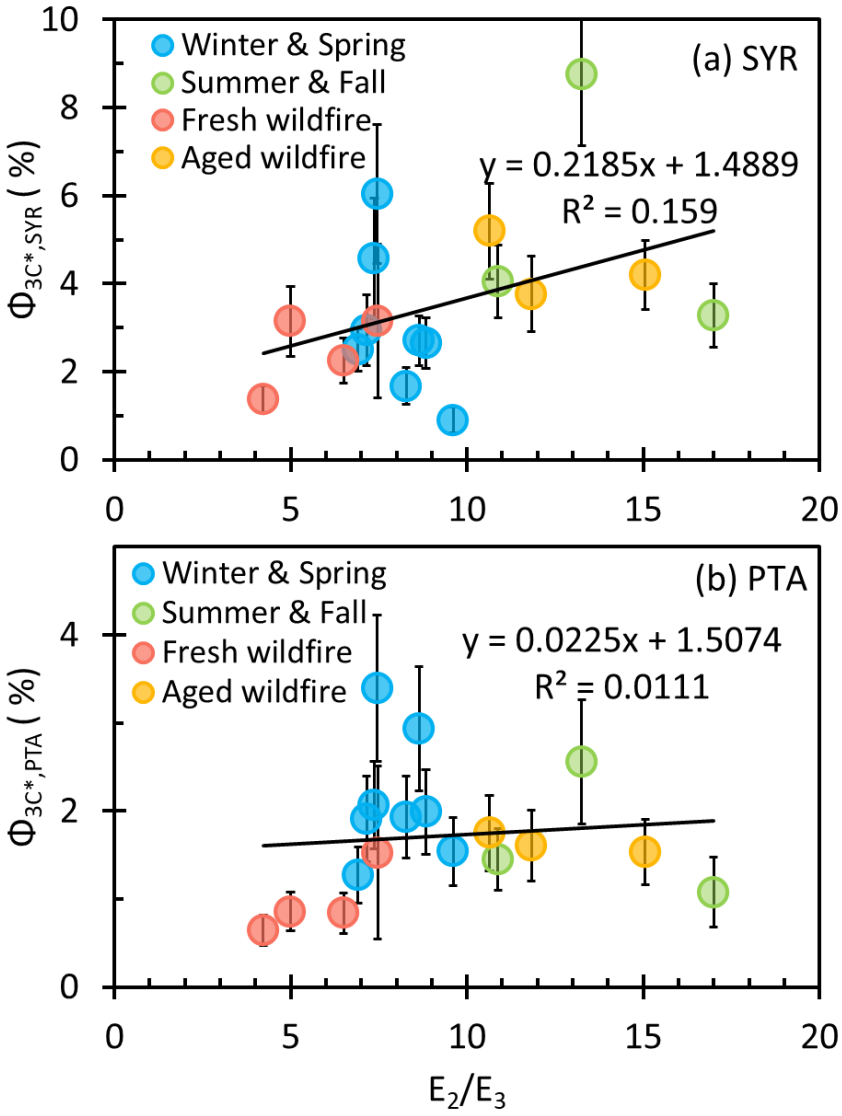

Figure S26. Apparent quantum yields of $^3C^*$ determined by (a) SYR and (b) PTA as a function of E_2/E_3.

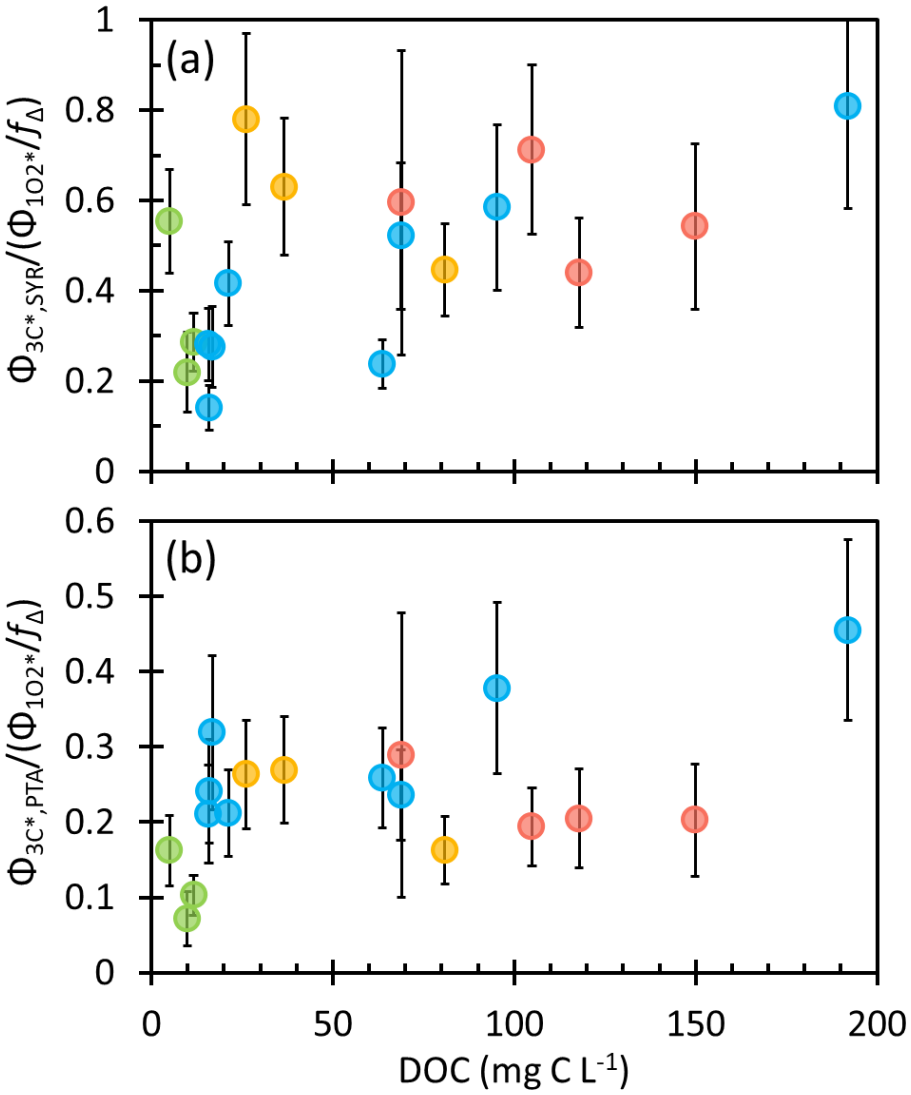

Figure S27. Approximate fraction of the total triplet pool (i.e., those that can generate singlet oxygen) that can oxidize (a) SYR and (b) PTA as a function of DOC. Based on the averages (± 1 σ) for these two plots (0.47 (± 0.20) and 0.24 (± 0.09) for (a) and (b), respectively), approximately 24 % of the total triplets are strongly oxidizing (determined as the PTA average fraction) and roughly 23 % of the total triplets are weakly oxidizing (determined as the SYR average fraction minus the PTA average).

Section S4. Extrapolating photooxidant concentrations in PME to aerosol liquid water (ALW) conditions

Photooxidant concentrations that we measured in PM extracts represent dilute conditions similar to cloud/fog waters, while our goal is to estimate photooxidant concentrations in aerosol liquid water, which is orders of magnitude more concentrated. To predict photooxidant concentrations in ALW, we quantified photooxidant kinetics (i.e., oxidant formation rates and loss rate constants) for each sample type as a function of particle mass concentration and then extrapolate to ALW conditions (Kaur et al., 2019; Ma et al., 2023a).

We start by considering hydroxyl radical. Based on results from the three samples that have been studied (Kaur et al., 2019; Ma et al., 2023a), there are at least two ways that the kinetics for $^{\bullet}$OH production vary as a function of extract concentration. In the two winter samples studied, the $^{\bullet}$OH concentration is independent of DOC concentration (a proxy for extract concentration), which we interpret to mean that both the production rate (P_{OH}) and $^{\bullet}$OH sink (k'_{OH}) linearly increase with DOC (Kaur et al., 2019; Ma et al., 2023a). However, in the third sample, which was collected in the summer and heavily influenced by relatively fresh biomass burning emissions, the $^{\bullet}$OH concentration increases with DOC, which suggests that the major $^{\bullet}$OH production pathway is a bimolecular reaction whose rate increases as the square of extract concentration (Ma et al., 2023a).

In our current work, we do not observe significant differences in the relationships of [$^{\bullet}$OH] and DOC among the four sample types (Figure 5). Therefore, to predict [$^{\bullet}$OH] in ALW for our current samples, we use the average P_{OH} values of the winter and summer samples at a given PM mass/water mass ratio in Ma et al. (2023a) and do not consider the small differences among sample types. We similarly use the average for the winter and summer k'_{OH} values at each PM mass/water mass ratio (Ma et al., 2022a). Figure S28 shows the average [$^{\bullet}$OH] calculated with $^{\bullet}$OH production only from aqueous reactions (Fig. S28a) and considering both aqueous reactions and gas-phase mass transport (Fig. S28b). Figure S28a shows that the average $^{\bullet}$OH prediction fits well with the measured [$^{\bullet}$OH] in more concentrated PME, but overestimates [$^{\bullet}$OH] in PME with low particle mass/water mass ratio, i.e., in more dilute extracts. Including gas-phase mass transport of $^{\bullet}$OH (Fig. S28b) increases the predicted [$^{\bullet}$OH], most notably at low particle mass/water ratios where $^{\bullet}$OH transport from the gas phase is the dominant source of aqueous $^{\bullet}$OH.

To extrapolate ^{3}C* concentrations determined by SYR, we first fitted measured $P_{3C^*,SYR}$ versus DOC for each sample type to obtain the slope $\Delta P_{3C^*,SYR}/\Delta DOC$ (Fig. S29b), whose values are shown in Table S10. We then use these slopes to calculate $P_{3C^*,SYR}$ in ambient PM conditions with the estimated DOC concentration in ALW, which is calculated as the product of the average ratio of DOC to PM mass/water

mass ratio for each sample type (Table S10) and the particle mass concentration. We estimate the pseudo-first order rate constant for the organic sink of ^{3}C* using the product of [DOC] and the second-order rate constant of DOC reacting with and quenching ^{3}C* determined by SYR ($k_{rxn+Q,3C*,SYR}$). For the bulk of our current samples, we use $k_{rxn+Q,3C*,SYR}$ values from our previous work (Ma et al., 2023a): for the Win-Spr samples we use the Davis winter particle extracts (WIN), while for FBB and ABB samples, we use the rate constant from the summer wildfire sample (SUM). For the Sum-Fall samples, we use a rate constant obtained from fitting all of our current samples (Fig. S23b). The rate constants used are also shown in Table S10. ^{3}C* concentrations are then calculated with:

$$[^3C^*] = \frac{P_{3C*}}{k'_{3C*}} = \frac{\Delta P_{3C*}/\Delta DOC \times [DOC]}{k_{3C*+O2}[O_2] + k_{rxn+Q,3C*}[DOC]} \quad (S5)$$

where k_{3C*+O2} is the second-order rate constant of ^{3}C* reacting with dissolved oxygen and [O_2] is the dissolved oxygen concentration. The DOC values in ambient PM condition are converted to particle mass/water mass ratios using the average ratio between DOC and PM mass to water mass ratio (DOC/(PM/H_2O)) for each sample type (Table S10). We predict [^{3}C*]$_{PTA}$ in ALW using the same method but different values for the triplet production rate ($\Delta P_{3C*,PTA}/\Delta$DOC) and triplet sink ($k_{rxn+Q,3C*}$) (Table S10). Predictions for the SYR- and PTA-determined triplet concentrations as a function of PM mass/water mass ratio are in Figure S30.

The method we use to extrapolate $^1O_2$* to ALW conditions is similar to what we do for ^{3}C*. First, we fit P_{1O2*} against DOC for each sample type to obtain the slopes ($\Delta P_{1O2*}/\Delta$DOC) (Fig. S28a and Table S10). Next, we need to consider that since ^{3}C* is the precursor of $^1O_2$*, the triplet concentration will affect production of $^1O_2$*. Therefore, in addition to acting as a source of singlet oxygen, DOC also affects $^1O_2$* in two other ways: (1) DOC is a direct sink for $^1O_2$* and (2) DOC suppresses $^1O_2$* production by quenching ^{3}C*. To quantify the first of these effects, we use an estimated average rate constant of DOC reacting with $^1O_2$* ($k_{1O2*+DOC}$) from previous work (Kaur et al., 2019; Ma et al., 2023a); the value of this second-order rate constant is 1.0×10^5 (L (mol C)$^{-1}$ s^{-1}), assuming independent of the sample type. We then take the product of this rate constant with the DOC concentration under ALW conditions to calculate the pseudo-first order rate constant $k'_{1O2*,DOC}$. For the second effect, we apply $k_{rxn+Q,3C*}$ determined from $^1O_2$* data in our previous work. Note that $k_{3C*+DOC}$ values determined from $^1O_2$* are different from $k_{3C*+DOC}$ determined by SYR or PTA. The latter represents the impact of DOC on the oxidizing triplet pool, while the former represents the total triplet pool, i.e., triplets that can react with O_2. We then calculate [$^1O_2$*] with (Ma et al., 2023a):

$$\left[{}^1O_2^*\right] = \frac{\frac{\Delta P_{1O2*}}{\Delta DOC} \times [DOC]}{1 + \frac{k_{rxn+Q,3C}[DOC]}{k_{3C*+O2}[O_2]}} / (k'_{H2O} + k_{1O2*+DOC}[DOC]) \quad (S6)$$

where k'_{H2O} is the first-order rate constant for loss of $^1O_2$* in H_2O (2.2×10^5 s^{-1}; (Bilski et al., 1997)). The concentrations of singlet oxygen as a function of DOC are then transformed to a function of PM mass/water mass ratio using the relationships between these independent variables (Table S10). Predictions for the singlet oxygen concentration as a function of PM mass/water mass ratio are shown in Figure S29.

Figure S31 shows the predicted photooxidant concentrations for each sample type under aerosol liquid water conditions at 1 μg PM/μg H_2O. These concentrations are all normalized to the same photon flux condition (i.e. j_{2NB} = 0.07 s^{-1}). To consider the effect of actinic flux, we use the average estimated j_{2NB} values for each sample type (Table S9) to correct the photooxidant concentrations. These corrected values are shown in Figure 8.

Table S10. Parameters used to extrapolate photooxidant concentrations to ALW conditions

Parameters				Win-Spr	Sum-Fall	FBB	ABB
Average DOC/(PM/H_2O) (mol C L^{-1})/(μg PM/μg H_2O)				13.6	8.9	26.1	21.3
•OH	Gas-phase mass transport[a]	Gas-phase [OH] (molecular cm^{-3})		1×10^6			
		Mass accommodation coefficient α		1.0			
	$\Delta P_{OH}/\Delta DOC$ (M s^{-1}/(mol C L^{-1})[b]		WIN	1.5×10^{-6}			
			SUM	2.0×10^{-6} for DOC > 0.045 mol C L^{-1}			
				See SI in Ma et al. (2023a) for values at lower DOC			
	$k_{rxn+Q,OH}$ (L (mol C)$^{-1}$ s^{-1})			2.7×10^{8} [c]			
$^1O_2$*	$\Delta P_{1O2*}/\Delta DOC$ (M s^{-1}/(mol C L^{-1})			6.6×10^{-5}	3.2×10^{-5}	7.1×10^{-5}	4.0×10^{-5}
	$k_{rxn+Q,3C*}$ (L (mol C)$^{-1}$ s^{-1})[d]			0.47×10^7 (WIN)[e]	1.2×10^7 (All)[f]	2.1×10^7 (SUM)[e]	
	$k_{DOC+1O2*}$ (L (mol C)$^{-1}$ s^{-1})			1.0×10^{5} [g]			
$^3C^*_{SYR}$	$\Delta P_{3C*}/\Delta DOC$ (M s^{-1}/(mol C L^{-1})			8.4×10^{-5}	1.8×10^{-5}	7.5×10^{-5}	3.8×10^{-5}
	$k_{rxn+Q,3C*}$ (L (mol C)$^{-1}$ s^{-1})[d]			7.6×10^7 (WIN)[e]	7.2×10^7 (All)[f]	12×10^7 (SUM)[e]	
$^3C^*_{PTA}$	$\Delta P_{3C*}/\Delta DOC$ (M s^{-1}/(mol C L^{-1})			4.9×10^{-5}	0.61×10^{-5}	2.8×10^{-5}	1.4×10^{-5}
	$k_{rxn+Q,3C*}$ (L (mol C)$^{-1}$ s^{-1})[d]			5.7×10^7 (WIN)[e]	7.4×10^7 (All)[f]	6.6×10^7 (SUM)[e]	

[a] To calculate the rate of gas-phase mass transport, we consider both gas-phase diffusion as well as interfacial transport. We assume the particle radius is 0.5 μm at 1 μg PM/μg H_2O and that the size quantitatively increases as the water content of the particles increases (Kaur et al., 2019).

[b] Values from our previous work (Ma et al., 2023a), using either the winter sample data (WIN) or the summer sample data (SUM). The final P_{OH} values used for extrapolation in this work is the average P_{OH} values of the WIN and SUM at a given PM mass/water mass ratio.

[c] Value is calculated as the average of slopes of k'_{DOC} with DOC in winter and summer samples from our previous work (Ma et al., 2023a).

[d] Combined rate constant for reaction and quenching of triplet states by DOC. Values of this rate constant depend on what probe was employed: (1) values listed under $^1O_2$* were determined using FFA as the probe and represent DOC reactions and quenching of the total triplet pool (as measured by the perturbation of singlet oxygen); (2) values under $^3C^*_{SYR}$ were determined using SYR as the probe and represent DOC quenching and reactions with strongly and weakly oxidizing triplets; (3) values under $^3C^*_{PTA}$ were determined using PTA as a probe and represent DOC quenching and reactions with strongly oxidizing triplets.

[e] Values from our previous work (Ma et al., 2023a), using either the winter sample data (WIN) or the summer sample data (SUM).

[f] Values are calculated from the hyperbolic regressions shown in Figure S23, which use all samples from this work as well as the WIN and SUM samples from our previous work (Ma et al., 2023a).

[g] Second-order rate constant for loss of $^1O_2$* by DOC. The value is estimated using the same approach from Kaur et al. (2019) but is lower than their value of 8.2×10^5 (L (mol C)$^{-1}$ s^{-1}.

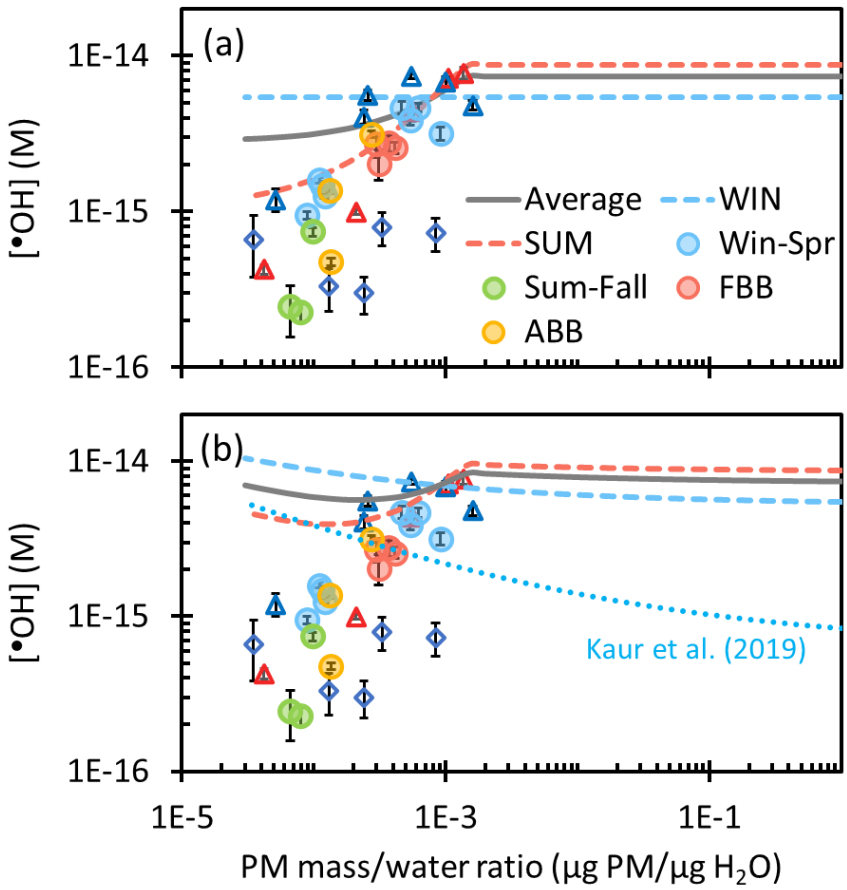

Figure S28. •OH concentration as a function of particle mass/water mass ratio calculated with (a) only aqueous •OH production and (b) •OH from both aqueous reactions and mass transport from the gas phase (Kaur et al., 2019) using a gas-phase •OH concentration of 1×10^6 mlc cm^{-3}. Circles are measured values. Previous measurements and extrapolations by Ma et al. (2023a) for Davis winter (WIN, blue) and summer wildfire (SUM, red) particle extracts are shown with triangles and dashed lines, while previous measurements and extrapolation by Kaur et al. (2019) for Davis winter particle extracts are shown with blue open diamonds and a dotted line. The grey line represents the average WIN and SUM •OH kinetics extrapolated to ALW conditions; this is our recommended prediction for all of the seasonality samples studied in the current work.

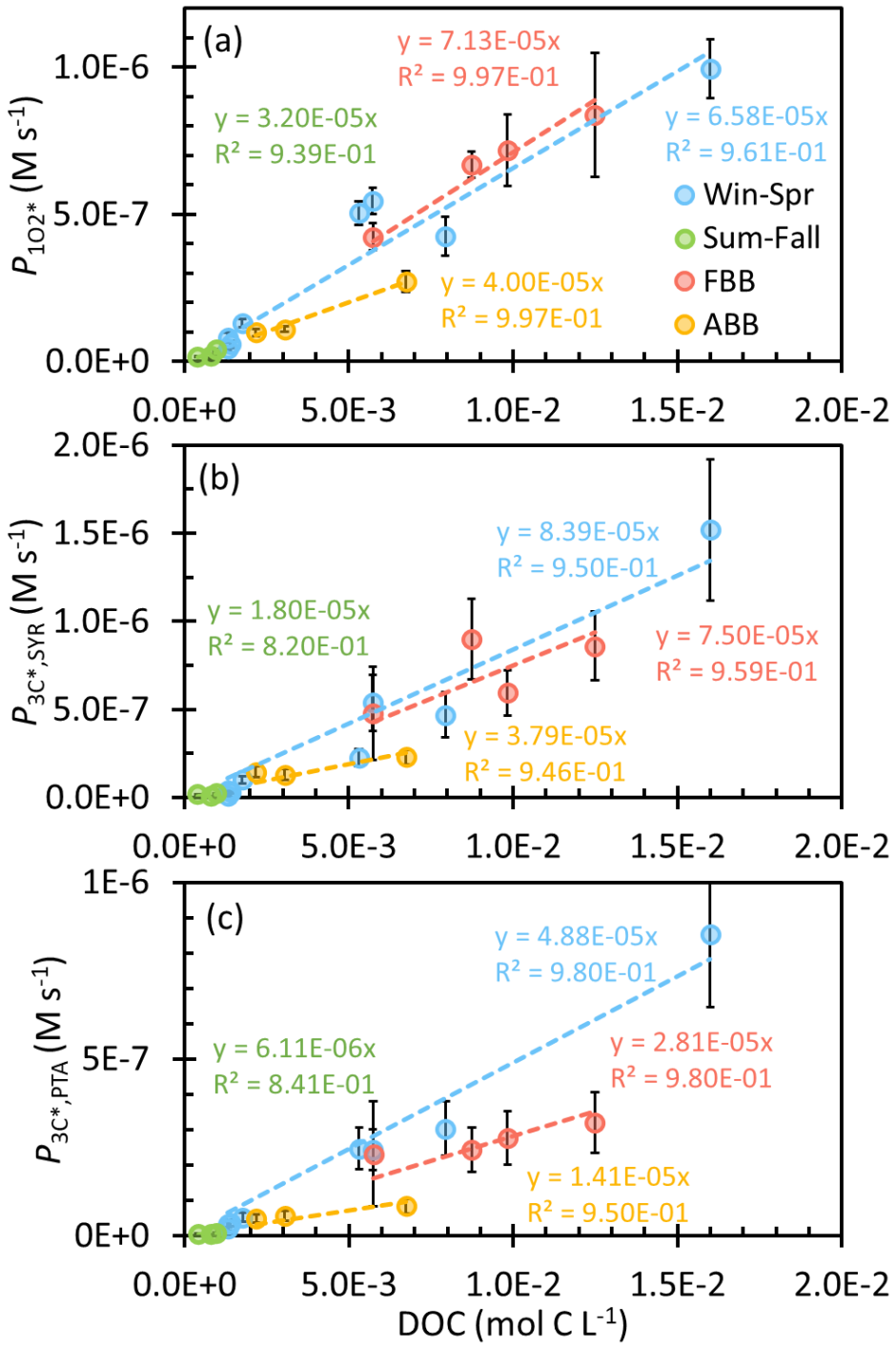

Figure S29. Production rates of (a) $^1O_2$* and ^{3}C* determined by (b) SYR or by (c) PTA as a function of DOC. Dashed lines represent linear regressions (with *y*-intercepts fixed at zero) for each sample type.

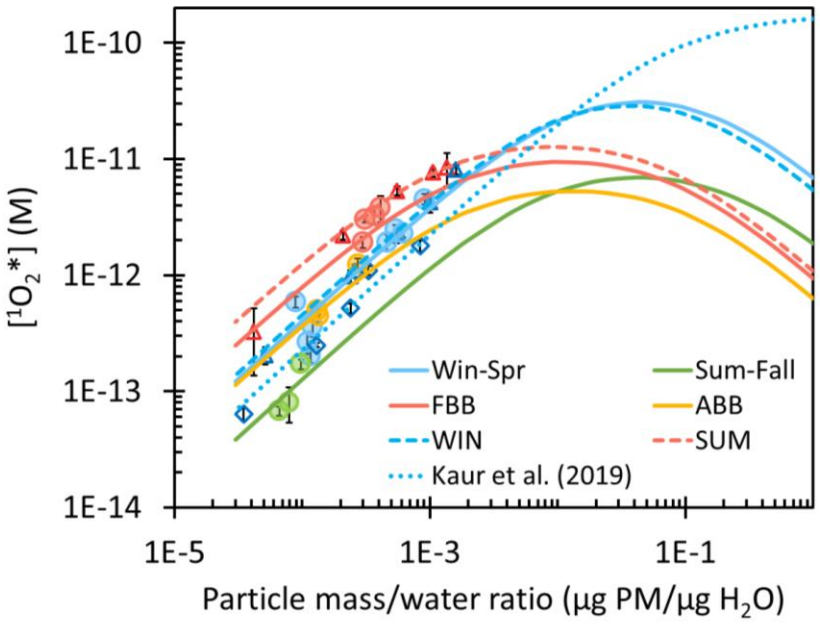

Figure S30. Dependence of $^1O_2$* concentrations for each sample type on particle mass/water mass ratio. Circles are measured values, while lines are extrapolations to ALW conditions. Previous measurements and extrapolations by Ma et al. (2023a) for Davis winter (WIN, blue) and summer wildfire (SUM, red) particle extracts are shown by triangles and dashed lines, while previous measurements and extrapolation by Kaur et al. (2019) for Davis winter particle extracts are shown with blue open diamonds and a dotted line.

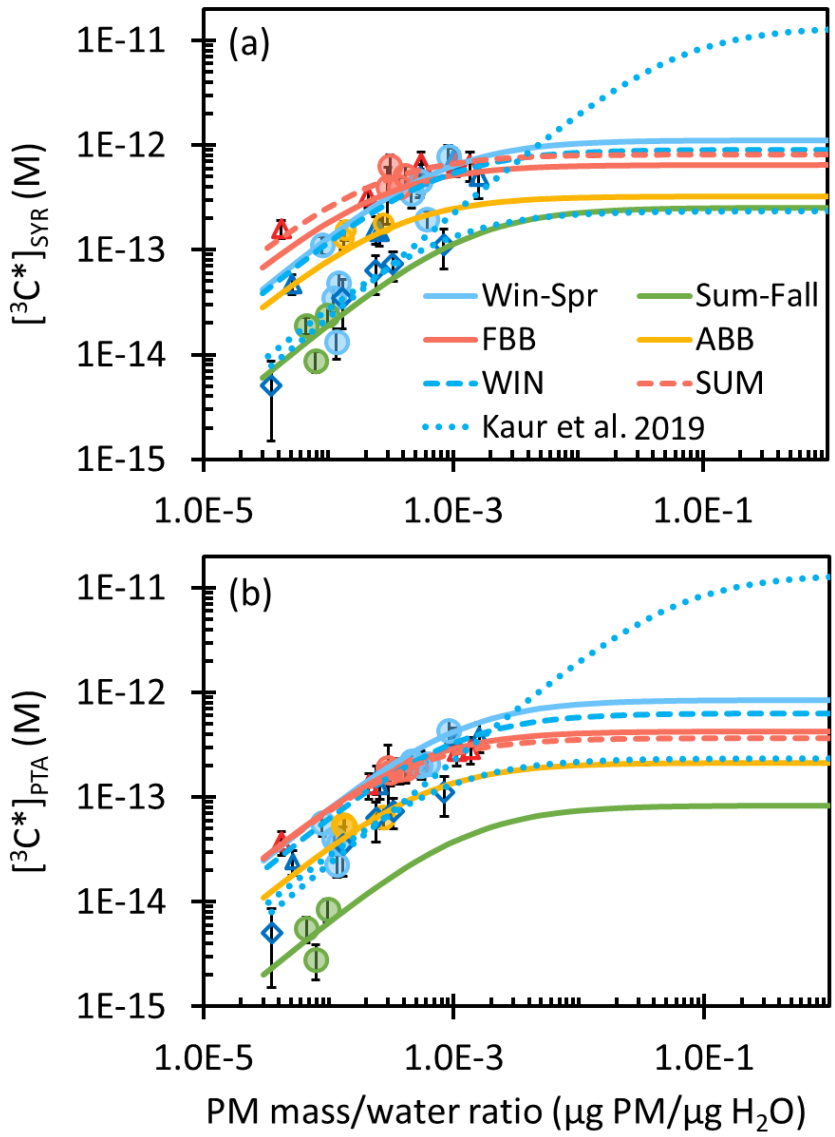

Figure S31. Dependence of $^3C^*$ concentration for each sample type determined by (a) SYR and (b) PTA on particle mass/water mass ratio. Circles are measured values, while lines are extrapolations to ALW conditions based on equation S5. Previous measurements and extrapolations by Ma et al. (2023a) for Davis winter (WIN, blue) and summer wildfire (SUM, red) particle extracts are shown by triangles and dashed lines, while previous measurements and extrapolation by Kaur et al. (2019) for Davis winter particle extracts are shown with blue open diamonds and dotted lines.

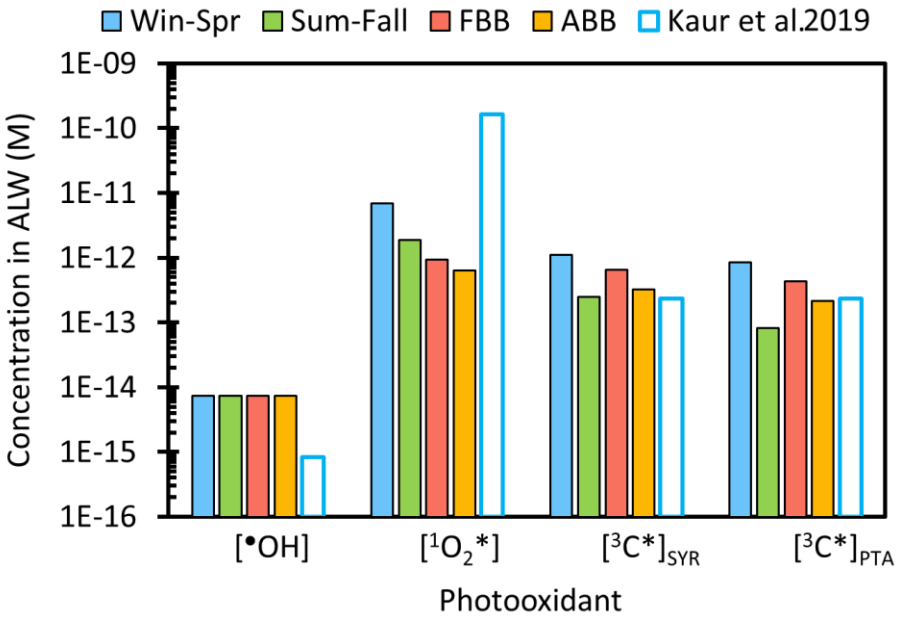

Figure S32. Predicted photooxidant concentrations for each sample type under aerosol liquid water conditions (1 µg PM/µg H_2O) normalized to the same actinic flux condition of midday on the winter solstice in Davis. Previous extrapolations made for Davis winter particle extracts are shown in open bars, where $^3C^*$ is the lower-bound estimate (Kaur et al., 2019).

References

Anastasio, C. and McGregor, K. G.: Chemistry of fog waters in California's Central Valley: 1. In situ photoformation of hydroxyl radical and singlet molecular oxygen, Atmos. Environ., 35(6), 1079–1089, doi:10.1016/S1352-2310(00)00281-8, 2001.

Bilski, P., Holt, R. N. and Chignell, C. F.: Properties of singlet molecular oxygen in binary solvent mixtures of different polarity and proticity, J. Photochem. Photobiol. A, 109(3), 243–249, doi:10.1016/S1010-6030(97)00147-0, 1997.

California Air Resources Board AQMIS Database: https://www.arb.ca.gov/aqmis2/aqmis2.php, last access: 12 July 2022.

Canonica, S. and Laubscher, H.-U.: Inhibitory effect of dissolved organic matter on triplet-induced oxidation of aquatic contaminants, Photochem. Photobiol. Sci., 7(5), 547, doi:10.1039/b719982a, 2008.

Galbavy, E. S., Ram, K. and Anastasio, C.: 2-Nitrobenzaldehyde as a chemical actinometer for solution and ice photochemistry, J. Photochem. Photobiol. A, 209(2-3), 186–192, doi:10.1016/j.jphotochem.2009.11.013, 2010.

Kaur, R. and Anastasio, C.: First measurements of organic triplet excited states in atmospheric waters., Environ. Sci. Technol., 52(9), 5218–5226, doi:10.1021/acs.est.7b06699, 2018.

Kaur, R., Labins, J. R., Helbock, S. S., Jiang, W., Bein, K. J., Zhang, Q. and Anastasio, C.: Photooxidants from brown carbon and other chromophores in illuminated particle extracts, Atmos. Chem. Phys., 19(9), 6579–6594, doi:10.5194/acp-19-6579-2019, 2019.

Ma, L., Worland, R., Jiang, W., Niedek, C., Guzman, C., Bein, K. J., Zhang, Q. and Anastasio, C.: Predicting photooxidant concentrations in aerosol liquid water based on laboratory extracts of ambient particles, 23(15), 8805–8821, doi:10.5194/acp-23-8805-2023, 2023a .

Ma, L., Worland, R., Tran, T. and Anastasio, C.: An evaluation of probes to measure oxidizing triplet excited states in aerosol liquid water, Environ. Sci. Technol., 57(15), 6052–6062, doi:10.1021/acs.est.2c09672, 2023b.

McNeill, K. and Canonica, S.: Triplet state dissolved organic matter in aquatic photochemistry: reaction mechanisms, substrate scope, and photophysical properties., Environ. Sci. Process. Impacts, 18(11), 1381–1399, doi:10.1039/c6em00408c, 2016.

Rolph, G., Stein, A. and Stunder, B.: Real-time Environmental Applications and Display sYstem: READY, Environ. Model. Softw., 95, 210–228, doi:10.1016/j.envsoft.2017.06.025, 2017.

Ross, F. and Ross, A. B.: Selected specific rates of reactions of transients from water in aqueous solution. III. Hydroxyl radical and perhydroxyl radical and their radical ions, Historical Energy Database (United States)., 1977.

Smith, J. D., Kinney, H. and Anastasio, C.: Aqueous benzene-diols react with an organic triplet excited state and hydroxyl radical to form secondary organic aerosol., Phys. Chem. Chem. Phys., 17(15), 10227–10237, doi:10.1039/c4cp06095d, 2015.

Stein, A. F., Draxler, R. R., Rolph, G. D., Stunder, B. J. B., Cohen, M. D. and Ngan, F.: Noaa's HYSPLIT atmospheric transport and dispersion modeling system, Bull. Amer. Meteor. Soc., 96(12), 2059–2077, doi:10.1175/BAMS-D-14-00110.1, 2015.

Tratnyek, P. G. and Hoigne, J.: Oxidation of substituted phenols in the environment: a QSAR analysis of rate constants for reaction with singlet oxygen, Environ. Sci. Technol., 25(9), 1596–1604, 1991.

Wenk, J., von Gunten, U. and Canonica, S.: Effect of dissolved organic matter on the transformation of contaminants induced by excited triplet states and the hydroxyl radical., Environ. Sci. Technol., 45(4), 1334–1340, doi:10.1021/es102212t, 2011.